Spectral Analysis of The Infinite Slot Leaky Wave Antenna & Leaky Wave Antenna With Multiple Slots

Dunja Lončarević

Student number: 5257999

Supervisors: prof. dr. Nuria Llombart, Sjoerd Bosma, prof. dr. Andrea Neto

Faculty of Electrical Engineering, Mathematics and Computer Science
Delft University of Technology
The Netherlands
June 30, 2022

Spectral Analysis of The Infinite Slot Leaky Wave Antenna & Leaky Wave Antenna With Multiple Slots (June 30, 2022)

Preface

Within the framework of this thesis, the analysis of the infinite slot leaky wave antenna is presented and a new geometry for the feed of a leaky lens is explored. Firstly, the analysis of the propagating leaky wave modes (TM_0 and slot modes) is done leading to the findings about the location of the slot pole w.r.t. k_0, as well as the contributions of the leaky waves and how they behave when the thickness of air-cavity and width of the slot change. Secondly, the spectral analysis of the near field is put forward with the goal of gaining deeper understanding of the leaky wave modes' behaviour and their asymmetry. Finally, a new geometry: leaky wave antenna with multiple slots is explored and its potential of lowering the levels of cross pol. is shown.

Acknowledgements

I would like to thank my supervisor, dr. Nuria Llombart, for being a true mentor to me in the previous year. Thank you for your guidance, patience and seemingly inexhaustible energy that you put into this project together with me. You really bring the *super* to the word *supervisor*.

To Sjoerd Bosma, thank you for learning together with me and always being ready to drop whatever you were working on and help me with yet another bug. Furthermore, I still have your copy of Felsen.

I also owe big thanks to dr. Andrea Neto. Thank you for spending hours with me at the beginning of my thesis helping me be less afraid of complex analysis. It worked.

And to the whole Terahertz sensing group, thank you for creating the most amazing atmosphere that makes it easy coming to the office every day. I look forward to not starting lunch until everyone is at the table for the upcoming years.

To the friends that have by now transcended into the realm of family, thank you. Your love and support, well, that alone makes life worth living. I love you.

And to my family. Волим вас. Хвала.

I never thought I'd need so many people. David Bowie

But I did. I needed all of you. Thank you.

Spectral Analysis of The Infinite Slot Leaky Wave Antenna & Leaky Wave Antenna With Multiple Slots

---

This thesis is submitted in partial fulfillment of the requirements for the degree of

MASTER OF SCIENCE

in

ELECTRICAL ENGINEERING

by

Dunja Lončarević

The work presented in this thesis was performed at:
Terahertz Sensing Group
Department of Microelectronics
Faculty of Electrical Engineering, Mathematics and Computer Science
Delft University of Technology

Delft University of Technology
Department of Electrical Engineering

The undersigned hereby certify that they have read and recommended to the Faculty of Electrical Engineering, Mathematics and Computer Science for acceptance the thesis entitled "**Spectral Analysis of The Infinite Slot Leaky Wave Antenna** & **Leaky Wave Antenna With Multiple Slots**" by **Dunja Lončarević** in partial fulfillment of the requirements for the degree of **Master of Science**.

Dated: July 6, 2022

Chairman: _____
prof. dr. Nuria Llombart

Advisor: _____
prof. dr. Andrea Neto

Committee Member: _____
dr. ir. Rob Remis

Contents

1 Introduction **1**
- 1.1 Background . . . 1
- 1.2 Contribution of the thesis . . . 2
- 1.3 Outline of the thesis . . . 2

2 Analysis of the leaky wave modes **5**
- 2.1 TM_0 mode . . . 5
- 2.2 Slot mode . . . 8
  - 2.2.1 Behaviour of the slot mode . . . 10
  - 2.2.2 Integration in the complex k_y-plane . . . 12
  - 2.2.3 Contributions to the magnetic current along the slot . . . 14
- 2.3 Approximated contributions of the leaky waves . . . 18
  - 2.3.1 Spectrum of the electric field . . . 18
  - 2.3.2 Far field . . . 19

3 Spectral analysis of the near field **23**
- 3.1 Solving the integral in α . . . 23
- 3.2 Singularities in k_ρ-plane . . . 24
- 3.3 Integration . . . 26
  - 3.3.1 E-plane . . . 27
  - 3.3.2 H-plane . . . 29
  - 3.3.3 Arbitrary plane . . . 31
- 3.4 Verification . . . 34

4 Leaky wave antenna with multiple slots **37**
- 4.1 Tapered slot . . . 37
- 4.2 Introduction of the LWA with multiple slots . . . 40
  - 4.2.1 LWA with three slots as a feed to a lens . . . 42
- 4.3 Parametric analysis of the LWA with multiple slots . . . 45
  - 4.3.1 Angle α_r . . . 45
  - 4.3.2 Number of slots . . . 47
  - 4.3.3 Air-cavity thickness . . . 49
  - 4.3.4 Slot tapering . . . 50

5 Conclusions and future work **53**
- 5.1 Summary and conclusions . . . 53
- 5.2 Future work . . . 54

Bibliography **57**

A Closing the integral in α analytically **59**

B β-plane integration and choosing the Riemann sheets **61**

C Residual contributions of the modes **63**

Chapter 1

Introduction

1.1 Background

Dielectric leaky lens antennas fed by resonant leaky wave feeds are by now a mature technology that has been demonstrated at mm and sub-mm wavelengths, achieving high aperture efficiency with $10-15\%$ operational bandwidth. However, due to the need for higher range resolution in radars and larger frequency characterization in spectrometers, the need for the antennas with wider operational bandwidth appeared. Answering these requirements, infinite slot leaky wave antenna was first introduced in [1]. As is illustrated in Figure 1.1, this antenna consists of an infinite slot etched into the ground plane that separates the lower and the upper semi-infinite mediums. Additionally, between the ground plane and the upper medium, thin layer of vacuum is placed responsible for inducing the TM_0 leaky wave mode. How this leaky wave mode propagates together with the slot mode induced by the infinite slot itself and how they contribute to the far field in H and E-planes is demonstrated in [1]. Furthermore, the ultra-wideband property of the structure is shown and the antenna is proposed as a feed to a leaky lens.

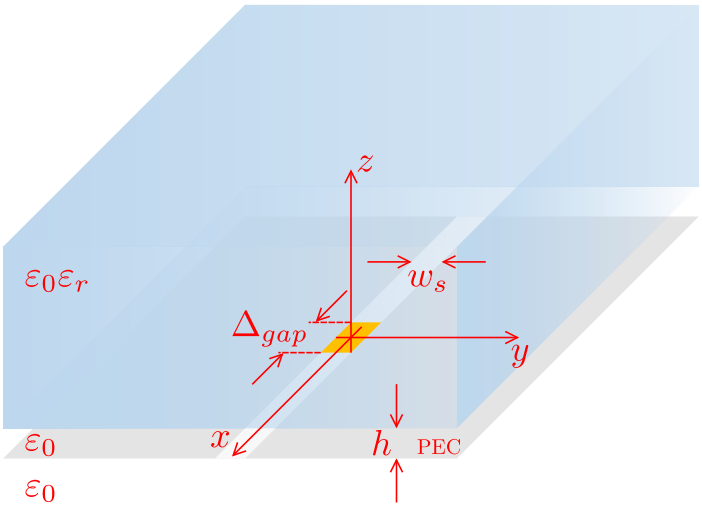

Figure 1.1: Infinite slot leaky wave antenna

However, the infinite slot leaky wave antenna suffers from high levels of cross pol. which limits the aperture efficiency of the leaky lens that uses it as the feed. In order to lower this cross pol. component, the state of the art leaky lens feeds use tapering of the infinite slot and very thin air-cavity so as to weaken the leaky waves and therefore their contribution to the cross pol. as well [2], [3]. On the other hand, this leads to the patterns of the feed that are not very

directive, requiring lenses that have large truncation angles allowing more reflection in the lens as well as increasing the complexity of manufacturing the matching layer. [4]

In order to understand the cross pol. better and the reasons for its high levels, deeper understanding of the propagating leaky wave modes is needed. For this reason, the modes and their propagation constants are analysed as was previously started in [5]. Furthermore, the spectral analysis of the near field is done with the same goal. Finally, based on the gained insights, a new geometry that decreases the cross pol. is presented and explored.

1.2 Contribution of the thesis

Within the framework of the thesis, the analysis of the infinite slot leaky wave antenna is presented and a new geometry for the feed of a leaky lens is explored.

Firstly, the analysis of the propagating leaky wave modes (TM_0 and slot modes) is presented. Since the Riemann sheet w.r.t. the lower semi-infinite medium in which the slot pole is to be found is unknown, the analysis of the magnetic current along the slot and what contributes to it is put forward. After presenting the integration path that allows the separation of different components of the current, the results are compared to the total magnetic current which is obtained by not crossing any branch-cuts in k_x-plane. From this analysis, it is concluded that the slot pole is in the top Riemann sheet w.r.t. k_0. Moreover, it is noted that the slot mode becomes less dominant as the air-cavity thickness and width of the slot become larger in terms of the wavelength.

Secondly, the spectral analysis of the near field is put forward. In order to obtain the electric field in the near field, the integral in α is solved analytically using an approximation on the magnetic current along the slot. Next, the singularities of the integrand in k_ρ are presented after which the integration paths for different planes are defined. This complex analysis together with its results provides with the deeper understanding of how the TM_0 and the slot mode behave and in what ways they are different and non-symmetrical.

Finally, a new geometry: leaky wave antenna with multiple slots is explored. After comparing it to the state of the art leaky lens feed (tapered slot) and performing the parametric analysis, it is concluded that for the same air-cavity thickness, the LWA with three slots outperforms the tapered slot in terms of cross pol. efficiency and, consequently, in aperture efficiency (when used as a feed to a leaky lens antenna). Furthermore, the lens truncation angle is decreased which can be beneficial in manufacturing of the matching layer.

1.3 Outline of the thesis

This report is divided into three central chapters. In Chapter 2, the analysis of the leaky wave modes and their propagation constants is presented. Firstly, the TM_0 mode is shown (Section 2.1) after which the slot mode is analysed (Section 2.2). In order to determine in which Riemann sheet of k_0 is the slot leaky wave pole in and consequently calculate its propagation constant, the behaviour of the pole is analysed in Subsection 2.2.1. Furthermore, comparing the total magnetic current along the slot to the current obtained by adding contributions of the leaky waves and the space wave, it is demonstrated that the leaky wave pole of the slot mode is in the top Riemann sheet of the lower semi-infinite medium (Subsection 2.2.3). Next, the approximated contributions of the leaky waves are presented in Section 2.3, where the high

levels of cross pol. component are discussed.

In Chapter 3, the spectral analysis of the near field is put forward with the goal of gaining deeper understanding of the leaky waves' behaviour. In Section 3.1, the closing of the integral in α is demonstrated together with the approximations used in order to be able to do it analytically. Next, the singularities in k_ρ are presented (Section 3.2). In Section 3.3, the integration paths for different planes are shown together with the electric fields obtained through the presented method. Finally, the verification of the results is presented in Section 3.4.

In Chapter 4, leaky wave antenna with multiple slots is explored as a design which could reduce the cross pol. Firstly, the current state of the art leaky lens feeds (tapered slots) are shown (Section 4.1). Next, the leaky wave antenna with three slots is presented as an example of the antenna with multiple slots and its performance is compared to that of a tapered slot (Section 4.2). Finally, in Section 4.3 the parametric analysis of the leaky wave antenna with multiple slots is performed where it is shown that this antenna can reduce the cross pol. and obtain similar aperture efficiency as the tapered slot antenna of the same air-cavity thickness, but for a smaller lens truncation angle.

Conclusions and future work are presented in Chapter 5.

Chapter 2

Analysis of the leaky wave modes

The analysed structure consists of the infinite slot directed along x-axis printed on an infinite ground plane that separates the lower and the upper semi-infinite mediums. Between the upper semi-infinite medium and the ground plane a thin layer of vacuum is placed, the thickness of which is h. This antenna is excited by a uniform y oriented delta-gap electric current. In Figure 1.1 the antenna is illustrated with the symbols that are be used for its parameters throughout the report.

The electric field of this antenna can be calculated as:

$$\vec{E}(\vec{r}) = \frac{1}{4\pi^2} \iint_{-\infty}^{\infty} \tilde{G}^{EM}(k_x, k_y, z, z')\vec{M}(k_x, k_y)\mathrm{e}^{-jk_x x}\mathrm{e}^{-jk_y y} dk_x dk_y, \tag{2.1}$$

where $\tilde{G}^{EM}(k_x, k_y, z, z')$ represents the spectral Green's function for the stratification of the analysed structure in the absence of the slot, while $\vec{M}(k_x, k_y)$ is the spectral domain magnetic current along the slot. Since the coordinate system is taken as such that the slot is positioned at $z' = 0$, the dependence on z' in the Green's function is omitted throughout the thesis report.

It is well known that the dominant contributions to the field of this antenna are due to the pole singularities of both the Green's function (TM_0 mode) and the magnetic current (slot mode) [1].

In Section 2.1 the formulas to calculate the propagation constant of the TM_0 mode are presented. Next, the behaviour of the slot mode pole is analysed in Section 2.2 where the integration path in k_y-plane is defined and the contributions to the magnetic current are obtained. Finally, in Section 2.3 the approximated contributions of the leaky waves are evaluated in the far field.

2.1 TM_0 mode

TM_0 mode is a consequence of the pole that appears in the spectral Green's function. In order to obtain the propagation constant of the TM_0 leaky wave, this pole needs to be located [6].

The spectral Green's function for calculating the electric field from magnetic currents is:

$$\tilde{G}^{EM} = \begin{bmatrix} \dfrac{(v_{TM} - v_{TE})k_x k_y}{k_\rho^2} & -\dfrac{v_{TE}k_y^2 + v_{TM}k_x^2}{k_\rho^2} \\ \dfrac{v_{TE}k_x^2 + v_{TM}k_y^2}{k_\rho^2} & \dfrac{(v_{TE} - v_{TM})k_x k_y}{k_\rho^2} \\ -\zeta\dfrac{k_y}{k} i_{TM} & \zeta\dfrac{k_x}{k} i_{TM} \end{bmatrix}, \tag{2.2}$$

where $k_x = k\sin\theta\cos\phi$, $k_y = k\sin\theta\sin\phi$, $k_\rho = \sqrt{k_x^2 + k_y^2}$ while ζ and k are, respectively, characteristic impedance of the medium in which the electric field is calculated and its propagation constant. Furthermore, the currents and voltages are the solutions of the transmission line representation of the analysed structure (Figure 2.1). Since TM and TE modes are decoupled, their solutions of the transmission line are obtained separately. Characteristic impedances are calculated as $Z_i^{TM} = \zeta_i \frac{k_{zi}}{k_i}$ and $Z_i^{TE} = \zeta_i \frac{k_i}{k_{zi}}$. [7] Since the leaky wave pole is known to be located in the bottom Riemann sheet with respect to the upper and in the top Riemann sheet with respect to the lower semi-infinite medium, k_{zi} are chosen as:

$$k_{z0} = -j\sqrt{-(k_0^2 - k_\rho^2)}, \tag{2.3}$$

$$k_{z2} = j\sqrt{-(k_2^2 - k_\rho^2)}. \tag{2.4}$$

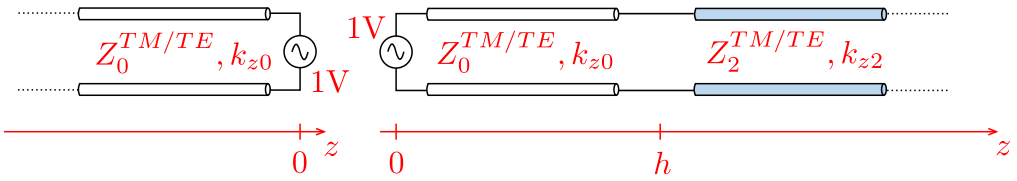

Figure 2.1: Transmission line representation of the infinite slot LWA

Solving the transmission line, it can be noted that all the currents and voltages have the same denominator:

$$D_G(k_\rho) = Z_2 + jZ_0\tan(k_{z0}h). \tag{2.5}$$

Equating the denominator to zero, and solving the equation for k_ρ, the propagation constant of the TM_0 mode is obtained. Mathematically, this equation has more than one solution. However, for the analysed antenna, only the TM_0 mode is of significance, therefore only the propagation constant for this mode is calculated.

Approximating $\tan(k_{z0}h) \approx k_{z0}h - n\pi$ and taking $n = 0$ (corresponding to TM_0 mode) and $Z_2 \approx \frac{\zeta_0}{\sqrt{\varepsilon_r}}$ (corresponding to broadside direction), propagation constant of the TM_0 mode can be approximated:

$$(k_{z0}^{g,TM_0})^2 \approx j\frac{2\pi}{\sqrt{\varepsilon_r}\lambda_0 h}, \tag{2.6}$$

$$k_\rho^{g,TM_0} = \sqrt{k_0^2 - (k_{z0}^{g,TM_0})^2}. \tag{2.7}$$

In order to converge to a more accurate solution, Newton-Raphson method is used. Firstly, the Taylor expansion around the above-mentioned approximate solution is employed:

$$D_G(k_\rho^{TM_0}) \approx D_G(k_\rho^{g,TM_0}) + D'_G(k_\rho^{g,TM_0})(k_\rho^{TM_0} - k_\rho^{g,TM_0}) = 0, \tag{2.8}$$

$$k_\rho^{TM_0} = k_\rho^{g,TM_0} - \frac{D_G(k_\rho^{g,TM_0})}{D'_G(k_\rho^{g,TM_0})}, \tag{2.9}$$

where $D'_G(k_\rho) \approx \frac{D_G(k_\rho + \frac{\Delta k}{2}) - D_G(k_\rho - \frac{\Delta k}{2})}{\Delta k}$ and $\Delta k = \frac{k_0}{500}$. These steps can be repeated for the new $k_\rho^{TM_0}$ as a guess point iteratively, keeping the track of $\left|\frac{D_G(k_\rho^{g,TM_0})}{D'_G(k_\rho^{g,TM_0})}\right|$. When

$\left|\frac{D_G(k_\rho^{g,TM_0})}{D'_G(k_\rho^{g,TM_0})}\right|$ becomes smaller than the previously agreed-upon value $e_{threshold} = 10^{-5}$, $k_\rho^{TM_0}$ is considered to be the propagation constant of the TM_0 mode. When the propagation constant is calculated over a frequency range, the propagation constant of the previous frequency point is used as the first approximated value and the input to Newton-Raphson loop for the current frequency point. [6]

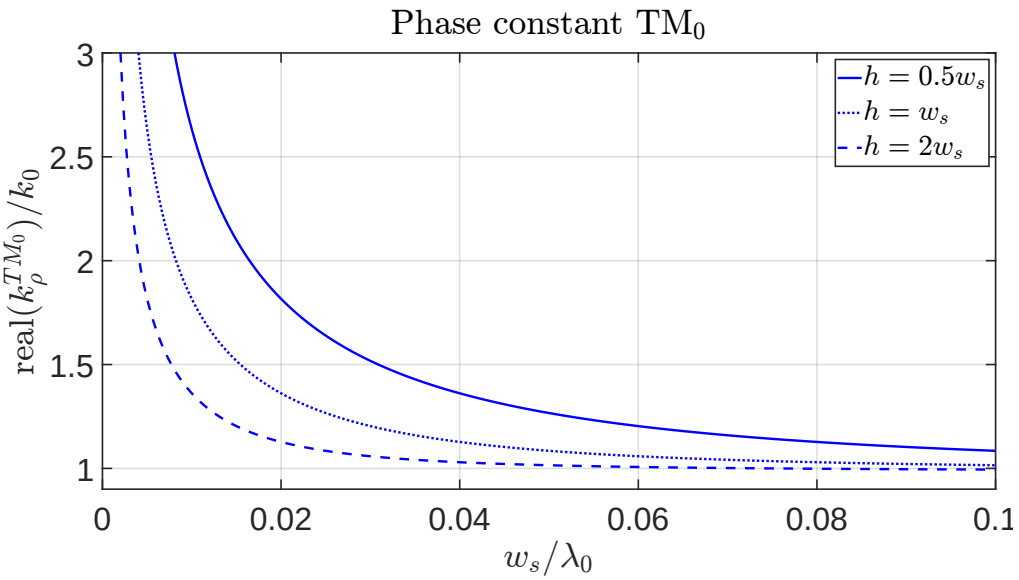

Figure 2.2: Phase constant TM_0: $\varepsilon_r = 11.9, w_s = 100\mu$m, $\Delta_{gap} = 180\mu$m

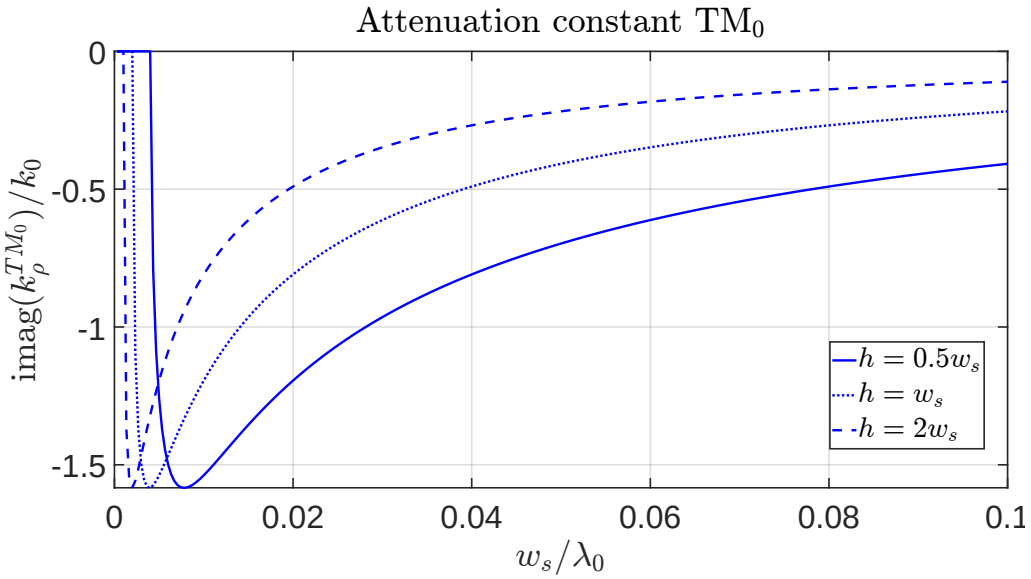

Figure 2.3: Attenuation constant TM_0: $\varepsilon_r = 11.9, w_s = 100\mu$m, $\Delta_{gap} = 180\mu$m

The propagation constant of the TM_0 mode is presented in Figures 2.2 and 2.3 where the thickness of the air-cavity is being varied. It is noted that as the thickness gets larger the pointing angle of the TM_0 mode gets smaller. Additionally, the absolute value of the attenuation constant gets smaller, leading to a more directive radiation pattern.

2.2 Slot mode

As the slot mode is not a regular leaky wave stemming from the pole of the Green's function, a more widely known structure is analysed in parallel (Figure 2.4). As can be noted, this structure does not have the air-cavity separating the silicon layer from the PEC, but is otherwise the same as the one presented in Figure 1.1. The lack of the air-cavity results in the loss of the TM_0 mode. However, the structure supports the propagation of the slot mode and is used as a reference point for the behaviour of the structure with the air-cavity. The derivation that follows is valid for both structures [8], [1].

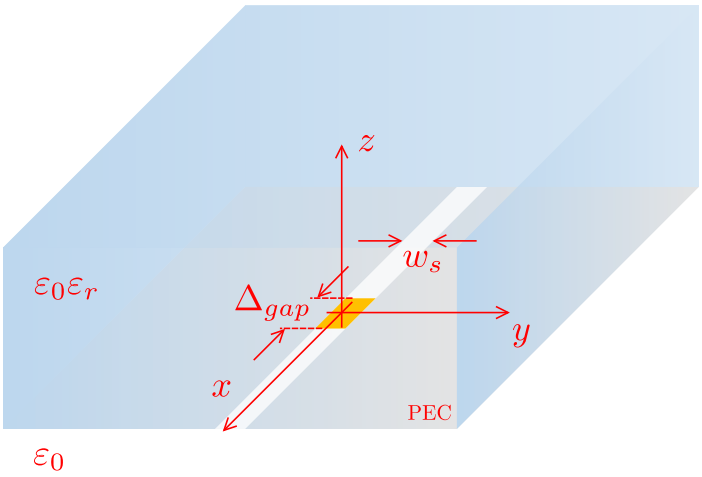

Figure 2.4: Infinite slot leaky wave antenna without the air-cavity

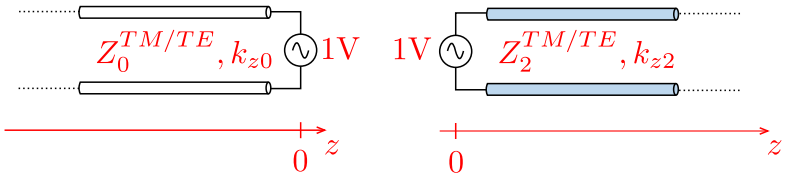

Figure 2.5: Transmission line representation of the infinite slot LWA without the air-cavity

In order to obtain the propagation constant of the slot mode, firstly the current along the slot needs to be calculated. By invoking the equivalence theorem, the slot volume is filled with the perfect electric conductor. The magnetic current on the surface above the slot is calculated as $\boldsymbol{m_s^+} = -\hat{z} \times \boldsymbol{e^+}$, and on the surface below the slot as $\boldsymbol{m_s^-} = \hat{z} \times \boldsymbol{e^-}$. Since $\boldsymbol{e^+} = \boldsymbol{e^-}$, then $\boldsymbol{m_s^-} = -\boldsymbol{m_s^+}$. Furthermore, the continuity of the magnetic field at $z = 0$ is enforced:

$$\hat{z} \times (\boldsymbol{h^+} - \boldsymbol{h^-}) = \boldsymbol{j_{inc}}, \tag{2.10}$$

$$\hat{z} \times (\boldsymbol{m_s^+} * \boldsymbol{g_2^{HM}} - \boldsymbol{m_s^-} * \boldsymbol{g_1^{HM}}) = \boldsymbol{j_{inc}}, \tag{2.11}$$

$$\hat{z} \times (\boldsymbol{m_s^+} * (\boldsymbol{g_1^{HM}} + \boldsymbol{g_2^{HM}})) = \boldsymbol{j_{inc}}, \tag{2.12}$$

$$\hat{z} \times (\boldsymbol{m_s^+} * \boldsymbol{g^{HM}}) = \boldsymbol{j_{inc}}, \tag{2.13}$$

where $\boldsymbol{j_{inc}}$ is the impressed electric current. Assuming that the slot is narrow and that the magnetic current is perfectly polarized along x:

$$m_x(x, y) * g_{xx}^{HM}(x, y) = j_{inc,y}(x, y). \tag{2.14}$$

Rewritten in integral form:[1]

$$\iint_{-\infty}^{\infty} g_{xx}^{HM}(x-x',-y')m_x(x',y')dx'dy' = \mathrm{rect}\Big(\frac{x}{\Delta_{gap}}\Big). \tag{2.15}$$

As the slot is assumed to be narrow, the magnetic current distribution has a separable space dependence on x and y. The transverse y dependence is chosen to certify the quasi-static edge singularities:

$$m_x(x,y) = v(x)m_t(y), \tag{2.16}$$

$$m_t(y) = -\frac{2}{w_s\pi}\frac{1}{\sqrt{1-\Big(\frac{2y}{w_s\pi}\Big)^2}}. \tag{2.17}$$

Continuing with the derivation:

$$\iint_{-\infty}^{\infty} g_{xx}^{HM}(x-x',-y')v(x')m_t(y')dx'dy' = \mathrm{rect}\Big(\frac{x}{\Delta_{gap}}\Big). \tag{2.18}$$

Changing the order of the integration and regrouping the variables:

$$\int_{-\infty}^{\infty} v(x')\int_{-\infty}^{\infty} g_{xx}^{HM}(x-x',-y')m_t(y')dy'dx' = \mathrm{rect}\Big(\frac{x}{\Delta_{gap}}\Big), \tag{2.19}$$

$$\int_{-\infty}^{\infty} v(x')d_M(x-x')dx' = \mathrm{rect}\Big(\frac{x}{\Delta_{gap}}\Big), \tag{2.20}$$

where $d_M(x-x') = \int_{-\infty}^{\infty} g_{xx}^{HM}(x-x',-y')m_t(y')dy'$. Rewriting $d_M(x-x')$ in the form of the anti-Fourier transformation and regrouping the variables:

$$\int_{-\infty}^{\infty} v(x')\frac{1}{2\pi}\int_{-\infty}^{\infty} D_M(k_x)\mathrm{e}^{-jk_x(x-x')}dk_xdx' = \mathrm{rect}\Big(\frac{x}{\Delta_{gap}}\Big), \tag{2.21}$$

$$\frac{1}{2\pi}\int_{-\infty}^{\infty} D_M(k_x)\mathrm{e}^{-jk_xx}\int_{-\infty}^{\infty} v(x')\mathrm{e}^{jk_xx'}dx'dk_x = \mathrm{rect}\Big(\frac{x}{\Delta_{gap}}\Big). \tag{2.22}$$

Finally, by expressing the rectangular function in the anti-Fourier form the equation becomes:

$$\frac{1}{2\pi}\int_{-\infty}^{\infty} D_M(k_x)V(k_x)\mathrm{e}^{-jk_xx}dk_x = \frac{1}{2\pi}\int_{-\infty}^{\infty} \mathrm{sinc}\Big(\frac{k_x\Delta_{gap}}{2}\Big)\mathrm{e}^{-jk_xx}dk_x, \tag{2.23}$$

from which the spectral and spatial longitudinal magnetic current is derived (since the Eq. (2.23) is valid for any k_x):

$$V(k_x) = \frac{\mathrm{sinc}\Big(\frac{k_x\Delta_{gap}}{2}\Big)}{D_M(k_x)}, \tag{2.24}$$

$$v(x) = \frac{1}{2\pi}\int_{-\infty}^{\infty} \frac{\mathrm{sinc}\Big(\frac{k_x\Delta_{gap}}{2}\Big)}{D_M(k_x)}\mathrm{e}^{-jk_xx}dk_x. \tag{2.25}$$

[1]For the case with the air-cavity, this integral is additionally averaged across the width of the slot $\frac{1}{w_s}\int_{w_s} dky$. This leads to an additional factor $\mathrm{sinc}\Big(\frac{k_yw_s}{2}\Big)$ in the final expression of the denominator as derived in Eq.(2.30) [5].

In order to determine $D_M(k_x)$, the spectral Green's function is rewritten in the form of anti-Fourier transformation in the expression for $d_M(x-x')$:

$$d_M(x-x') = \int_{-\infty}^{\infty} \left(\frac{1}{4\pi^2} \iint_{-\infty}^{\infty} G_{xx}^{HM}(k_x,k_y) \mathrm{e}^{-jk_x(x-x')} \mathrm{e}^{jk_y y'} dk_x dk_y \right) m_t(y') dy', \tag{2.26}$$

where $G_{xx}^{HM}(k_x,k_y) = G_{xx,1}^{HM} + G_{xx,2}^{HM}$, $G_{xx,i}^{HM} = -\dfrac{i_{TE,i}k_x^2 + i_{TM,i}k_y^2}{k_\rho^2}$. The currents in $G_{xx,1}^{HM}$ and $G_{xx,2}^{HM}$ are obtained by solving the transmission line representations of the structure for $z = 0^-$ and $z = 0^+$, respectively (Figure 2.1 for the case with the air-cavity and Figure 2.5 for the one without the air-cavity). After regrouping the terms in y' and reversing the order of integration:

$$d_M(x-x') = \frac{1}{4\pi^2} \iint_{-\infty}^{\infty} G_{xx}^{HM}(k_x,k_y) \mathrm{e}^{-jk_x(x-x')} \left(\int_{-\infty}^{\infty} m_t(y') \mathrm{e}^{jk_y y'} dy' \right) dk_x dk_y. \tag{2.27}$$

Closing the integral in brackets analytically, the final expression is:

$$d_M(x-x') = -\frac{1}{4\pi^2} \iint_{-\infty}^{\infty} G_{xx}^{HM}(k_x,k_y) \mathrm{e}^{-jk_x(x-x')} J_0\Big(\frac{k_y w_s}{w}\Big) dk_x dk_y, \tag{2.28}$$

$$d_M(x-x') = \frac{1}{2\pi} \int_{-\infty}^{\infty} D_M(k_x) \mathrm{e}^{-jk_x(x-x')} dk_x, \tag{2.29}$$

where

$$D_M(k_x) = -\frac{1}{2\pi} \int_{-\infty}^{\infty} G_{xx}^{HM}(k_x,k_y) J_0\Big(\frac{k_y w_s}{2}\Big) dk_y. \tag{2.30}$$

Furthermore, since $m_t(y)$ has a closed-form Fourier transform $FT(m_t(y)) = -J_0\Big(\dfrac{k_y w_s}{2}\Big)$, the spectrum of the magnetic current along the slot can be expressed as:

$$M_x(k_x,k_y) = -\frac{\mathrm{sinc}\Big(\dfrac{k_x \Delta_{gap}}{2}\Big)}{D_M(k_x)} J_0\Big(\frac{k_y w_s}{2}\Big). \tag{2.31}$$

From the Eq.(2.31) it is evident that $D_M(k_x)$ is the denominator of the magnetic current spectrum. In order to obtain the propagation constant of the slot mode, the integral in Eq.(2.30) needs to be solved and equated to zero. For the structure without the air-cavity, the integral can be solved analytically. However, for the case with the air-cavity, analytical solution does not exist and the integral needs to be solved numerically.

In Subsection 2.2.1 behaviour of the pole for the structures with and without the air-cavity is analysed. Next, in Subsection 2.2.2. integration in the complex k_y-plane is presented in order to solve the integral from Eq.(2.30) and obtain the pole of $D_M(k_x)$ for the antenna with the air-cavity. Two possible pole solutions are put forward. In Subsection 2.2.3 the significant pole is identified by reconstructing the total magnetic current. The reconstruction is obtained by summing the branch-cut and the pole contributions.

2.2.1 Behaviour of the slot mode

The integral in Eq.(2.30) can be analytically solved for the structure without the air-cavity and is given by the following expression:

$$D_M(k_x) = \frac{1}{2k_0\zeta_0} \sum_{i=0}^{2} (k_i^2 - k_x^2) J_0\left(\frac{w_s}{4} \sqrt{k_i^2 - k_x^2} \right) H_0^{(2)}\left(\frac{w_s}{4} \sqrt{k_i^2 - k_x^2} \right). \tag{2.32}$$

The slot mode pole is located in the bottom Riemann sheet for k_2 and top Riemann sheet w.r.t. k_0. The real part of the propagation constant is presented in Figure 2.6 where it can be noted that real$(k_x^{slot}) \approx \sqrt{\frac{k_0^2+k_2^2}{2}}$ [8].

However, since Eq.(2.30) cannot be solved analytically for the structure with the air-cavity, the integral needs to be evaluated numerically. For this calculation, one needs to be very careful how the branches of the semi-infinite media are crossed. In order to avoid this complication at this stage but still gain some insight into the general behaviour of the mode, firstly an approximate propagation constant of the slot mode is obtained.

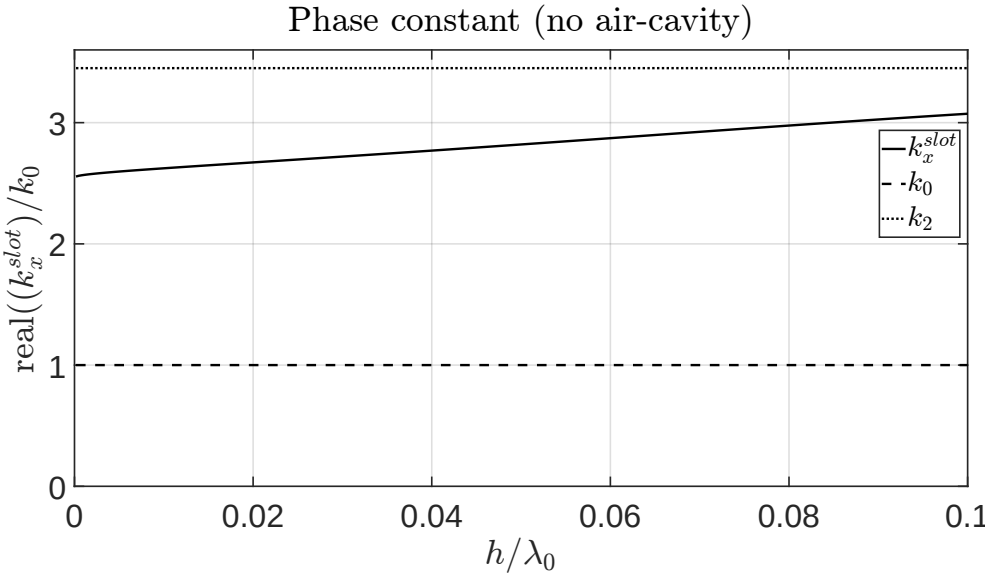

Figure 2.6: Phase constant (no air-cavity): $\varepsilon_r = 11.9, w_s = 100\mu\text{m}$, $\Delta_{gap} = 180\mu\text{m}$

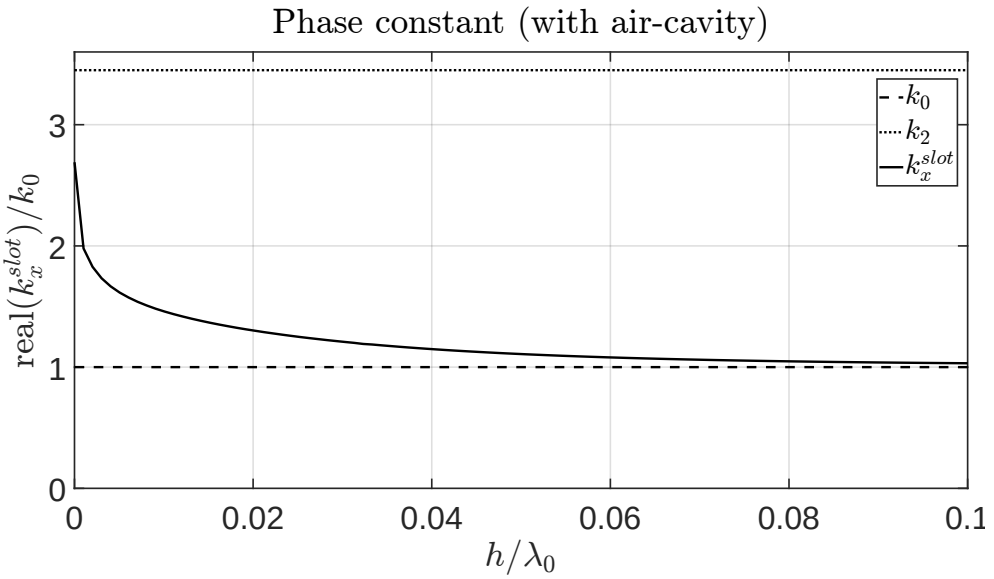

Figure 2.7: Phase constant (with air-cavity): $\varepsilon_r = 11.9, h = w_s = 100\mu\text{m}$, $\Delta_{gap} = 180\mu\text{m}$

In order to arrive at the approximate propagation constant of the slot mode for this case, the integration is performed over the real axis and only one iteration of the Newton-Raphson method is executed. More precisely, the first guess (as defined in Eq.(2.8)) is taken to be $k_x^{g,slot} = 0.9k_0$.

Since the guessed value of the slot propagation constant is real, the denominator $D_M(k_x)$ and its first derivative $D_M(k_x)'$ are calculated without having to cross any branches. Therefore, we are in the top Riemann sheets of both semi-infinite media.

The approximated value for the phase constant is presented in Figure 2.7. It can be noted that only for the very small values of h does the phase constant follow the behaviour as in the case without the air-cavity. However, as the thickness of the air-cavity gets larger, the real part of the propagation constant tends to k_0. For this reason, it becomes unclear whether the pole is located in the top Riemann sheet w.r.t. k_0, or is it necessary to cross that branch-cut and to look for the pole in the bottom Riemann sheet for k_0. This problem is discussed next.

2.2.2 Integration in the complex k_y-plane

To obtain the propagation constant of the slot mode accurately, multiple iterations of Newton-Raphson method need to be performed. This means that the integration path in k_y-plane is no longer only along the real axis and it needs to be defined.

Considering that the integration in k_y-plane depends on the Riemann sheets in which the pole is searched for in k_x-plane, the longitudinal spectral plane is illustrated in Figure 2.8a. Apart from the pole associated to the slot mode, k_x-plane also contains branch-points and their branch-cuts as a consequence of the semi-infinite mediums. On the other hand, Figure 2.8b illustrates the transverse spectral plane k_y with its branch-point and branch-cuts. Branch-points of the semi-infinite mediums are noted as k_{y0}, k_{y2} and are calculated as $k_{yi} = \sqrt{k_i^2 - k_x^2}$ [9].

It is *a priori* known that the slot mode leaks into the upper semi-infinite medium, and that its pole then must be in the bottom Riemann sheet with respect to k_2. However, the Riemann sheet in reference to k_0 is not evident (as was discussed previously). For that reason, two possible locations of the pole are analysed:

1. top Riemann sheet w.r.t. k_0, bottom Riemann sheet w.r.t. k_2,
2. bottom Riemann sheet w.r.t. k_0, bottom Riemann sheet w.r.t. k_2.

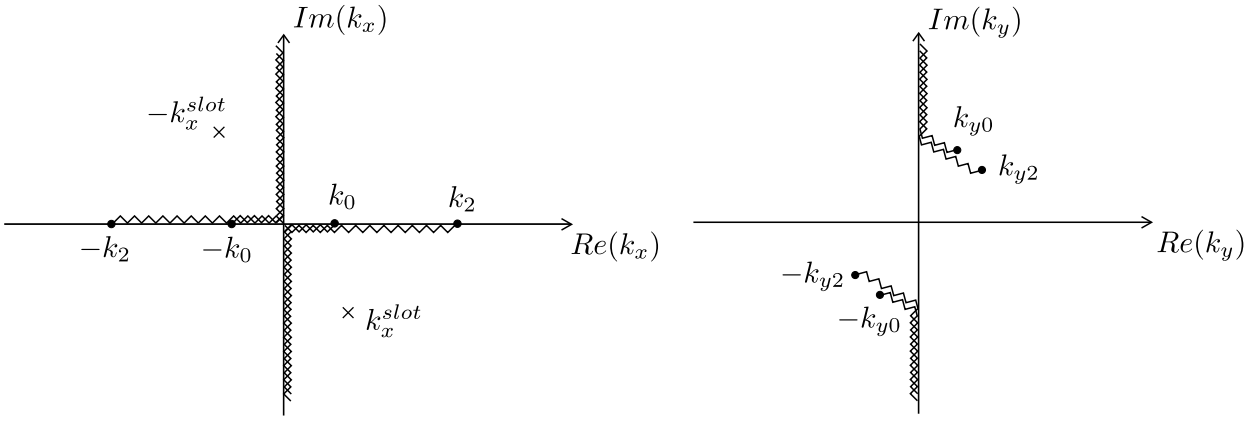

(a) Longitudinal spectral plane k_x (b) Transverse spectral plane k_y

Figure 2.8: Longitudinal and transverse spectral planes

Depending on the Riemann sheets in which the integral Eq.(2.30) is being calculated, the integration paths in k_y plane are illustrated in Figure 2.9. When $D_M(k_x)$ is obtained in the top

Riemann sheet w.r.t. k_0 and bottom Riemann sheet w.r.t. k_2, only the branch-cut associated to k_2 is crossed and the integration path in k_y-plane for this case is presented in Figure 2.9a. Furthermore, if $D_M(k_x)$ is obtained in the bottom Riemann sheet for k_0 as well as k_2, both branch-cuts are crossed (Figure 2.9b) [9]. The color of the integration path indicates how k_{zi} is calculated for $G_{xx}^{HM}(k_x, k_y)$. For the top Riemann sheet $k_{zi} = -j\sqrt{-(k_i^2 - k_\rho^2)}$, while for the bottom Riemann sheet $k_{zi} = j\sqrt{-(k_i^2 - k_\rho^2)}$ (Figure 2.9c).

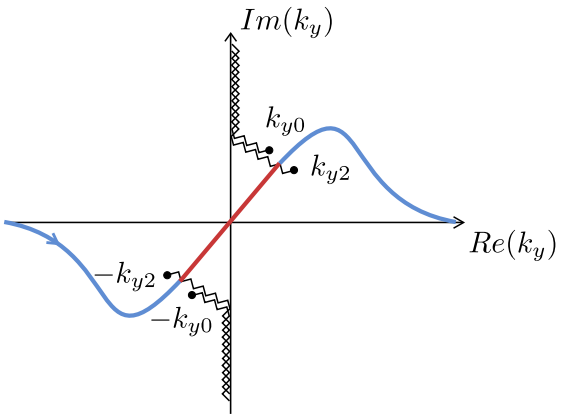

(a) Top RS w.r.t. k_0 and bottom RS w.r.t. k_2

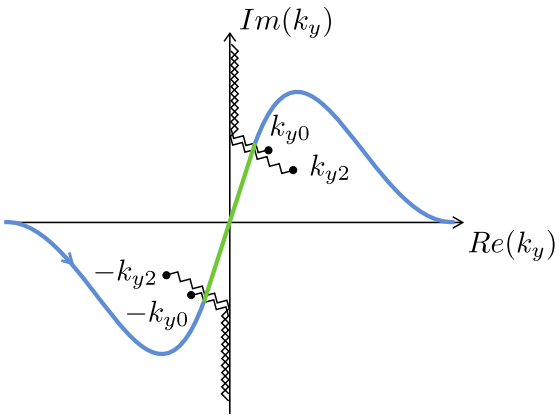

(b) Bottom RS w.r.t. k_0 and k_2

	k_0	k_2
	TOP	TOP
	BOTTOM	BOTTOM
	TOP	BOTTOM
	BOTTOM	TOP

(c) Riemann sheet legend

Figure 2.9: Integration paths in the transverse spectral plane

It is possible to determine the integration paths that are equivalent to the ones presented in Figure 2.9, but easier to implement. Invoking the Cauchy's integral theorem: $C_1 + C_2 + C_3 = 0$ (Figure 3.3b). Therefore, $C_1 = -C_2 - C_3$, and the equivalent integration path from Figure 2.9a is presented in Figure 2.11a. Similarly, crossing the branches of both media is equivalent to the integration path in Figure 2.11b [5].

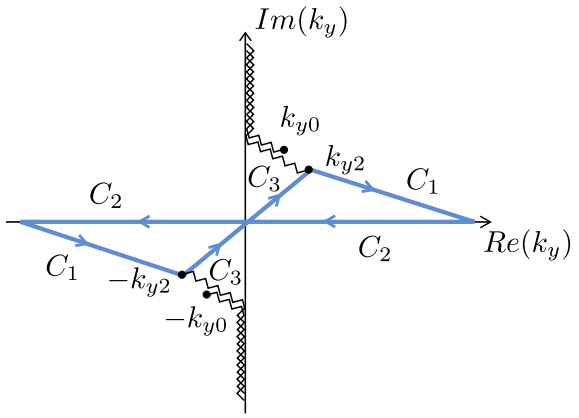

Figure 2.10: Cauchy's integral theorem in the transverse spectral plane

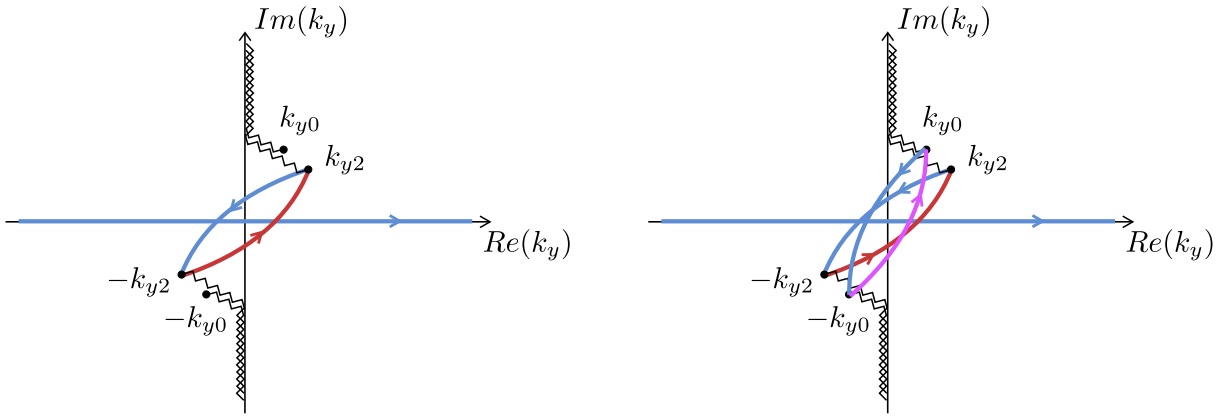

(a) Top RS w.r.t. k_0 and bottom RS w.r.t. k_2 (b) Bottom RS w.r.t. k_0 and k_2

Figure 2.11: Equivalent integration paths in k_y-plane

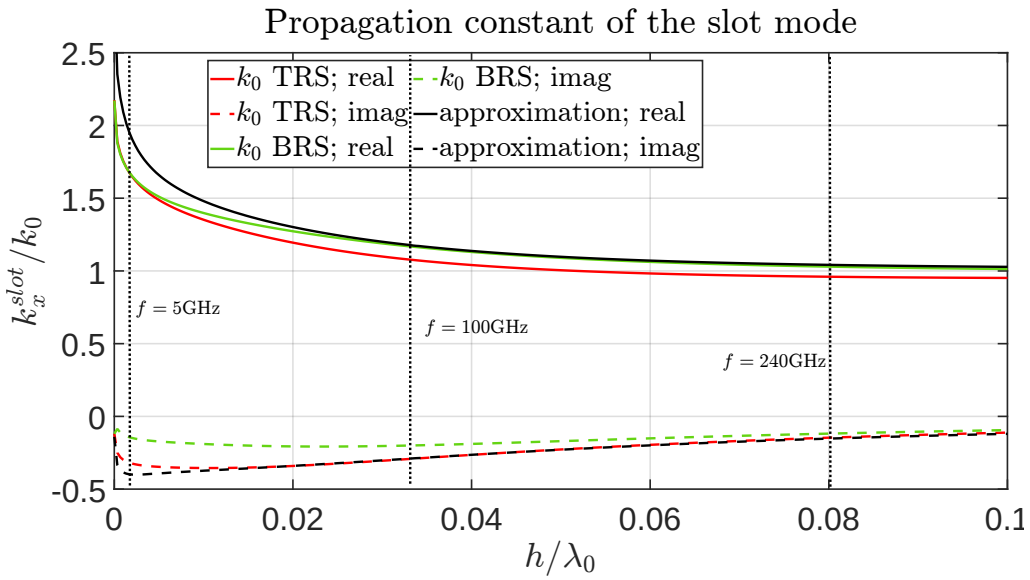

Figure 2.12: Propagation constant of the slot mode: $\varepsilon_r = 11.9, h = w_s = 100\mu$m, $\Delta_{gap} = 180\mu$m

Having defined the integration paths in the transverse spectral plane, the denominator of the magnetic current along the slot is calculated as defined in Eq.(2.30). Furthermore, using the Newton-Raphson method to converge to the accurate solution across a frequency range, the poles in different Riemann sheets with respect to k_0 are obtained and presented in Figure 2.12. As can be noted, there are two poles: one in the top and one in the bottom Riemann sheet w.r.t. the lower medium. Furthermore, the approximated propagation constant (as defined in Subsection 2.2.1) is plotted. Evidently, the approximation does not give the same results as any of the two propagation constants presented. Therefore, multiple loops of the Newton-Raphson method are needed. In the next subsection, magnetic current along the slot is reconstructed so as to determine which pole is significant for the analysed structure.

2.2.3 Contributions to the magnetic current along the slot

Longitudinal term of the magnetic current is obtained by Eq.(2.25). However, the integration path in k_x-plane that leads to the solution is not uniquely defined.

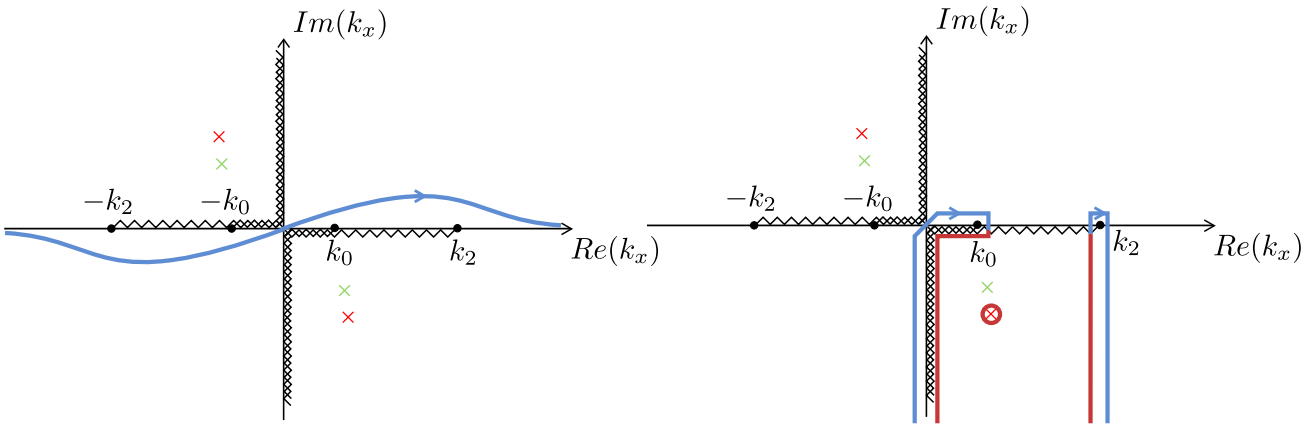

(a) Total magnetic current (b) Contributions of the branches and the pole

Figure 2.13: Integration path in k_x-plane

In Figure 2.13a, the integration path that gives the total longitudinal term of the magnetic current is illustrated. It is referred to as *total* because it does not distinguish between the contributions of the branch-cuts and the poles. The equation for this integration path is given as: $k_x^{path} = k_x + 0.01je^{-\frac{1}{2}(\frac{k_x}{k_2})^2}$. On the other hand, the path can also be chosen as the one in Figure 2.13b. As a consequence of the deformation of the original path presented in Figure 2.13a and Cauchy's theorem, the contribution of the pole in the top Riemann sheet for k_0 is added as a residue:

$$v(x) = v_1(x) + v_2(x) + v_{slot}(x), \tag{2.33}$$

$$v_{slot}(x) = -2\pi j \text{Res}\left(\frac{\text{sinc}\left(\frac{k_x \Delta_{gap}}{2}\right)}{2\pi D_M(k_x)} e^{-jk_x x} \right)\Bigg|_{k_x = k_x^{slot}}, \tag{2.34}$$

$$v_{slot}(x) = -j \frac{\text{sinc}\left(\frac{k_x^{slot} \Delta_{gap}}{2}\right)}{D'_M(k_x^{slot})} e^{-jk_x^{slot}|x|}, \tag{2.35}$$

where $v_1(x)$ and $v_2(x)$ are the contributions of the integration paths encircling branch-point k_0 and k_2, respectively, as is presented in Figure 2.13b. It is evident that the pole in the bottom Riemann sheet w.r.t. k_0 is not crossed, therefore its contribution is not added to the magnetic current.

To evaluate the significance of the pole in the top Riemann sheet for k_0, $v(x)$ obtained with the deformed path that enables the separation of the contributions is compared to $v_{total}(x)$ calculated using the integration path from Figure 2.13b. This is done for the frequency points as indicated in Figure 2.12 and the results are presented in Figure 2.14. It can be noted that for the lowest frequency point, the two evaluated currents are practically equal. As the frequency becomes higher, the difference between $v(x)$ and $v_{total}(x)$ becomes larger for the points close to the source, but is still quite negligible. Furthermore, for the case $f = 5$ GHz results of a full wave CST simulation are also plotted confirming the results obtained using the above-mentioned procedure. Similar analysis was performed for different dimensions of the infinite slot leaky wave antenna with the same qualitative results that are not included in the thesis report for conciseness.

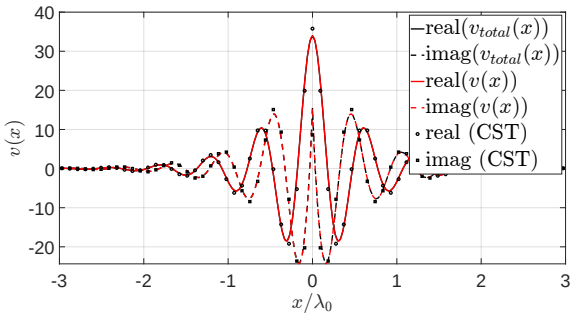

(a) $f = 5$GHz

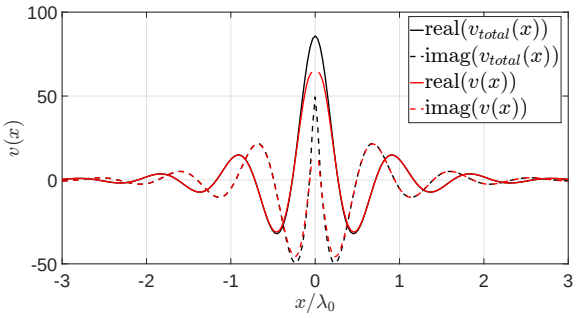

(b) $f = 100$GHz

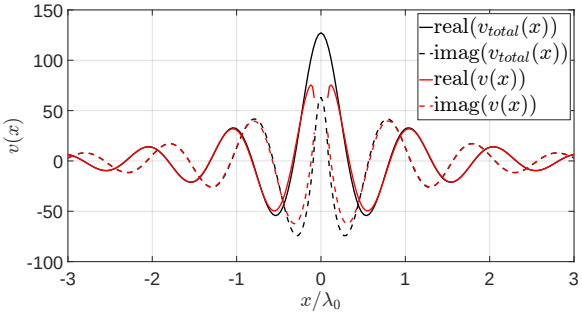

(c) $f = 240$GHz

Figure 2.14: Comparison of $v(x)$ and $v_{total}(x)$ for $f = [5, 100, 240]$ GHz: $\varepsilon_r = 11.9, h = w_s = 100\mu$m, $\Delta_{gap} = 180\mu$m

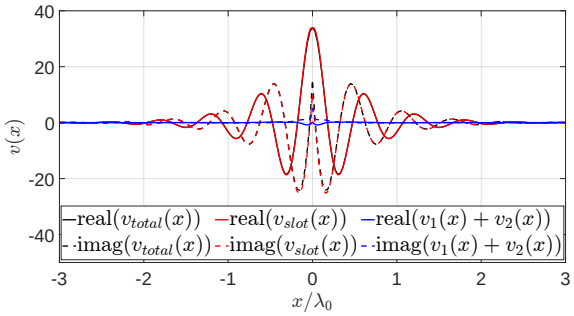

(a) $f = 5$GHz

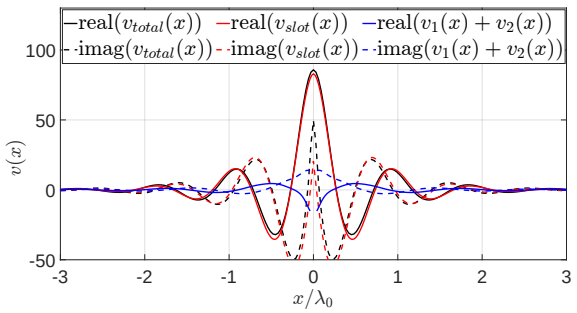

(b) $f = 100$GHz

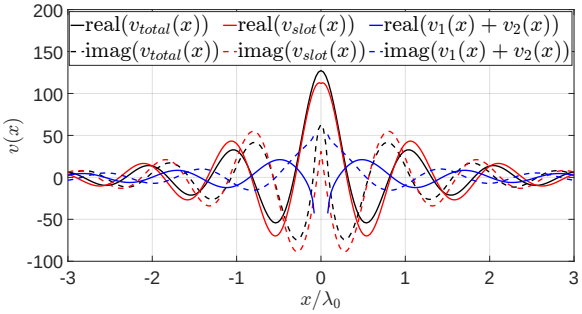

(c) $f = 240$GHz

Figure 2.15: Contributions to the magnetic current along the slot for $f = [5, 100, 240]$ GHz: $\varepsilon_r = 11.9, h = w_s = 100\mu$m, $\Delta_{gap} = 180\mu$m

Based on the presented study, it is concluded that the pole in the top Riemann sheet w.r.t. k_0 and bottom Riemann sheet w.r.t. k_2 is the significant pole for the analysed structure and is taken as the slot mode for the rest of the thesis report. On the other hand, the pole in the bottom Riemann sheet w.r.t. both media is mathematically valid, but it does not contribute

to the radiation of the antenna.

Additionally, the contributions of the leaky wave and the branch-cuts are presented in Figure 2.15. As can be seen, the leaky wave is dominant for the lower frequencies, but as the frequency gets higher (or as the thickness of the air-cavity and width of the slot become larger), the contribution of the branch-cuts increases. At $f = 240$GHz, the two contributions are of comparable scale. This is important to note because it reveals when the assumption that the leaky wave is dominant can be made and, consequently, in what frequency range should the antenna be designed.

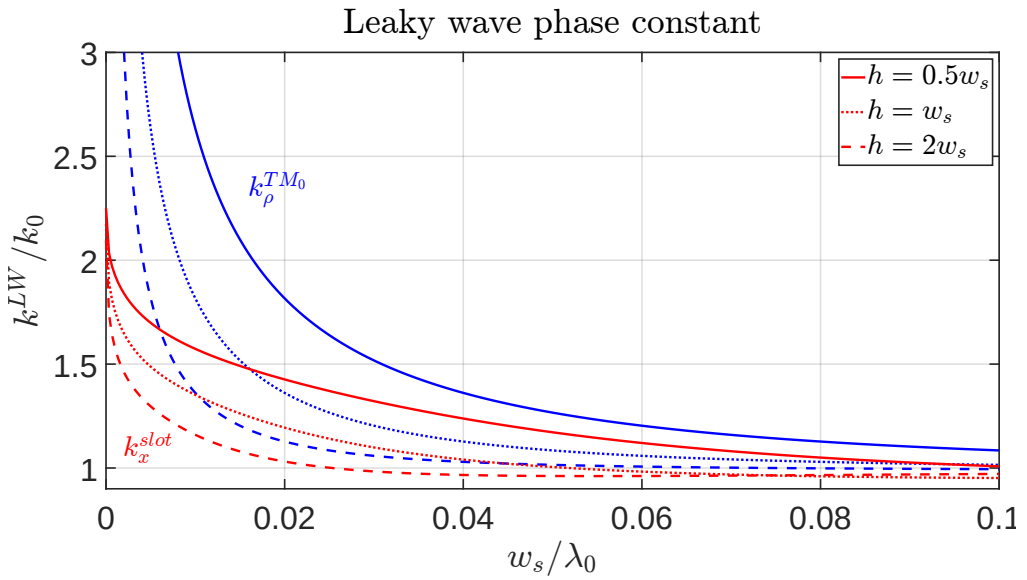

Figure 2.16: Phase constant of the leaky waves: $\varepsilon_r = 11.9, w_s = 100\mu$m, $\Delta_{gap} = 180\mu$m

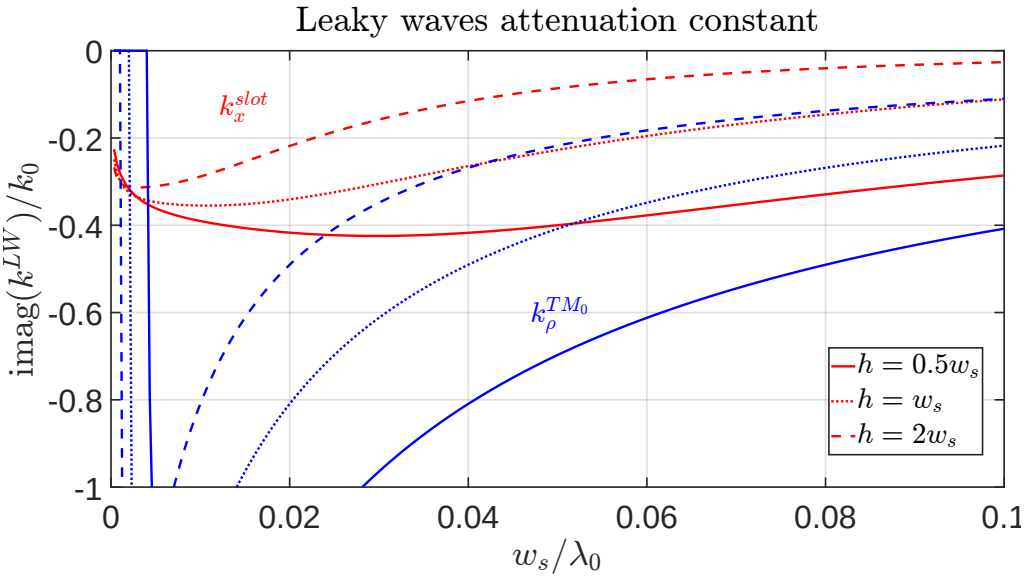

Figure 2.17: Attenuation constant of the leaky waves: $\varepsilon_r = 11.9, w_s = 100\mu$m, $\Delta_{gap} = 180\mu$m

Finally, the propagation constant of the both TM_0 and the slot mode is presented in Figures 2.16 and 2.17. These graphs show that the propagation constant of the slot mode behaves similarly as the thickness of the air-cavity is increased as the TM_0 mode. However, the values of the propagation constants for the two modes are quite different, which implies a non-symmetric

radiation pattern. The contributions of the poles in the far field are discussed in the next section.

2.3 Approximated contributions of the leaky waves

In this section, the approximated contributions of the leaky waves are evaluated in the far field. Since the contribution of a leaky wave defined as the residue of the electric field integrand evaluated in the pole does not exist in the far field, the contributions are obtained by using the approximation of the spectrum around the poles. The far field analysis is complemented with the analysis of the spectrum of the electric field which is presented first.

2.3.1 Spectrum of the electric field

As the far field is proportional to the spectrum of the electric field for $k_\rho \in [0, k_2]$, the analysis of the spectrum can lead to important insights into the behaviour of the antenna. Therefore, in this subsection, the electric field spectrum is studied.

The spectrum of the electric field is given as:

$$\vec{E}(k_\rho, \alpha, z) = \tilde{G}^{EM}(k_\rho, \alpha, z)\vec{M}(k_\rho, \alpha). \tag{2.36}$$

Approximating the spectrum around the poles, the approximated contributions of these poles are evaluated [10]:

$$\vec{E}^{TM_0}(k_\rho, \alpha, z) \approx \frac{2k_\rho^{TM_0}}{k_\rho^2 - {k_\rho^{TM_0}}^2} Res\Big(\tilde{G}^{EM}(k_\rho, \alpha, z)\vec{M}(k_\rho, \alpha)\Big)\Big|_{k_\rho = k_\rho^{TM_0}}, \tag{2.37}$$

$$\vec{E}^{slot}(k_\rho, \alpha, z) \approx \frac{2k_x^{slot}}{(k_\rho \cos\alpha)^2 - {k_x^{slot}}^2} Res\Big(\tilde{G}^{EM}(k_\rho, \alpha, z)\vec{M}(k_\rho, \alpha)\Big)\Big|_{k_\rho = \frac{k_x^{slot}}{\cos\alpha}}. \tag{2.38}$$

In order to demonstrate that the approximations of the pole contributions model the behaviour of the poles well, the spectrum of the y-component is plotted for $\alpha = 45°$ (D-plane in the far field) for the case $\varepsilon_r = 11.9, h = w_s = 100\mu\text{m} = 0.04\lambda_0$, $\Delta_{gap} = 180\mu\text{m}$ (Figure 2.18). As can be noted from these graphs, subtracting the approximated contributions of the poles from the total spectrum leads to the cancellation of the respective poles. Therefore, it can be concluded that the approximated contributions of the poles model the behaviour of the poles well.

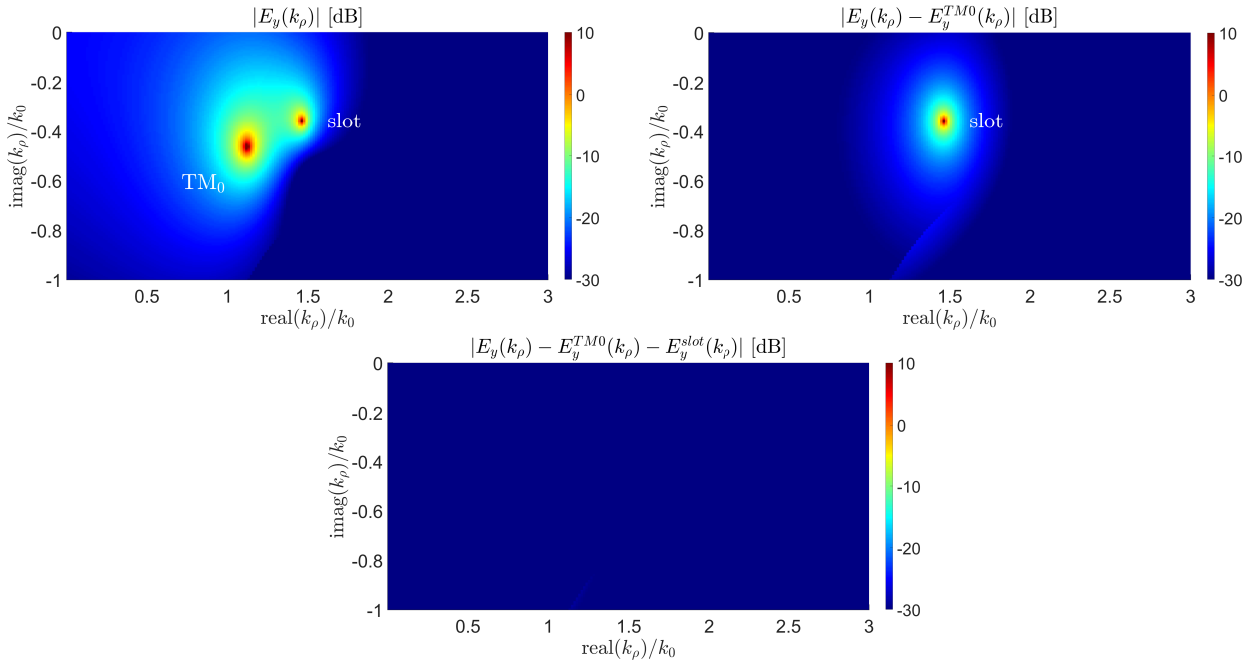

Figure 2.18: Spectrum of the y-component of the electric field for $\alpha = 45°$: $\varepsilon_r = 11.9, h = w_s = 100\mu\text{m} = 0.04\lambda_0$, $\Delta_{gap} = 180\mu\text{m}$

2.3.2 Far field

To obtain the contributions of the poles in the far field, the approximated expressions for the spectrum are used and evaluated asymptotically in the stationary phase point ($k_{\rho,s} = k_2 \sin\theta, k_{zs} = k_2 \cos\theta, \alpha_s = \phi$):

$$\vec{E}_{FF}^{TM_0}(\vec{r}) \approx jk_{zs}\frac{2k_\rho^{TM_0}}{k_{\rho,s}^2 - k_\rho^{TM_0\,2}} Res\Big(\tilde{G}^{EM}(k_\rho, \alpha_s, z)\vec{M}(k_\rho, \alpha_s)\Big)\Big|_{k_\rho = k_\rho^{TM_0}} \frac{\mathrm{e}^{-jkr}}{2\pi r}, \tag{2.39}$$

$$\vec{E}_{FF}^{slot}(\vec{r}) \approx jk_{zs}\frac{2k_x^{slot}}{(k_{\rho,s}\cos\alpha_s)^2 - k_x^{slot\,2}} Res\Big(\tilde{G}^{EM}(k_\rho, \alpha_s, z)\vec{M}(k_\rho, \alpha_s)\Big)\Big|_{k_\rho = \frac{k_x^{slot}}{\cos\alpha_s}} \frac{\mathrm{e}^{-jkr}}{2\pi r}. \tag{2.40}$$

Therefore, the total far field that is obtained using the standard definition:

$$\vec{E}_{FF}^{total}(\vec{r}) \approx jk_{zs}\tilde{G}^{EM}(k_{xs}, k_{ys}, z)\vec{M}(k_{xs}, k_{ys})\frac{\mathrm{e}^{-jkr}}{2\pi r}, \tag{2.41}$$

is equal to the summation of the pole contributions and a remaining term:

$$\vec{E}_{FF}^{total} \approx \vec{E}_{FF}^{remaining} + \vec{E}_{FF}^{TM_0} + \vec{E}_{FF}^{slot}. \tag{2.42}$$

Before the results of the far field are presented, an important characteristic of the two leaky wave modes can be noted inspecting the spectral Green's function given in Eq.(2.2) and the approximated contributions of the poles in the far field. As the residue in Eq.(2.39) is evaluated at $k_\rho^{TM_0}$, there is no contribution of the TE voltages. Therefore, TM_0 mode is a purely TM mode. However, since the slot mode appears as a pole of the magnetic current, the residue in Eq.(2.40) is equal to $\tilde{G}^{EM}(\frac{k_x^{slot}}{\cos\alpha_s}, \alpha_s, z)\dfrac{\vec{N}_M(\frac{k_x^{slot}}{\cos\alpha_s}, \alpha_s)}{D'_M(\frac{k_x^{slot}}{\cos\alpha_s}, \alpha_s)}$. From this expression, it is clear that both the TM and the TE solutions of the Green's function are contributing to the far field. Hence, it can be concluded that the slot mode is a hybrid mode.

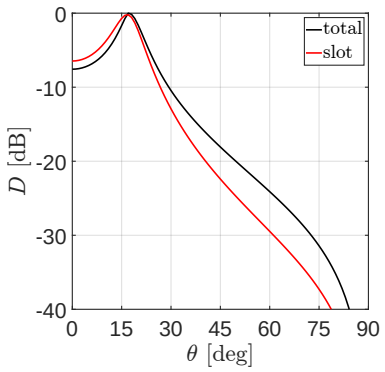

(a) H-plane

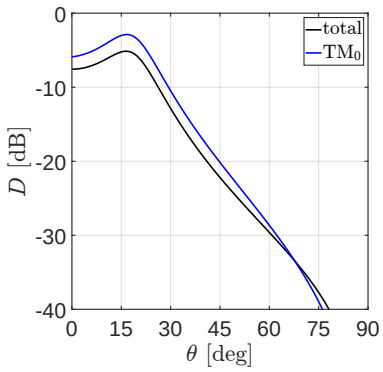

(b) E-plane

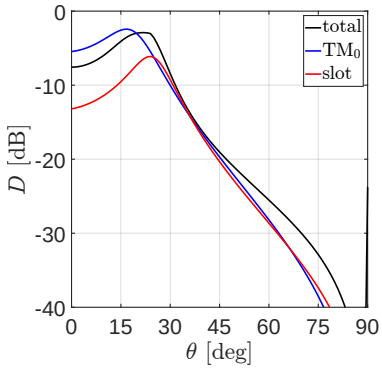

(c) D-plane: co. pol.

Figure 2.19: Directivity in the main planes: $\varepsilon_r = 11.9, h = w_s = 100\mu\text{m}$, $\Delta_{gap} = 180\mu\text{m}$

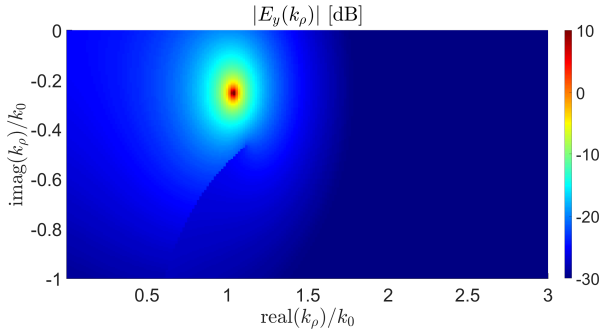

(a) $\alpha = 0°$

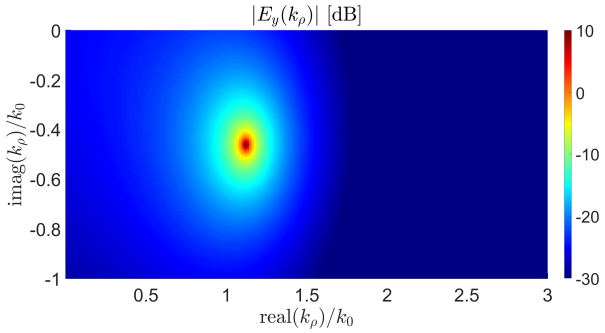

(b) $\alpha = 90°$

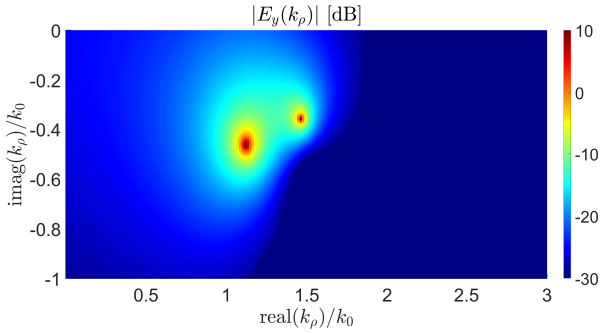

(c) $\alpha = 45°$

Figure 2.20: y-component of the electric field spectrum in the main planes: $\varepsilon_r = 11.9, h = w_s = 100\mu\text{m}$, $\Delta_{gap} = 180\mu\text{m}$

The normalised directivity in the main planes is presented in Figure 2.19, while the y-component of the electric field spectrum is plotted in Figure 2.20 ($\varepsilon_r = 11.9, h = w_s = 100\mu\text{m} = 0.04\lambda_0$,

$\Delta_{gap} = 180\mu$m). From these figures it can be seen that in the H-plane there is only the contribution of the slot mode, in E-plane the contribution of TM_0, while in D-plane both leaky waves are contributing. Furthermore, the TM_0 pole is constant in the spectrum, while the pole linked to the slot mode moves in the complex k_ρ plane. As a consequence, the pointing angle and the directivity of the slot contribution change with ϕ.

In Figure 2.21 cross polarised component in D-plane is plotted for $\varepsilon_r = 11.9, w_s = 100\mu$m$= 0.04\lambda_0$, $\Delta_{gap} = 180\mu$m and different values of the air-cavity thickness.

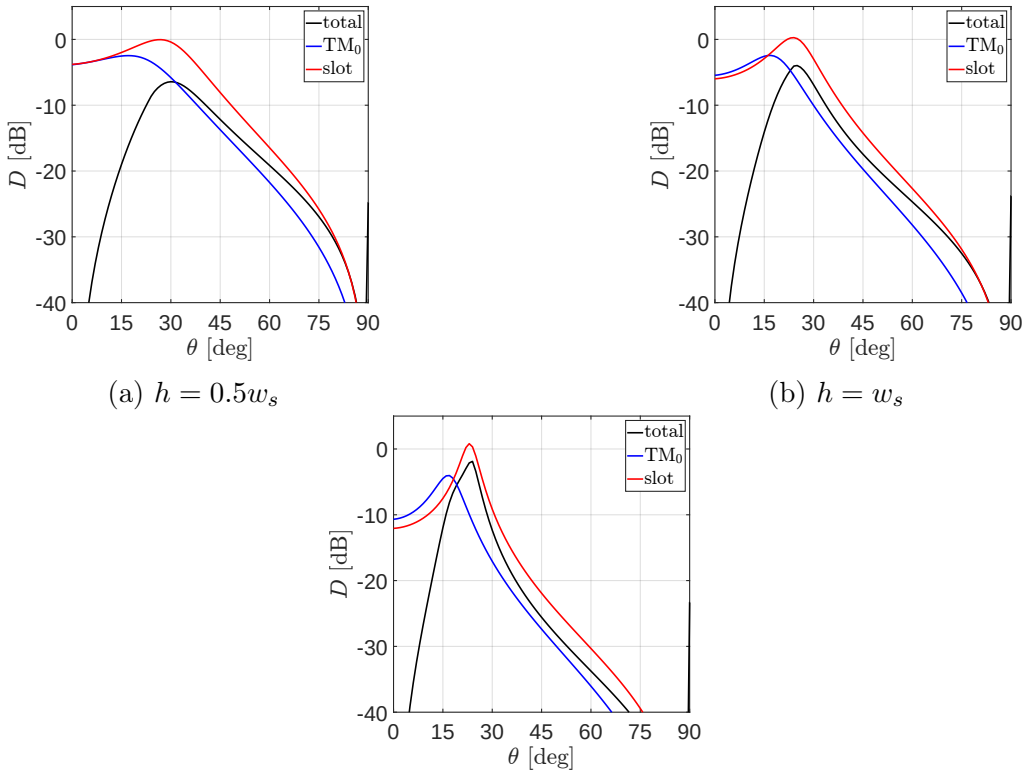

(a) $h = 0.5w_s$

(b) $h = w_s$

(c) $h = 2w_s$

Figure 2.21: Cross polarised component in D-plane: $\varepsilon_r = 11.9, h = w_s = 100\mu$m, $\Delta_{gap} = 180\mu$m

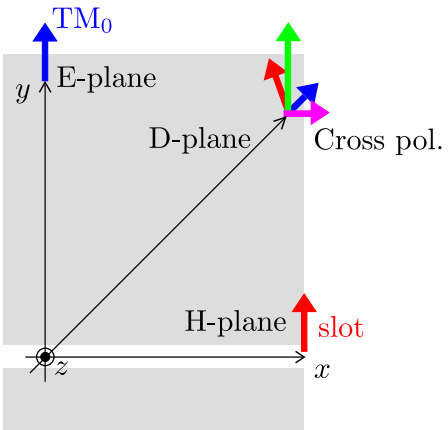

Figure 2.22: Illustration of the cross polarised component in D-plane

It is noted that the cross component is very high for the analysed values of h. This is a consequence of the two leaky wave contributions not having the same amplitude nor the same

pointing angle and therefore not canceling each other. In Figure 2.22 the cross component behaviour is illustrated additionally. Since the TM_0 mode is a purely TM mode, it is oriented along $\vec{i}_\rho$. However, being a hybrid mode, the slot mode is not strictly oriented along $\vec{i}_\phi$. Furthermore, the amplitudes of the mode contributions are not equal (as can also be noted in Figure 2.21). For these reasons, the analysed structure has a very high cross polarised component not only in D-plane but across a larger range of angle ϕ which can be noted in Figure 2.23. The demonstrated cross polarisation component motivates the slot tapering [2], [3].

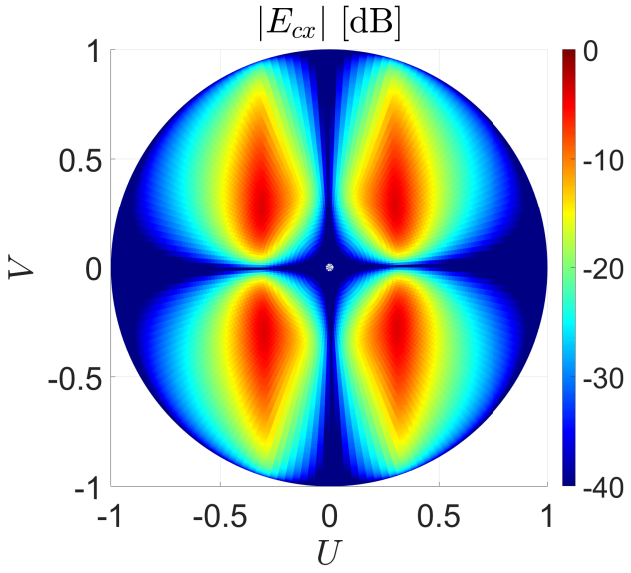

Figure 2.23: Cross polarised component of the total far field 2D: $\varepsilon_r = 11.9, h = w_s = 100\mu\text{m}$, $\Delta_{gap} = 180\mu\text{m}$

Chapter 3

Spectral analysis of the near field

In the previous chapter, spectral analysis of the leaky wave modes was performed which resulted in propagation constants of the leaky waves, magnetic current contributions and the approximated contributions of the modes in the far field. However, the analysis cannot be used to describe the behaviour of the slot mode in its entirety. For this reason, the spectral analysis of the near field is conducted. The procedure and its results are presented in the following chapter.

In Section 3.1, the procedure of solving the integral in α analytically is presented. This is done using an approximation on the phase of the magnetic current in order to avoid numerical calculation of the integral which would be very heavy computationally. Next, the singularities in k_ρ-plane and their behaviour are illustrated in Section 3.2. The integration paths for different planes are explained in Section 3.3, with verification of the results in Section 3.4.

3.1 Solving the integral in α

The double integral that this chapter is dedicated to solving is given in Eq.(2.1). Taking into the account that the slot is oriented along x-axis and performing the change of variables, this equation assumes the following form:

$$\vec{E}(\vec{r}) = \frac{1}{4\pi^2}\int_0^{2\pi}\int_0^{\infty} \tilde{G}^{EM}(k_\rho,\alpha,z)M_x(k_\rho,\alpha)\mathrm{e}^{-jk_\rho\rho\cos(\alpha-\phi)}k_\rho dk_\rho d\alpha. \tag{3.1}$$

The first approximation that can be made is to assume that the current is slow-varying in α compared to the phase term of the integrand $M_x(k_\rho,\alpha) \approx M_x(k_\rho,\phi)$[1]. This approximation is made in order to avoid the numerical closing of the integral in α, which would be very heavy numerically. The reason for it is that there is already one integral in M_x that is being solved numerically: integral in k_y (Eq.(2.30)).

After changing the order of integrals and taking the magnetic current out of the α integral (since it no longer depends on α), the expression becomes:

$$\vec{E}(\vec{r}) \approx \frac{1}{4\pi^2}\int_0^{\infty} M_x(k_\rho,\phi)\Big(\int_0^{2\pi} \tilde{G}^{EM}(k_\rho,\alpha,z)\mathrm{e}^{-jk_\rho\rho\cos(\alpha-\phi)}d\alpha\Big)k_\rho dk_\rho. \tag{3.2}$$

The remaining integral in α can be solved analytically and the steps of that derivation are given in Appendix A. After the integral in α is closed, the electric field expression can be presented as:

$$\vec{E}(\vec{r}) \approx \frac{1}{8\pi}\int_{-\infty}^{\infty} \tilde{G}^{EM}_{k_\rho}(k_\rho,\rho,z)M_x(k_\rho,\phi)k_\rho dk_\rho, \tag{3.3}$$

[1]The approximation on α of the magnetic current is discussed further in Section 3.4.

where $\tilde{G}_{k_\rho}^{EM}(k_\rho, \rho, z)$ is given in the form of its cylindrical components:

$$G_{k_\rho,\rho}^{EM}(k_\rho, \rho, z) = \sin\phi[v_{TE}(H_0^{(2)}(k_\rho\rho) + H_2^{(2)}(k_\rho\rho)) + v_{TM}(H_0^{(2)}(k_\rho\rho) - H_2^{(2)}(k_\rho\rho))], \tag{3.4}$$

$$G_{k_\rho,\phi}^{EM}(k_\rho, \rho, z) = \cos\phi[v_{TE}(H_0^{(2)}(k_\rho\rho) - H_2^{(2)}(k_\rho\rho)) + v_{TM}(H_0^{(2)}(k_\rho\rho) + H_2^{(2)}(k_\rho\rho))], \tag{3.5}$$

$$G_{k_\rho,z}^{EM}(k_\rho, \rho, z) = j2\sin\phi\frac{k_\rho v_{TM}}{k_{z2}}H_1^{(2)}(k_\rho\rho). \tag{3.6}$$

If the large-argument approximation on Hankel functions is assumed ($H_0^{(2)}(k_\rho\rho)+H_2^{(2)}(k_\rho\rho) \approx 0$ and $H_0^{(2)}(k_\rho\rho) - H_2^{(2)}(k_\rho\rho) \approx 2H_0^{(2)}(k_\rho\rho)$), the final expressions are as follows:

$$G_{k_\rho,\rho}^{EM}(k_\rho, \rho, z) \approx \sin\phi v_{TM}2H_0^{(2)}(k_\rho\rho), \tag{3.7}$$

$$G_{k_\rho,\phi}^{EM}(k_\rho, \rho, z) \approx \cos\phi v_{TE}2H_0^{(2)}(k_\rho\rho), \tag{3.8}$$

$$G_{k_\rho,z}^{EM}(k_\rho, \rho, z) = j2\sin\phi\frac{k_\rho v_{TM}}{k_{z2}}H_1^{(2)}(k_\rho\rho). \tag{3.9}$$

In order to perform the integration in k_ρ and obtain the electric field, it is important to take note of the singularities in k_ρ-plane. This is done in the next section.

3.2 Singularities in k_ρ-plane

Singularities of the integrand in Eq.(3.3) can stem both from the spectral Green's function and the magnetic current. These singularities are firstly illustrated separately in Figure 3.1.

$\tilde{G}_{k_\rho}^{EM}$ contains two singularities: branch-point $k_\rho = k_2$ and pole $k_\rho = k_\rho^{TM_0}$ (Figure 3.1a). There is only one branch-point and it comes from the upper semi-infinite medium (since only the $z > 0$ part of the transmission line in Figure 2.1 is solved to obtain currents and voltages that are inserted in the Green's function).

On the other hand, M_x has one pole $k_x = k_x^{slot}$ and three branch-points $k_x = k_0, k_x = k_2, k_x = k_\rho^{TM_0}$ [2] (Figure 3.1b). The branch points k_0 and k_2 come from the two semi-infinite media, which are both taken into account when calculating M_x (demonstrated in Section 2.2). $k_\rho^{TM_0}$ branch point comes form the TM_0 pole in Green's function. Since the slot is oriented along the x-axis, the singularities of the magnetic current are found in k_x. However, the integration Eq.(3.3) is performed in k_ρ. For that reason the singularities of M_x are presented in k_ρ-plane using the relation between the two planes $k_\rho = \frac{k_x}{\cos\phi}$ (Figure 3.1c).

Analysing the Figure 3.1, it can be noted that the singularities of the spectral Green's function do not depend on ϕ and are constant, while the singularities of the magnetic current change with ϕ as $\frac{1}{\cos\phi}$. This observation helps with understanding the differences in behaviours of the TM_0 and slot modes.

Finally, the singularities of M_x and $\tilde{G}_{k_\rho}^{EM}$ are not separated, but are existing simultaneously in k_ρ-plane. For an arbitrary angle ϕ, the k_ρ-plane is presented in Figure 3.2a. Planes E and H are special cases for which ϕ is equal to 90° and 0°, respectively. As can be noted from Figures 3.2b and 3.2c, E-plane only has the singularities of the Green's function, while H-plane contains

[2] Even though mentioned in this section, the branch-point $k_\rho^{TM_0}$ and its impact are not taken into account in the analysis that is put forward in this chapter since its contribution is negligible.

the singularities of the magnetic current.

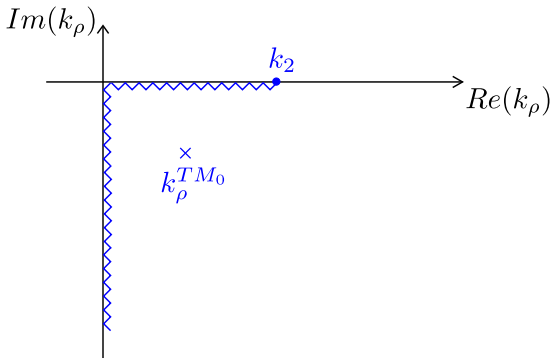

(a) Singularities of $\tilde{G}_{k_\rho}^{EM}$: k_ρ-plane

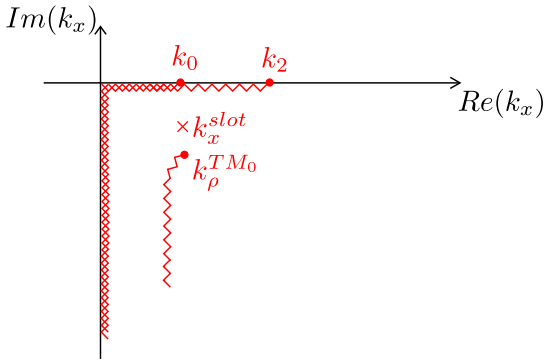

(b) Singularities of M_x: k_x-plane

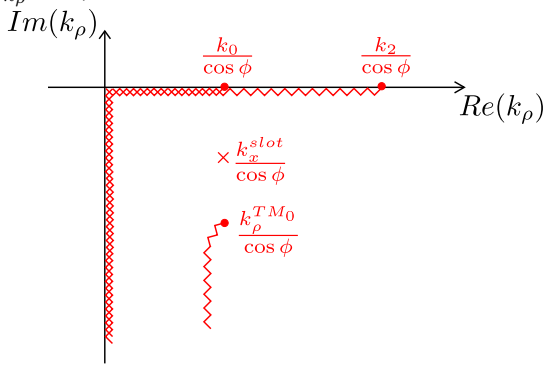

(c) Singularities of M_x: k_ρ-plane

Figure 3.1: Singularities of $\tilde{G}_{k_\rho}^{EM}$ and M_x

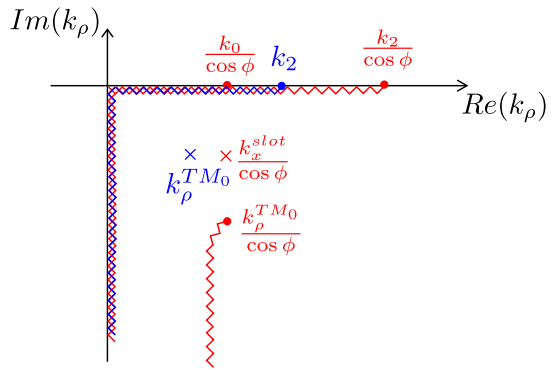

(a) Singularities in arbitrary plane

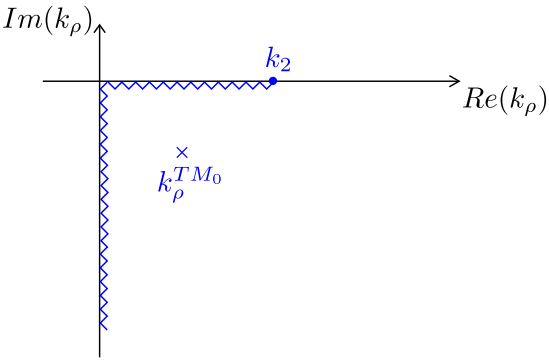

(b) Singularities in E-plane

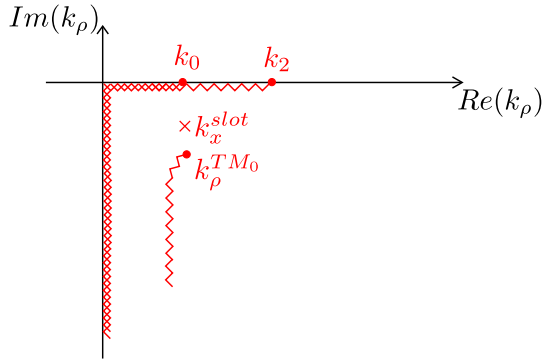

(c) Singularities in H-plane

Figure 3.2: Singularities in different planes

Having shown the k_ρ-plane and singularities in it, the next section describes how to integrate Eq.(3.3) in order to obtain the electric field.

3.3 Integration

As it was presented in the previous section, there are many singularities in k_ρ-plane. For an arbitrary angle ϕ, there are four branch-points and branch-cuts, and two poles. Before the integration for this case is put forward, for the sake of simplicity, the main principle behind it is explained with an example with less singularities.

For this demonstration, the goal is to calculate the electric field:

$$\vec{E}(\vec{r}) = \int_{-\infty}^{\infty} f(k_\rho) dk_\rho, \tag{3.10}$$

where $f(k_\rho)$ is a function that contains two singularities in k_ρ-plane: one branch-point $k_\rho = k_{branch}$ and one pole $k_\rho = k_{pole}$.

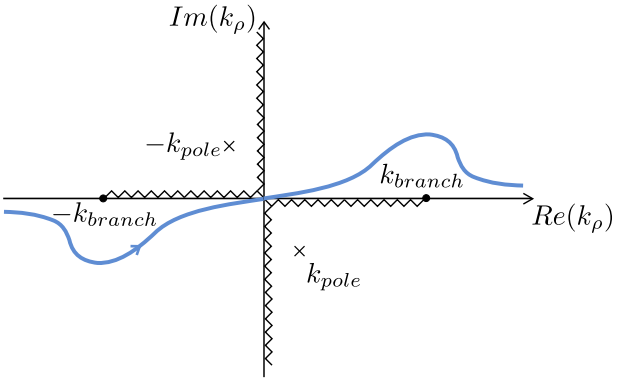

(a) Original integration path

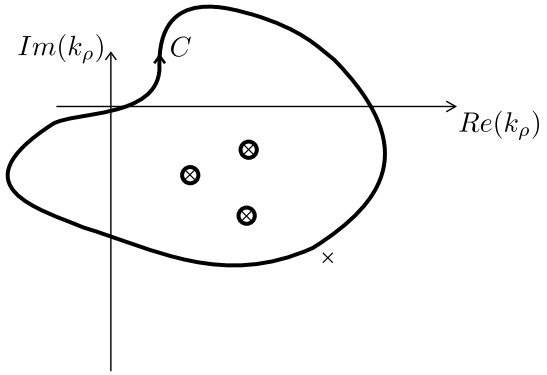

(b) Cauchy's residue theorem

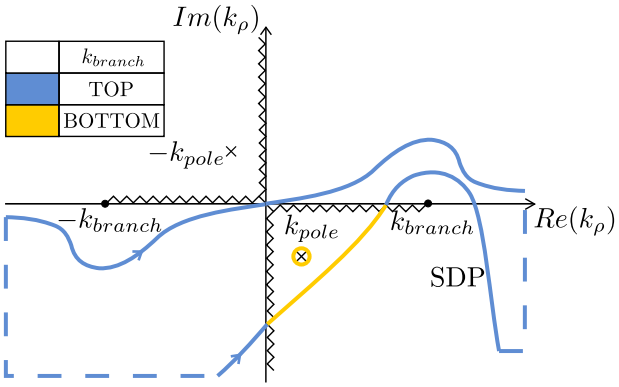

(c) Deformed integration path

Figure 3.3: Applying Cauchy's residue theorem

One possible integration path is presented in Figure 3.3a. It is slightly modified from the real-axis path in order to avoid the branch-points, and is entirely on the top Riemann sheet of k_{branch}. This integration results in the total field, but it does not give any information about the separate contributions of the pole and the branch.

In order to obtain different contributions to the total field, the Cauchy's residue theorem is used [11]. This theorem says that if the integration is performed over a closed contour C, then that is equal to the residue contributions of the poles that the contour is enclosing (Eq.(3.11), Figure 3.3b).

$$\int_C f(k_\rho)dk_\rho = 2\pi j \sum_{k=1}^{n} \text{Res}_{k_\rho=k_{\rho,k}} f(k_\rho) \tag{3.11}$$

Going back to the example and minding the crossing of the branch, the SDP (Steepest Descent Path)[3] is added to the original integration path in order to form a closed contour (Figure 3.3c). It is important to note that in order for the two paths to form a closed contour, they need to be in the same Riemann sheet with respect to k_{branch} at the points where they meet. The contributions of the two integration paths can be written as:

$$\text{Original path integration} - \text{SDP integration} = \text{pole contribution}, \tag{3.12}$$

$$\text{Original path integration} = \text{SDP integration} + \text{pole contribution}, \tag{3.13}$$

where the minus sign in front of the SDP contribution comes from the reverse direction of the path with respect to the one of the original path. It can be noted from Eq.(3.13) that the deformed integration path gives the total electric field, but it also provides with the separate contributions of the SDP and the pole.

In the upcoming subsections, the explained method is used in order to define the integration paths in different planes and obtain the electric field results. The definition of the SDP and how the Riemann sheets with respect to different branch-cuts are chosen are given in Appendix B, while the residual contributions of the modes and their shadow boundary angles are presented in Appendix C.

3.3.1 E-plane

As was previously noted in Figure 3.2b, there are only singularities of the spectral Green's function in E-plane: one branch-point and one pole. Hence, the integration path chosen is very similar to the example given at the beginning of this section. This integration path is illustrated in Figure 3.4.

When the angle θ is smaller than the shadow boundary angle of the TM_0 mode, the TM_0 pole is not captured (Figure 3.4a). After θ becomes larger than $\theta_{SB}^{TM_0}$, the pole is crossed and its contribution can be separated as the residue of the integrand evaluated at $k_\rho = k_\rho^{TM_0}$. The Riemann sheets in which the integration path is changes as the branch-cuts are crossed.

In order to illustrate the results obtained with these integration paths, the electric field is calculated on the surface of the sphere center of which is located bellow the ground plane (Figure 3.5). The coordinate system is chosen as such because it is known that antennas like the one that is being analysed have their phase center bellow the ground plane [12]. Furthermore, the parameters of the antenna are $h = w_s = 0.04\lambda_0, \varepsilon_r = 11.9$.[4]

[3] SDP is defined in detail in Appendix B.

[4] These parameters are used throughout this chapter.

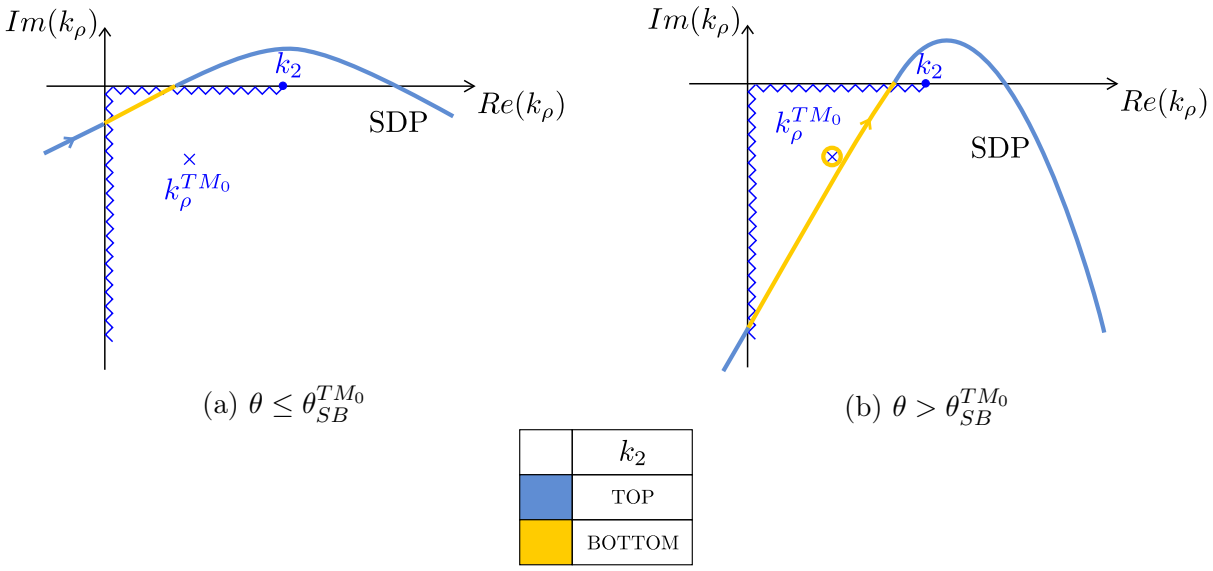

(a) $\theta \leq \theta_{SB}^{TM_0}$

(b) $\theta > \theta_{SB}^{TM_0}$

(c) Riemann sheet legend

Figure 3.4: Integration in E-plane

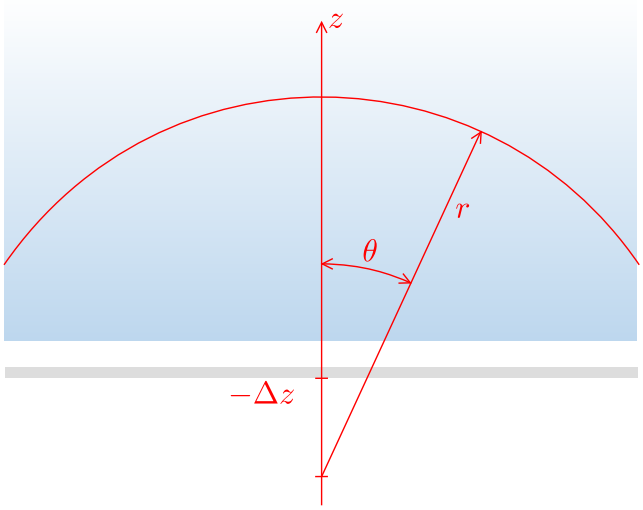

Figure 3.5: Near-field sphere

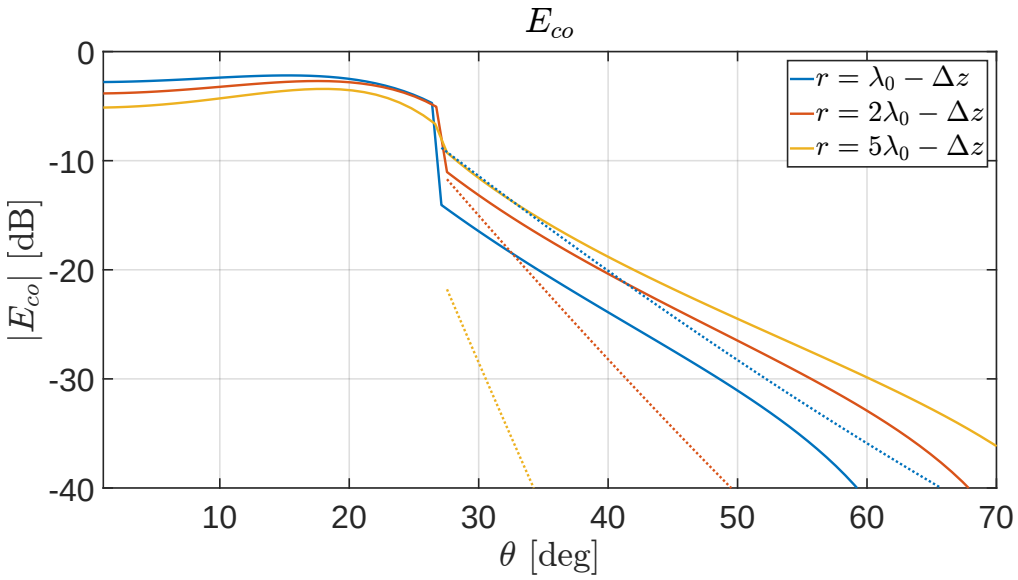

(a) Contributions to the electric field (solid: SDP, dot: TM_0)

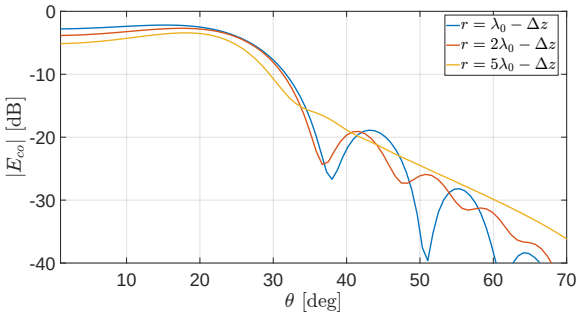

(b) Total electric field obtained by summing the contributions (SDP+TM_0)

Figure 3.6: Electric field in E-plane

In Figure 3.6a, the contributions of the electric field are plotted. As can be noted, up until a certain angle θ (shadow boundary angle of TM_0), there is only the contribution of SDP, which corresponds to the integration path in Figure 3.4a. At $\theta = \theta_{SB}^{TM_0}$, the SDP contribution is discontinuous. Above that angle, the contribution of the TM_0 pole is added (integration path Figure 3.4b). In order to demonstrate that these contributions result in a continuous field, their summation is plotted in Figure 3.6b.

3.3.2 H-plane

Compared to the E-plane, H-plane has two branch-points more that need to be taken into account when integrating. In Figure 3.7, the integration paths for H-plane are presented.

When $\theta \leq \beta_0^H, \theta_{SB}^{slot,H}$ (β_0^H, $\theta_{SB}^{slot,H}$ are β_0, θ_{SB}^{slot} evaluated for $\phi = 0°$, respectively, where $\beta_0 = \arcsin \frac{k_\rho}{k_0/\cos\phi}$[5]), the integration path is illustrated in Figure 3.7a. As can be seen, the integration path crosses the real-axis for the first time on the left-hand side of k_0 and the pole is not captured. However, when θ becomes larger than β_0^H, in order to close the contour with the original integration path (Figure 3.3c), k_0 branch contribution needs to be added to SDP. This way, starting from the top Riemann sheets of the both branch-cuts and changing the Riemann sheets when the branch-cuts are crossed, the SDP ends in top Riemann sheets too (Figure 3.7b). Additionally, when θ gets larger than the shadow boundary angle of the slot

[5]Appendix B.

mode, its contribution is added (Figure 3.7c).

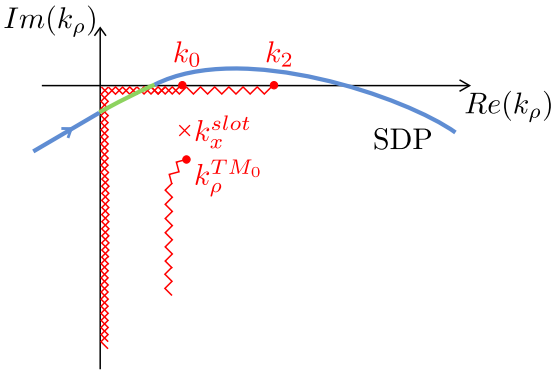

(a) $\theta \leq \beta_0^H, \theta_{SB}^{slot,H}$

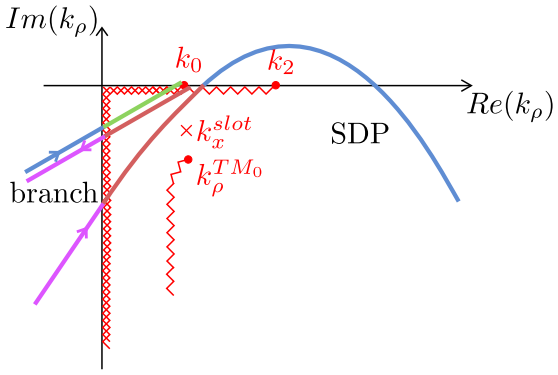

(b) $\theta > \beta_0^H, \theta \leq \theta_{SB}^{slot,H}$

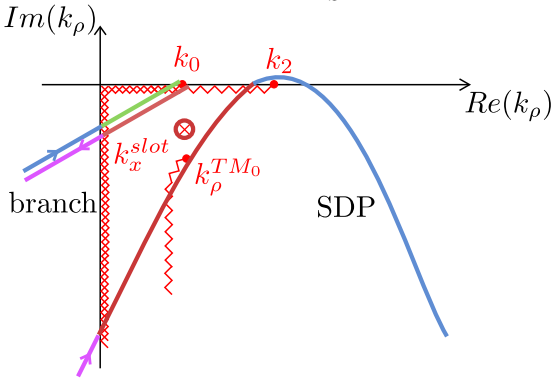

(c) $\theta > \beta_0^H, \theta_{SB}^{slot,H}$

	k_0	k_2
	TOP	TOP
	BOTTOM	BOTTOM
	TOP	BOTTOM
	BOTTOM	TOP

(d) Riemann sheets legend

Figure 3.7: Integration in H-plane

The electric field results are plotted in Figure 3.8. Firstly, the contribution of the pole and summed up contributions of SDP and branch are presented (Figure 3.8a). Similar to the E-plane, bellow the shadow boundary angle (of the slot mode), there is no contribution of the pole. The slot mode starts contributing explicitly for $\theta > \theta_{SB}^{slot,H}$ (corresponding to the integration path Figure 3.7c). As a confirmation, the summation of all the contributions is shown in Figure 3.8b where it can be noted that they result in a continuous field.

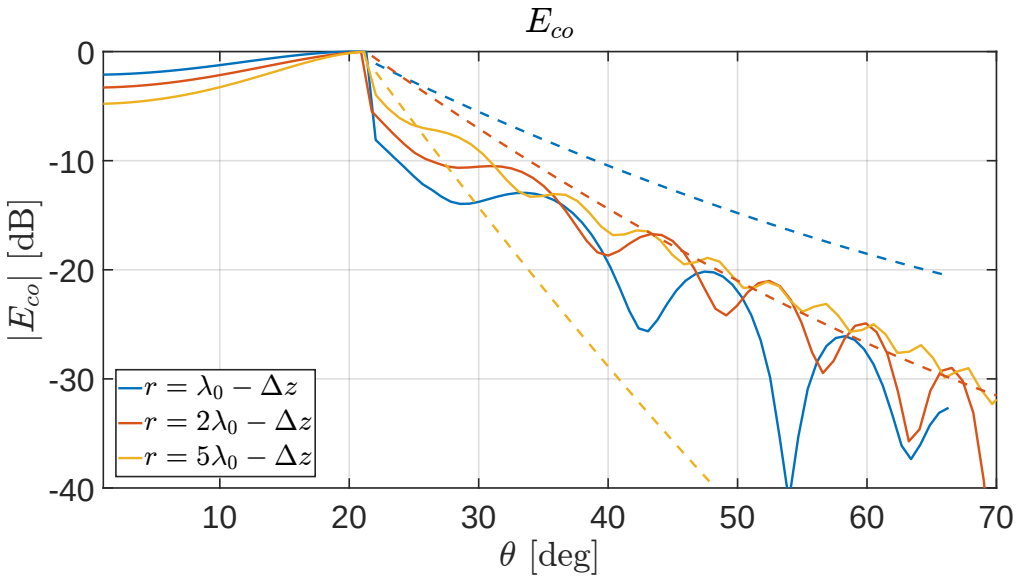

(a) Contributions to the electric field (solid: SDP+branch, dash: slot)

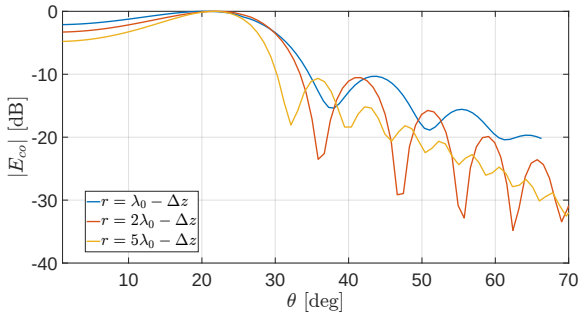

(b) Total electric field obtained by summing the contributions (SDP+branch+slot)

Figure 3.8: Electric field in H-plane

3.3.3 Arbitrary plane

Singularities in k_ρ-plane for an arbitrary plane were illustrated in Figure 3.2a. In order to perform the integration for an arbitrary ϕ, all of these singularities need to be navigated around. Different cases are presented in Figure 3.9.

In Figure 3.9a, the integration path is presented for when no poles are captured and angle θ is smaller than $\beta_0(\phi)$ (as defined in Appendix B). The SDP starts on the top Riemann sheet for all three branch-cuts and after crossing them all twice, goes back to the top Riemann sheets. When θ becomes larger than $\beta_0(\phi)$, similarly to the integration in H-plane, $\frac{k_0}{\cos\phi}$ contribution is added, minding the crossings of all three branch-cuts (Figure 3.9b). Furthermore, for $\theta > \beta_0(\phi), \theta_{SB}^{TM_0}, \theta_{SB}^{slot}(\phi)$, the poles of both modes are captured in bottom Riemann sheets of k_2 and $\frac{k_2}{\cos\phi}$ and top Riemann sheet of $\frac{k_0}{\cos\phi}$ (Figure 3.9d).

However, as angle ϕ increases in value, two things can be observed. Firstly, for $\beta_0(\phi) > \theta_{SB}^{TM_0}$, TM_0 pole is captured in the bottom Riemann sheets of all three branch-cuts. This effects the way the residual contribution of the mode is calculated (Appendix C). Secondly, above a certain angle ϕ, the slot mode is not captured and it does not explicitly contribute to the field. This angle corresponds to ϕ for which the shadow boundary angle of the slot mode becomes larger than 90°.

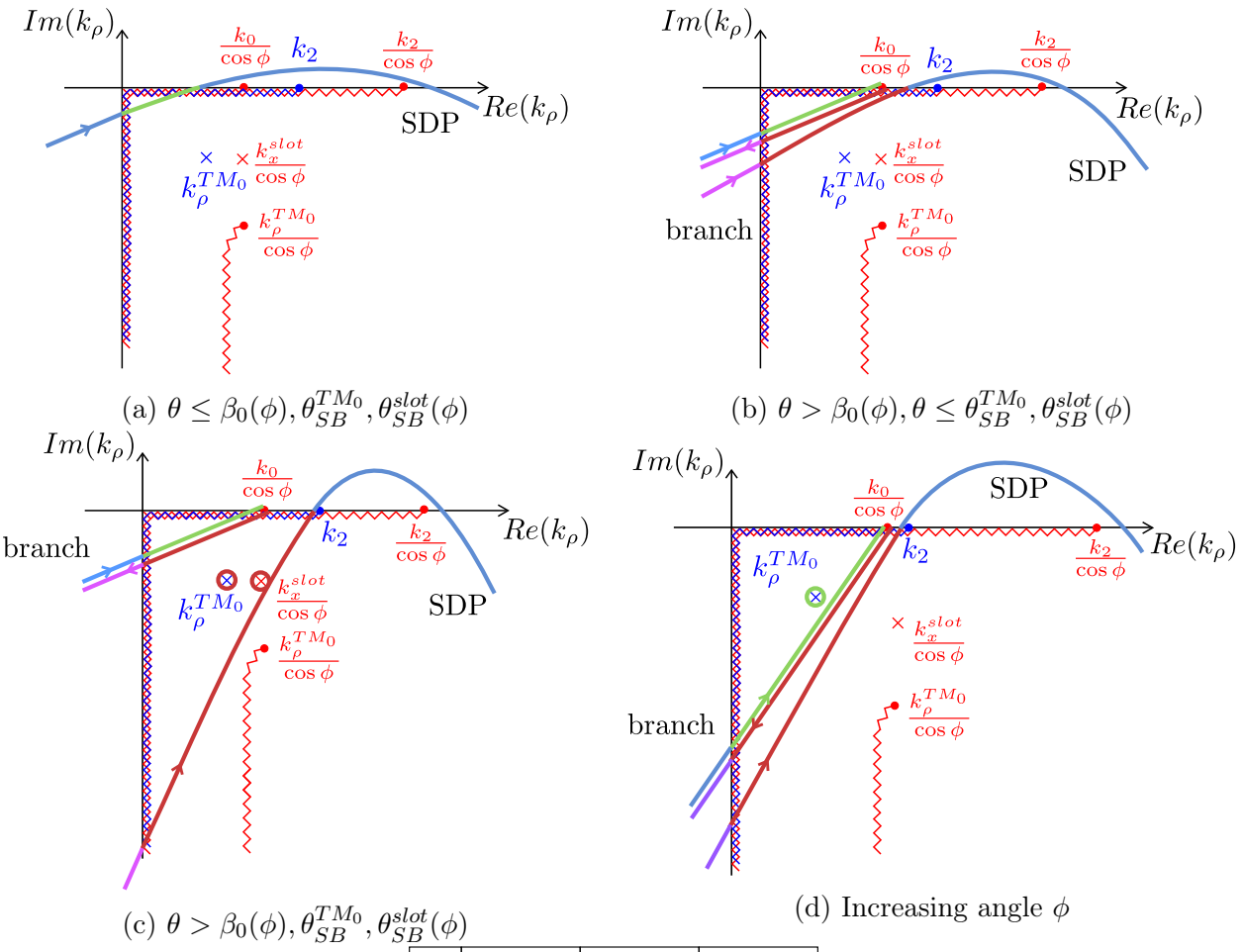

(a) $\theta \leq \beta_0(\phi), \theta_{SB}^{TM_0}, \theta_{SB}^{slot}(\phi)$

(b) $\theta > \beta_0(\phi), \theta \leq \theta_{SB}^{TM_0}, \theta_{SB}^{slot}(\phi)$

(c) $\theta > \beta_0(\phi), \theta_{SB}^{TM_0}, \theta_{SB}^{slot}(\phi)$

(d) Increasing angle ϕ

	k_2	$k_0/cos\phi$	$k_2/cos\phi$
	TOP	TOP	TOP
	BOTTOM	BOTTOM	BOTTOM
	BOTTOM	TOP	BOTTOM
	TOP	BOTTOM	TOP
	TOP	TOP	BOTTOM
	TOP	BOTTOM	BOTTOM

(e) Riemann sheets legend

Figure 3.9: Integration in an arbitrary plane

In the above-presented figures, the second time that the SDP crosses the real-axis is always after $\frac{k_2}{\cos\phi}$, assuring that the integration path ends in top Riemann sheets for all three branch-cuts. However, this is not the case for all θ. As is discussed in Appendix B, the SDP is defined around k_2 branch. As θ grows larger, the SDP becomes steeper and the points where it crosses the real-axis get closer to k_2. The integration paths that take into account these additional crossings of the branches are illustrated in Figure 3.10.

If only the $\frac{k_2}{\cos\phi}$ branch-cut is crossed above k_2 branch-point, the integration path is presented in Figure 3.10a. In order to form a closed contour with the original path (as discussed at the beginning of this section), contribution of the $\frac{k_2}{\cos\phi}$ branch should be added. Similarly, in Figure 3.10b the integration path is presented when the contributions of both $\frac{k_2}{\cos\phi}$ and $\frac{k_0}{\cos\phi}$ should be added. However, the integration paths given with dashed lines are not implemented in the code used to obtain the results, since their contribution is negligible.

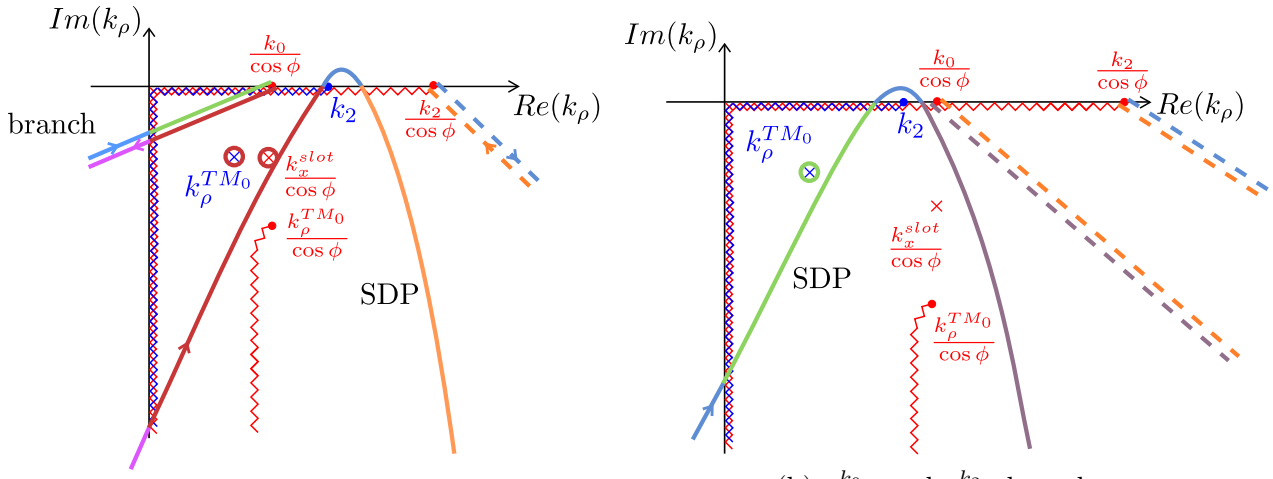

(a) $\frac{k_2}{\cos\phi}$ branch

(b) $\frac{k_0}{\cos\phi}$ and $\frac{k_2}{\cos\phi}$ branches

Figure 3.10: Additional branches

To demonstrate the results obtained for an arbitrary angle ϕ, electric field in D-plane is plotted in Figure 3.11. Firstly, the separate contributions are plotted: TM_0 mode, slot mode and SDP together with the branch contribution. Co. and cx. components are presented in Figures 3.11a and 3.11b, respectively. As can be noted, the two modes start contributing at different angles θ, since their shadow boundary angles are different. Furthermore, they do not have the same spreading term. These differences between the modes are the reason for the high cx. pol and the asymmetry of the radiation pattern. Finally, in Figures 3.11c and 3.11d the electric field obtained when all the contributions are summed up is plotted, showing that the resulting field is continuous.

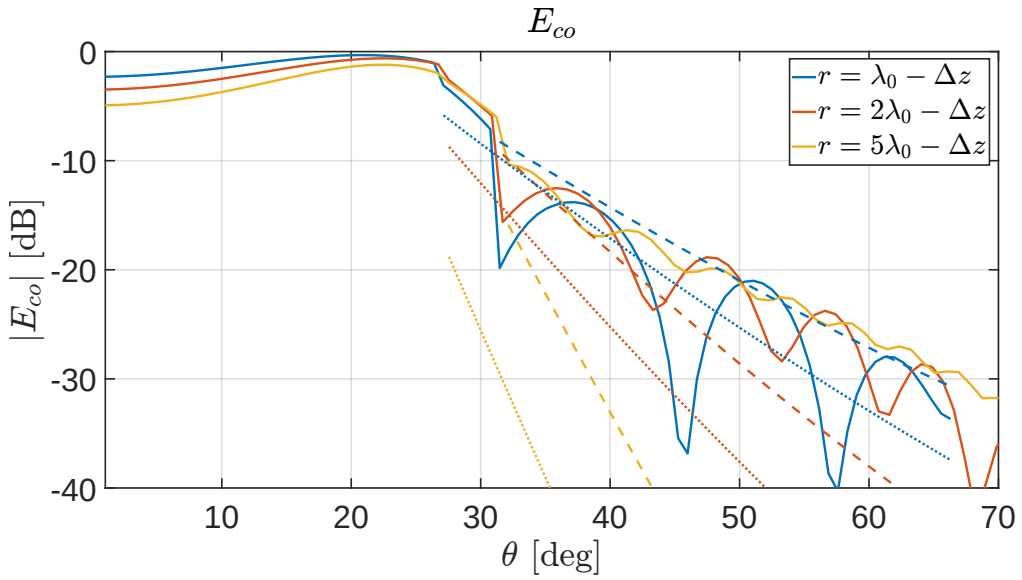

(a) Contributions to the electric field: co. (solid: SDP+branch, dash: slot, dot: TM_0)

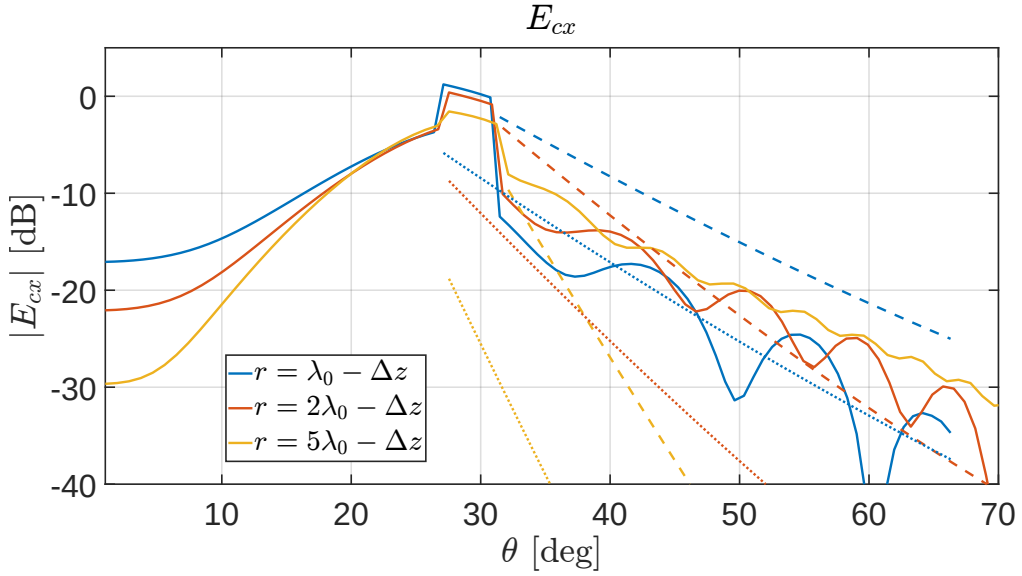

(b) Contributions to the electric field: cx. (solid: SDP+branch, dash: slot, dot: TM_0)

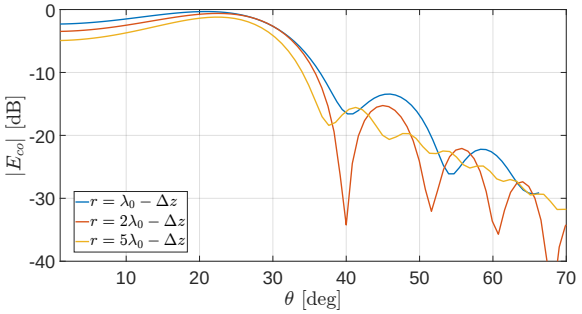

(c) Total electric field obtained by summing the contributions: co. (SDP+branch+slot+TM_0)

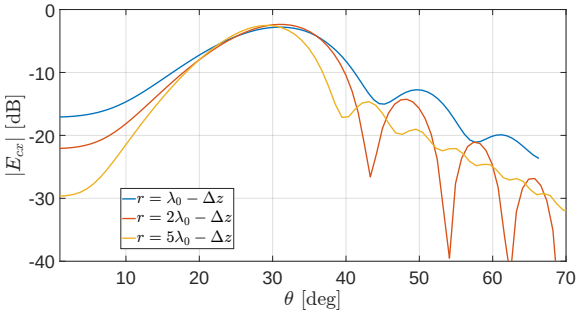

(d) Total electric field obtained by summing the contributions: cx. (SDP+branch+slot+TM_0)

Figure 3.11: Electric field in D-plane

3.4 Verification

In the following section, the verification of the electric field results is presented. Comparison is performed with respect to the real-axis integration of Eq.(3.3) and the results obtained with

CST.[6]

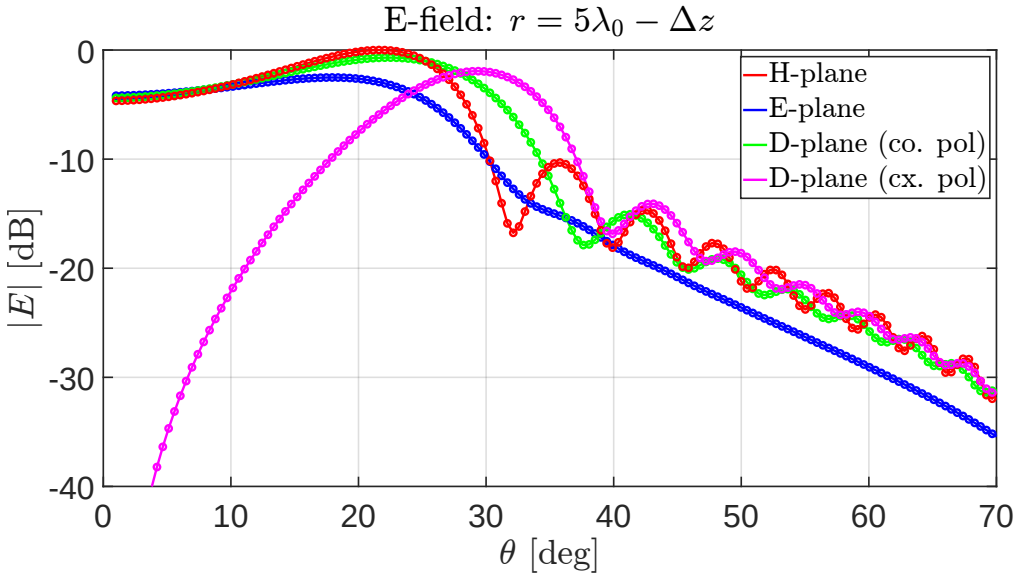

(a) Comparison to the real-axis integration (solid: summation of contributions, circles: real-axis integration)

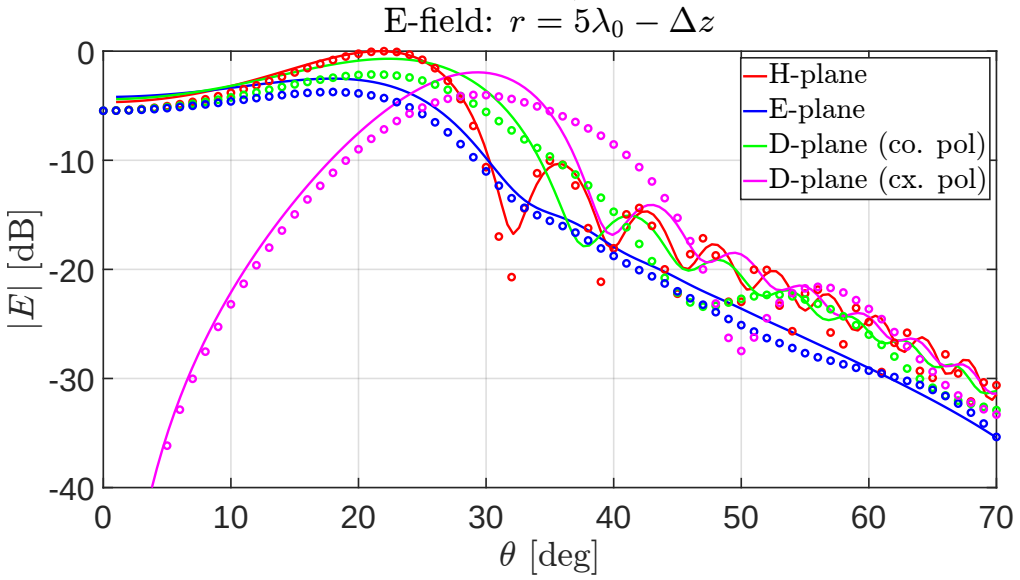

(b) Comparison to the CST results (solid: summation of contributions, circles: CST)

Figure 3.12: Verification of the electric field

The real-axis integration is slightly deformed so as to avoid the branch-points laying on the real-axis and is given with the expression $k_\rho^{path} = k_\rho + 0.01je^{-\frac{1}{2}(\frac{k_\rho}{k_2})^2}$. As was mentioned previously, this integration path results in the total electric field. The summation of the separate contributions presented in the previous section is compared to the total electric field in Figure 3.12a. It can be noted that the agreement between the two integration paths is perfect. This means that the complex analysis and the integration paths presented in Section 3.3 are correct.

On the other hand, in Figure 3.12b the results are compared to the ones obtained with full

[6]The results presented in this section are obtained without using the large-argument approximation on the Hankel functions from Section 3.1.

wave CST simulation. As can be seen, the match is not perfect for such a small r. This was expected due to the approximation made on the magnetic current $M_x(k_\rho, \alpha) \approx M_x(k_\rho, \phi)$ which is pretty rough considering that the current contains singularities. However, this choice was made so as to not perform numerical closing of the integral in α which would be very demanding numerically. Finally, even though the match is not perfect for smaller values of r, the insight into the behaviour of the modes and how they contribute to the field that is gained with the spectral analysis of the near field performed is valid.

Chapter 4

Leaky wave antenna with multiple slots

In the previous chapter, using the spectral analysis of the near field, TM_0 and slot modes were characterised and an insight into the behaviour of these modes was presented. However, as was discussed in Chapter 2, the main problem of the infinite slot leaky wave antenna remains unsolved: high cross pol. component. Once again, this is demonstrated in Figure 4.1 for $h = w_s = 0.02\lambda_{0c}$[1] and it can be noted that the cross pol. in D-plane is around -7dB, which represents a strong interference.[2]

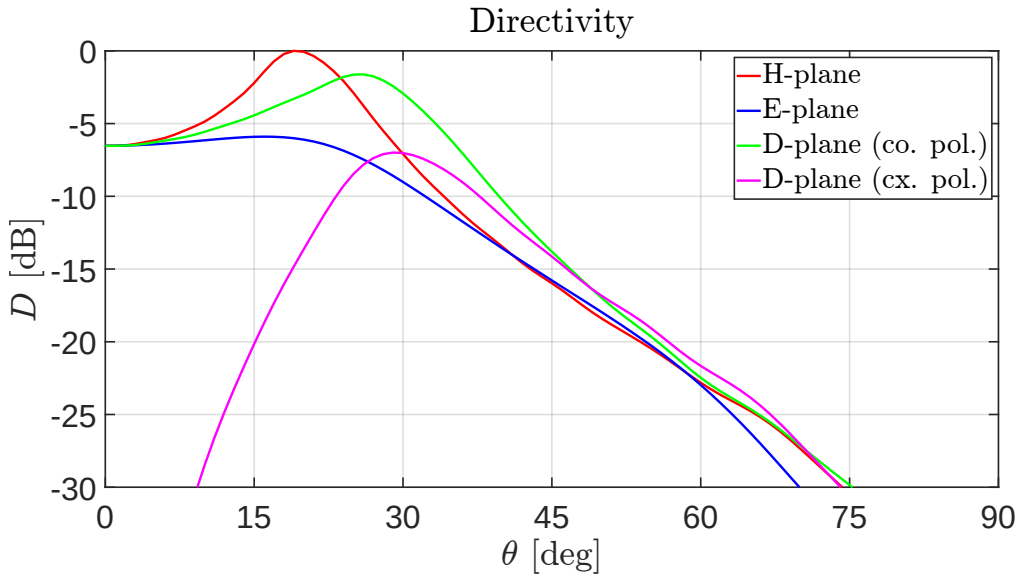

Figure 4.1: Directivity of the infinite slot LWA: $\varepsilon_r = 11.9, h = w_s = 0.02\lambda_{0c}$

In the next section, the current state of the art feeds of leaky lens antenna that suppress the cross pol. are presented and analysed.

4.1 Tapered slot

Up until this point, the most effective way to deal with high cross pol. has been to taper the slot, as presented in [2], [3]. The slot is then defined through the tapering angle γ_{tap} illustrated in Figure 4.2. Due to this widening of the slot, the space wave becomes more dominant and the contribution of the slot leaky wave becomes weaker. Therefore, since the slot mode is the

[1] Throughout this chapter, λ_{0c} corresponds to the central frequency of $f = 15$ GHz.

[2] If not stated otherwise, the radiation patterns presented in this chapter are at the central frequency. Furthermore, all the radiation patterns are obtained via full wave CST simulations.

mode with the stronger cross pol. contribution (as discussed in Subsection 2.3.2), it is expected that the cross pol. would get smaller with tapering of the slot.

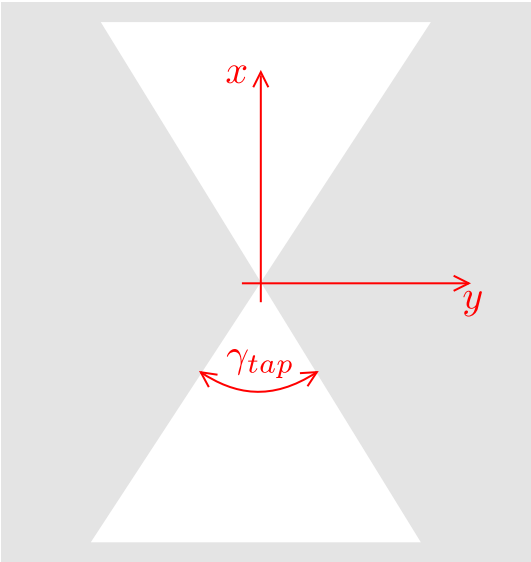

Figure 4.2: Tapered slot

In order to demonstrate the effect of tapering the slot on the far field of the antenna, two designs are compared:

1. Height $h = 0.02\lambda_0$, tapering angle $\gamma_{tap} = 30^\circ$ [2],
2. Height $h = 0.016\lambda_0$, tapering angle $\gamma_{tap} = 70^\circ$ [3].

The far fields of these two designs are presented in Figure 4.3. As can be noted, the fields in H and D-planes are more symmetric than that of a slot without the taper and the cross pol. in D-plane is lower: for $h = 0.02\lambda_{0c}$, $\gamma_{tap} = 30^\circ$ the cross pol. is approximately -10dB, while for $h = 0.016\lambda_{0c}$, $\gamma_{tap} = 70^\circ$ it is around -14dB. It should also be noted that the antenna with smaller air-cavity is less directive and its pattern is broader in θ, which is an important metric if such an antenna is used as a feed to a lens. Furthermore, the cross pol. of this antenna is suppressed more not only due to the tapering of the slot, but also because of the fact that the modes are very weak for lower values of h (as can be clearly noted from Figure 2.17).

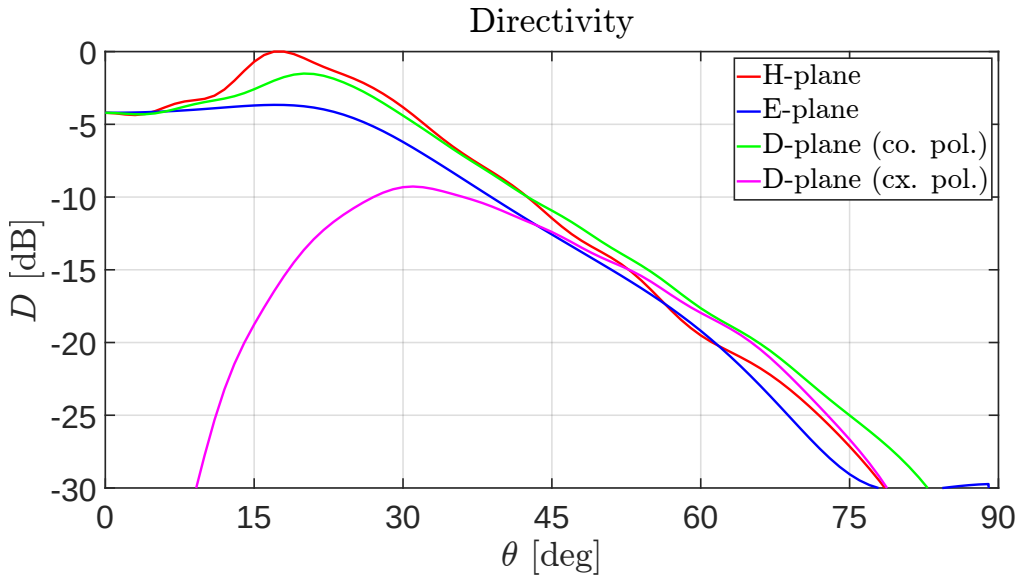

(a) $h = 0.02\lambda_{0c}$, $\gamma_{tap} = 30°$, $\varepsilon_r = 11.9$

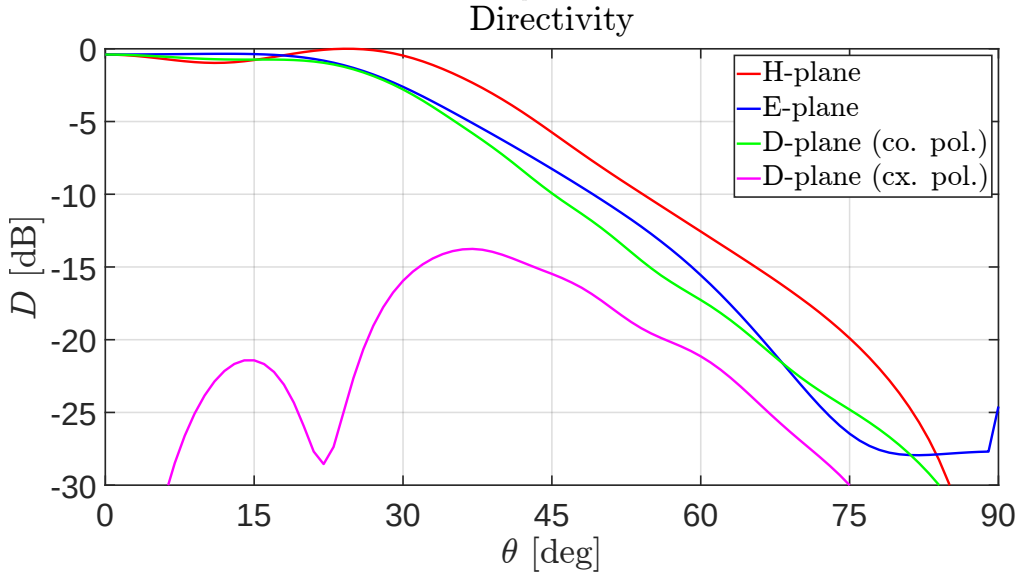

(b) $h = 0.016\lambda_{0c}$, $\gamma_{tap} = 70°$, $\varepsilon_r = 11.9$

Figure 4.3: Directivity of the tapered slot antennas

The level of cross pol. component can also be quantified with the cross pol. efficiency that is defined as:

$$\eta_{cx} = \frac{\int_0^{2\pi}\int_0^{\frac{\pi}{2}} |\vec{E}_{FF}^{co}(\theta,\phi)|^2 \sin\theta d\theta d\phi}{\int_0^{2\pi}\int_0^{\frac{\pi}{2}} |\vec{E}_{FF}(\theta,\phi)|^2 \sin\theta d\theta d\phi}. \tag{4.1}$$

This efficiency is plotted for the non-tapered slot and the two tapered antennas in Figure 4.4. As was expected, the efficiency is increased drastically with the taper. However, as was mentioned at the beginning of this section, increasing the taper eventually leads to losing the slot mode to the space wave. In the next section, a new geometry is presented to deal with high cross pol. while maintaining the leaky wave modes.

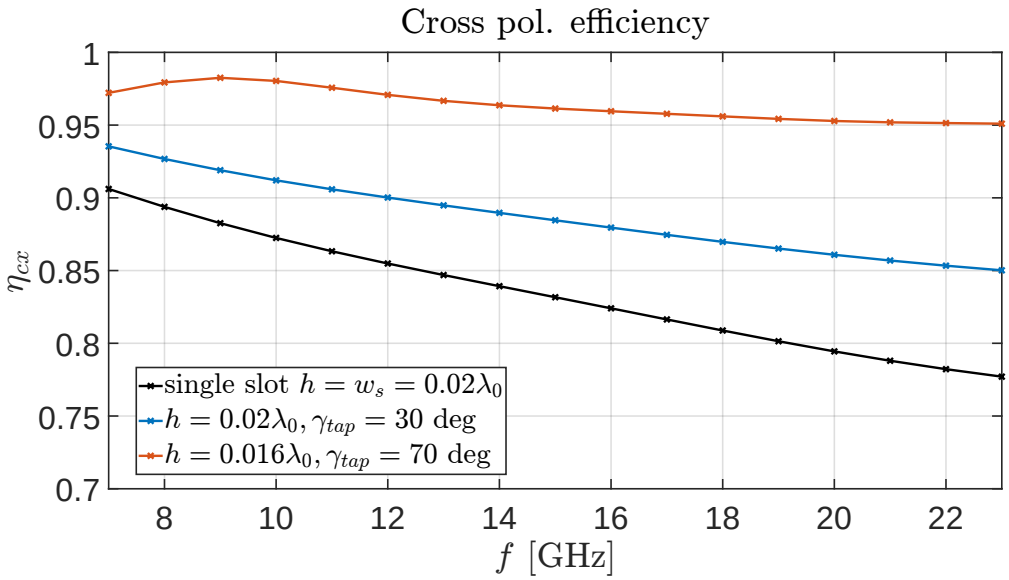

Figure 4.4: Cross pol. efficiency: non-tapered vs. tapered slot

4.2 Introduction of the LWA with multiple slots

As was demonstrated in the previous section, both tapering the slot and decreasing the thickness of the air-cavity contribute to lowering the level of cross pol. This effect is a consequence of removing the leaky wave components in the current. Since the leaky waves are by design made to be weak, the space wave is the most dominant component of the field which leads to less directive radiation patterns (Section 2.2). On the other hand, if there is no taper and the air-cavity is large, the TM_0 and slot modes are non-symmetric in ϕ leading to a high cross pol. component. In this section, the idea of obtaining more symmetrical contributions of the TM_0 and slot modes by adding additional slots is explored.

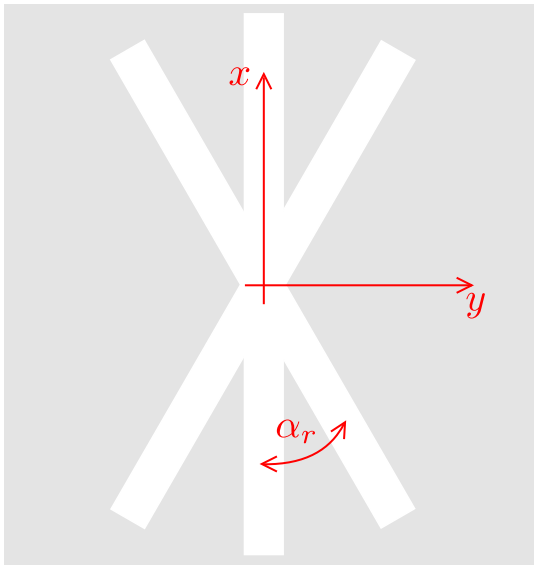

Figure 4.5: LWA with three slots

As an example of the leaky wave antenna with multiple slots, triple slot antenna is illustrated in Figure 4.5. Additional to the slot along the x-axis, the triple slot antenna consists of two other slots that are rotated in xy-plane by an angle α_r. This structure is fed by a delta-gap

generator in the center with the goal of exciting the slot mode in all three slots. Therefore, using the insight about the behaviour of the slot mode gained in the work presented previously, the shape of the radiation pattern can be modified w.r.t. the single slot antenna.

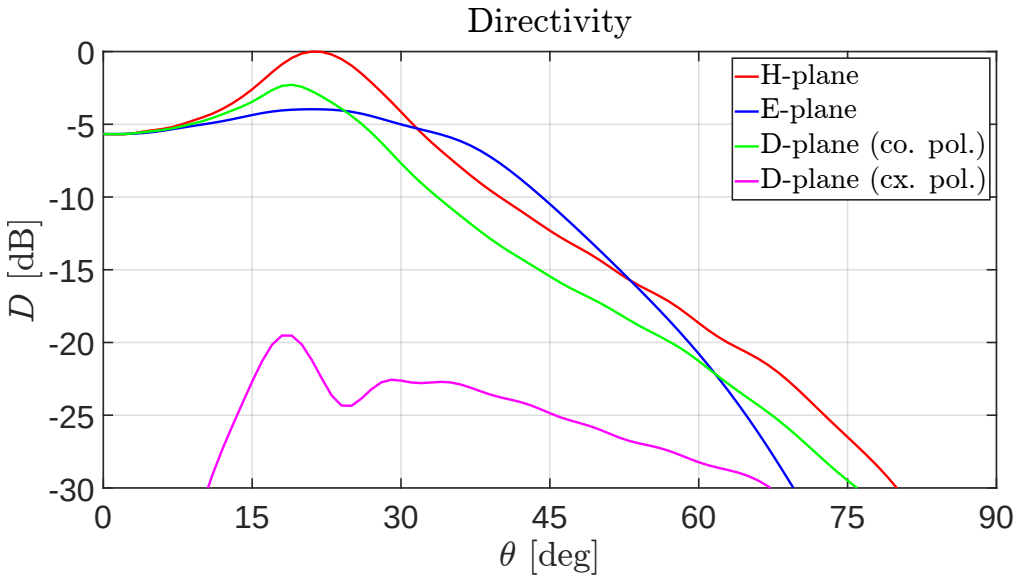

Figure 4.6: Directivity of the LWA with three slots: $\varepsilon_r = 11.9, h = w_s = 0.02\lambda_{0c}, \alpha_r = 30°$

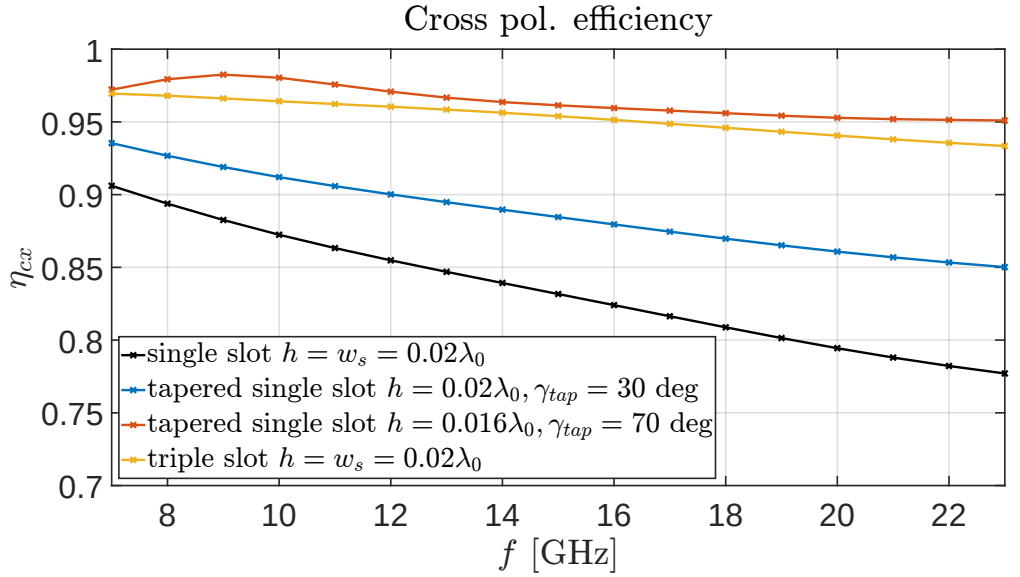

Figure 4.7: Cross pol. efficiency: non-tapered single slot vs. tapered single slot vs. triple slot

In Figure 4.6, the directivity of the LWA with three slots is presented. Even though the air-cavity thickness of this antenna is the same as the air-cavity thickness of one of the tapered slot antennas presented in the previous section, it is evident that the cross pol. component in D-plane is significantly lower: around -20dB. This effect can be further quantified by calculating cross pol. efficiency (Figure 4.7). Notably, the efficiency of the triple slot antenna is much higher than that of the tapered slot with the same height h and $\gamma_{tap} = 30°$, and slightly smaller than the efficiency of the other tapered slot case presented.[3]

[3]Based on the directivity plots presented in the previous section, it is intuitive to assume that the cross pol. efficiency of the triple slot antenna would be better than the efficiencies of both tapered slot cases presented

Based on the results presented in this section, it can be concluded that the LWA with three slots gives an additional degree of freedom that can be used to control the leaky wave contributions so as to achieve very low cross pol. In the next subsection, the potential of the leaky wave antenna with three slots as a feed to a leaky lens is analysed.

4.2.1 LWA with three slots as a feed to a lens

The antennas analysed so far are usually used as a feed to a lens in order to achieve directive radiation patterns across a wide frequency band. For that reason, performances of the lens antenna with different feeds (non-tapered single slot, tapered single slot, triple slot) are presented in this subsection.

In Figure 4.8, the geometry of an elliptical lens antenna is illustrated. Diameter of the lens is fixed to $D = 10\lambda_{0c}$. Truncation angle is noted as θ_0, while the relative permitivity of the matching layer is $\varepsilon_{r,m} = \sqrt{\varepsilon_r}$.

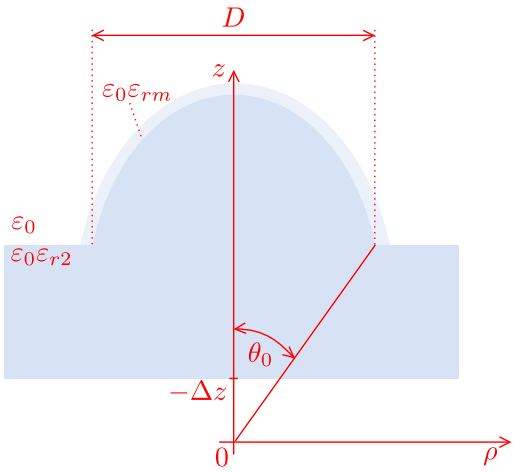

Figure 4.8: Leaky lens antenna

As a measure of the performance of such antennas, aperture efficiency in reception is used. This efficiency is defined as:

$$\eta_{ap} = \eta_{f2b}\frac{P_{load}}{P_{inc}} = \eta_{f2b}\frac{R_{GO}^2\left|\int_0^{2\pi}\int_0^{\theta_0}\vec{E}_{GO}(\theta,\phi)\cdot\vec{E}_{FF}(\theta,\phi)\sin\theta d\theta d\phi\right|^2}{2\zeta_2\int_0^{2\pi}\int_0^{\frac{\pi}{2}}|\vec{E}_{FF}(\theta,\phi)|^2\sin\theta d\theta d\phi}\frac{1}{P_{inc}}, \tag{4.2}$$

where $\vec{E}_{GO}$ represents the incoming field on GO sphere of radius R_{GO}, $\vec{E}_{FF}$ the far field of the feed, η_{f2b} front-to-back efficiency of the feed and P_{inc} the power incident on the lens surface by a plane wave. Characteristic impedance is given as $\zeta_2 = \frac{120\pi}{\sqrt{\varepsilon_r}}$. [13]

The aperture efficiencies for different feeds of the leaky wave lens antenna are plotted in Figure 4.9. This was done by keeping the diameter of the lens fixed and optimising the truncation angle and the phase center of the feed so as to obtain the highest aperture efficiency at the central frequency. It can be noted that the lens antenna with the triple slot outperforms the tapered slot of the same air-cavity thickness. Comparing the aperture efficiency of the triple slot fed antenna to the one with the tapered slot of $\gamma_{tap} = 70°$ and $h = 0.016\lambda_{0c}$, the tapered

(−20dB cross pol. level in D-plane compared to −10dB and −14dB). However, the cross pol. does not only exist in D-plane and its maximum might be elsewhere. This is something that is accounted for in the cross pol. efficiency.

slot is slightly better, which can be attributed to the smaller air-cavity and very large tapering angle. However, its truncation angle is larger, which would contribute to more complicated manufacturing of the matching layer.

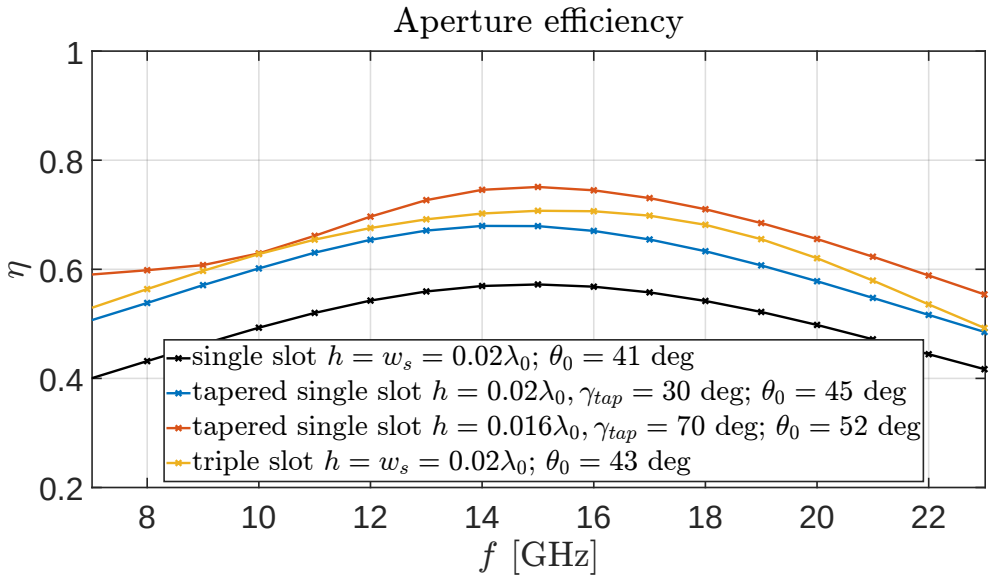

Figure 4.9: Aperture efficiency: non-tapered vs. tapered slot vs. triple slot

Furthermore, in Figure 4.10 the amplitude of the S_{11}-parameter is plotted for the analysed feeds showing that the triple slot antenna has a good matching across the observed $3:1$ frequency band. Additionally, the input impedance of the triple slot antenna is the highest of all feeds which could be beneficial for the application of time domain imaging using photoconductive antennas, for example.

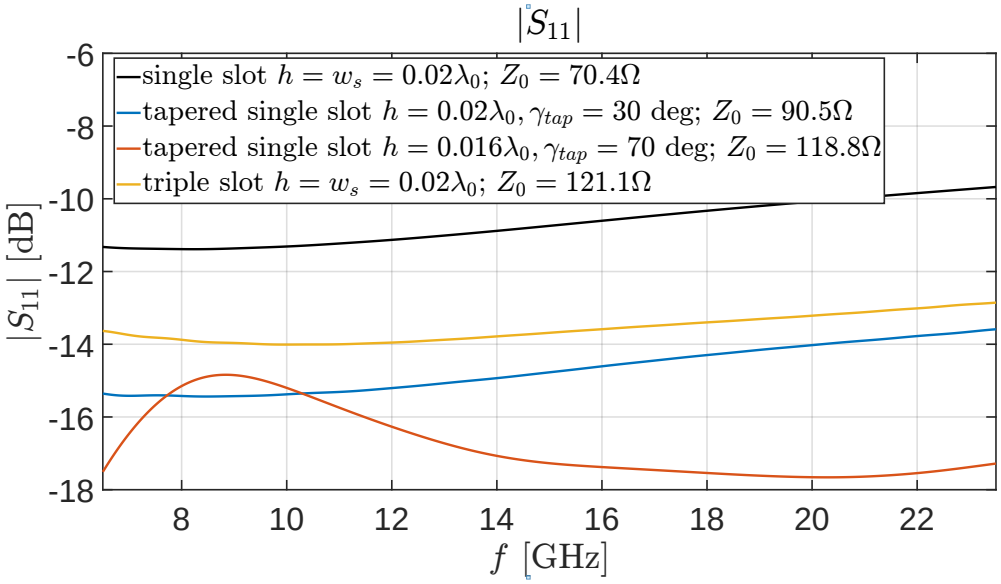

Figure 4.10: $|S_{11}|$: non-tapered vs. tapered slot vs. triple slot

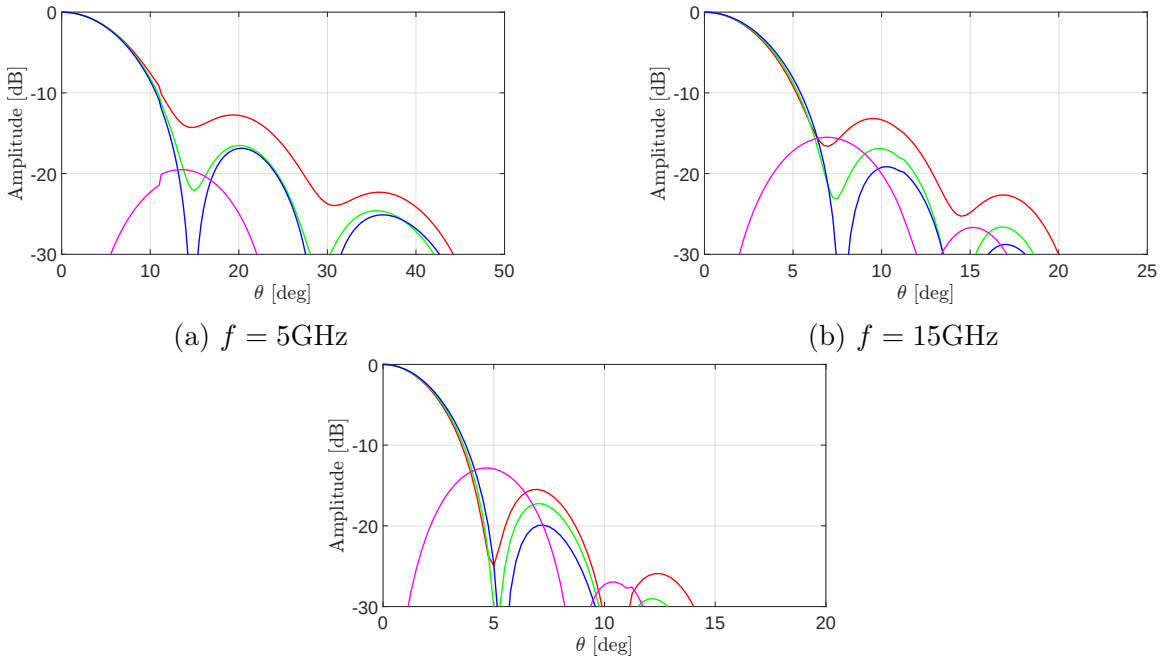

(a) $f = 5$GHz (b) $f = 15$GHz

(c) $f = 23$GHz

Figure 4.11: Secondary radiation patterns of the leaky lens fed by the tapered single slot: $\varepsilon_r = 11.9$, $h = 0.02\lambda_{0c}$, $\gamma_{tap} = 30°$ (red: H-plane, blue: E-plane, green: D-plane, magenta: D-plane cx.)

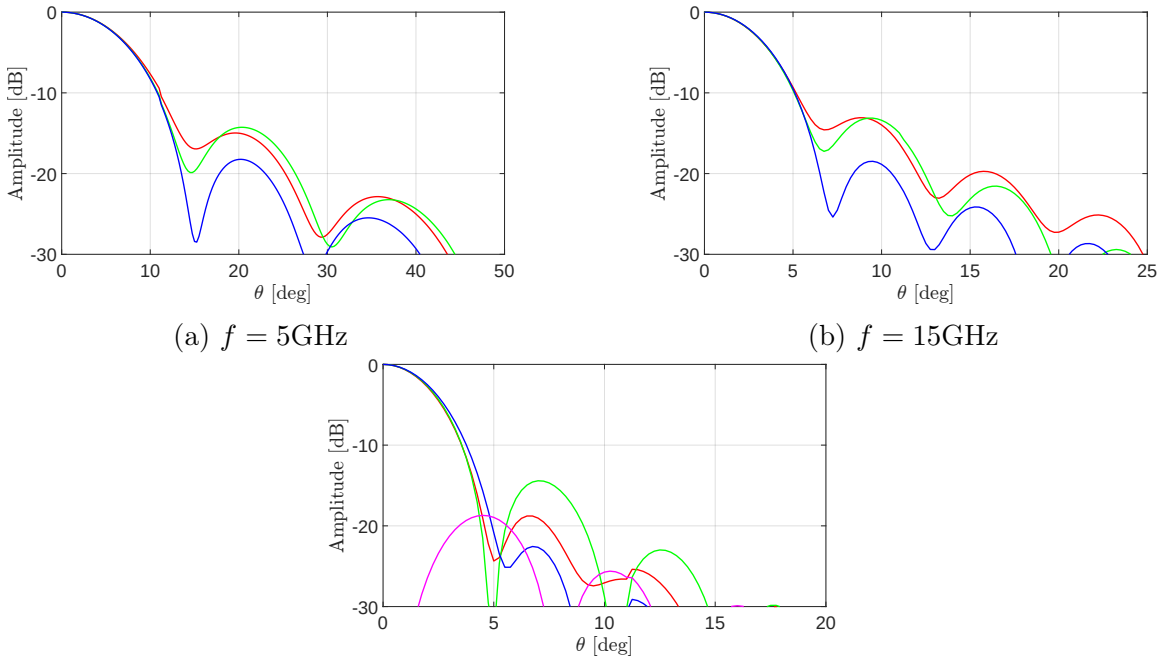

(a) $f = 5$GHz (b) $f = 15$GHz

(c) $f = 23$GHz

Figure 4.12: Secondary radiation patterns of the leaky lens fed by the LWA with three slots: $\varepsilon_r = 11.9$, $h = w_s = 0.02\lambda_{0c}$ (red: H-plane, blue: E-plane, green: D-plane, magenta: D-plane cx.)

Finally, in Figures 4.11 and 4.12, the secondary radiation patterns of the leaky lens antenna fed by a single tapered slot and LWA with three slots of the same air-cavity thickness are presented, respectively.[4] Comparing these results at three frequency points $f = 7, 15, 23$ GHz, it can be

[4]The secondary radiation patterns were obtained using Geometrical Optics / Fourier Optics Tool for Ana-

noted that the cross pol. in D-plane is significantly better for the antenna with three slots.

4.3 Parametric analysis of the LWA with multiple slots

In the previous section, the potential of the leaky wave antenna with multiple slots was demonstrated. In the upcoming subsections, parametric analysis of the antenna is presented and the results obtained are discussed. The dependence on the following parameters is discussed: angle α_r, the number of slots, the air cavity thickness h and the slot taper.

4.3.1 Angle α_r

A new parameter that is introduced with the LWA with multiple slots is the angle α_r. In this subsection, the dependence of the feed's far field and the aperture efficiency of the consequent leaky lens are analysed.

In Figure 4.13, the directivity of the leaky wave antenna with three slots is presented for different angles α_r ranging from 15° to 45°. Firstly, it can be noted that as α_r gets larger, the radiation pattern in E-planes gets more directive. Similarly, the direction of radiation in D-plane is slowly shifted to smaller angles of θ. This could be explained by the fact that with introducing the two additional slots, the field in E and D-planes get their dominant contribution from the slot modes of these two slots. Even though the modes excited in the three slots are not analysed in detail in this report due to complexity of solving that problem, for the sake of simplicity and the first-level explanation, it is imagined that the slot mode is excited in all three slots. Following that logic, a rough illustration for $\alpha_r = 45°$: contribution in D-plane is expected to be similar to the contribution in H-plane for the single slot antenna, while the pattern in E-plane would be more similar to the pattern in D-plane of the antenna with one slot.

Another thing that can be read from the graphs presented in Figure 4.13 is that at first the cross pol. component in D-plane gets lower with increasing α_r and after reaching the minimum value for $\alpha_r \approx 30°$, the cross pol. increases again.

The aperture efficiencies of the leaky lens fed by three-slot LWAs with different α_r are presented in Figure 4.14. It can be seen that the highest aperture efficiency is obtained with $\alpha_r = 30°$.

lyzing Quasi-optical Components (GO/FO) for which the interface is presented in [14].

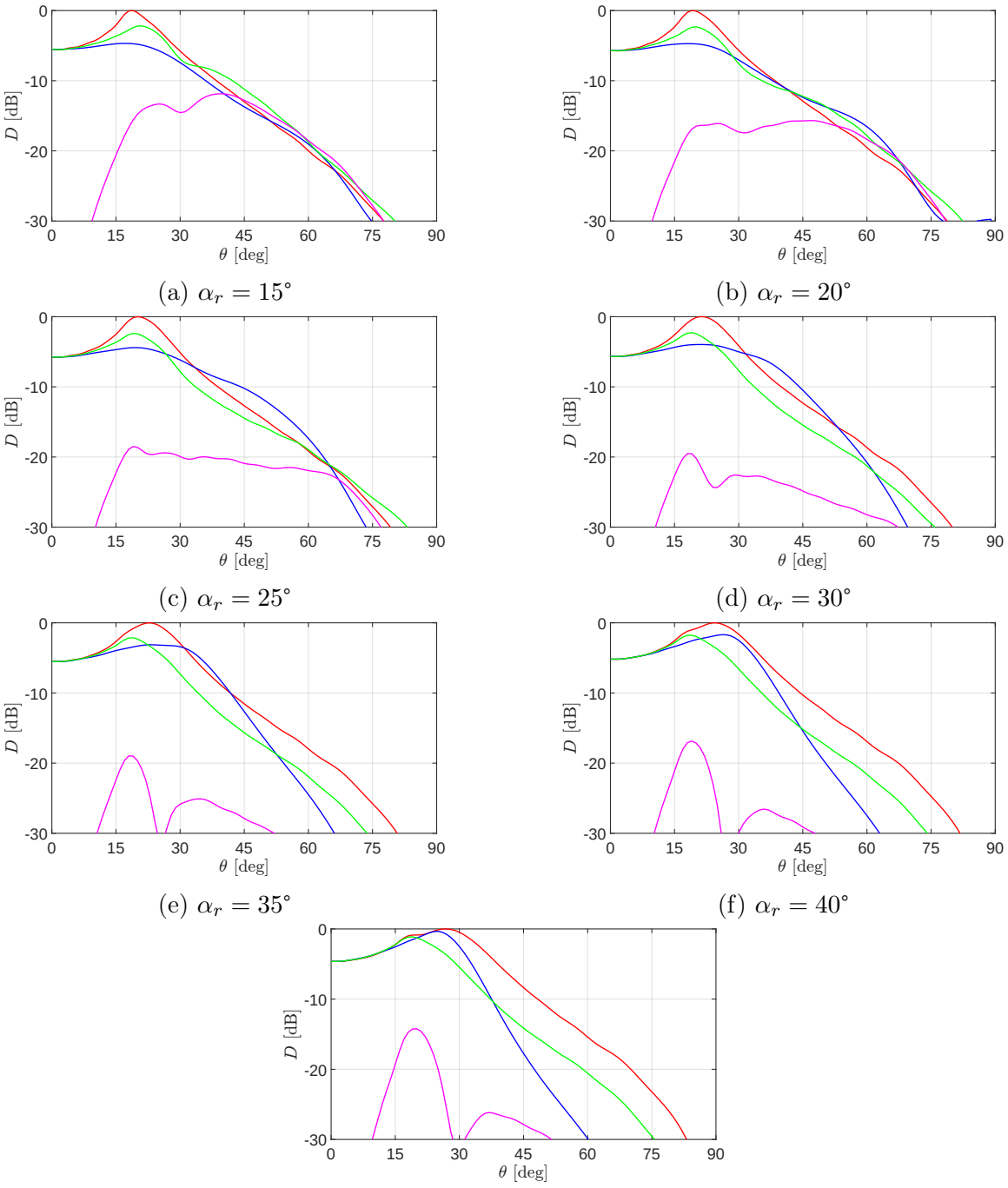

(a) $\alpha_r = 15°$ (b) $\alpha_r = 20°$

(c) $\alpha_r = 25°$ (d) $\alpha_r = 30°$

(e) $\alpha_r = 35°$ (f) $\alpha_r = 40°$

(g) $\alpha_r = 45°$

Figure 4.13: Directivity of the LWA with three slots: $\varepsilon_r = 11.9, h = w_s = 0.02\lambda_{0c}$ (red: H-plane, blue: E-plane, green: D-plane, magenta: D-plane cx.)

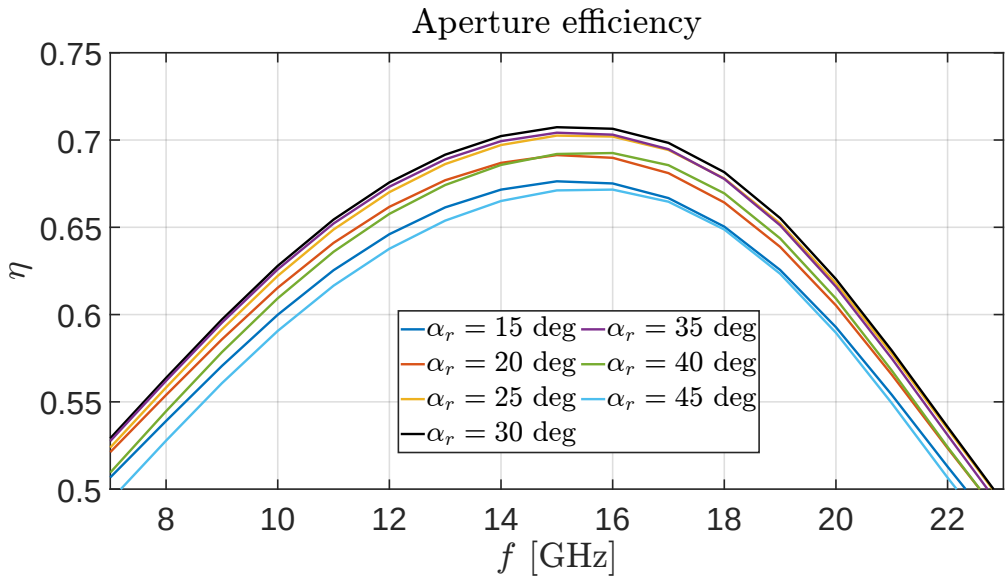

Figure 4.14: Aperture efficiency: $\varepsilon_r = 11.9, D = 10\lambda_{0c}, h = w_s = 0.02\lambda_{0c}$

4.3.2 Number of slots

Thus far, the analysed leaky wave antenna consisted of three slots. In this subsection, the antenna with two slots is presented (Figure 4.15). This is done with anticipating the tapering of the slots presented later in Subsection 4.3.4 since the double slot antenna offers opportunity for larger angle of tapering than the LWA with three slots.

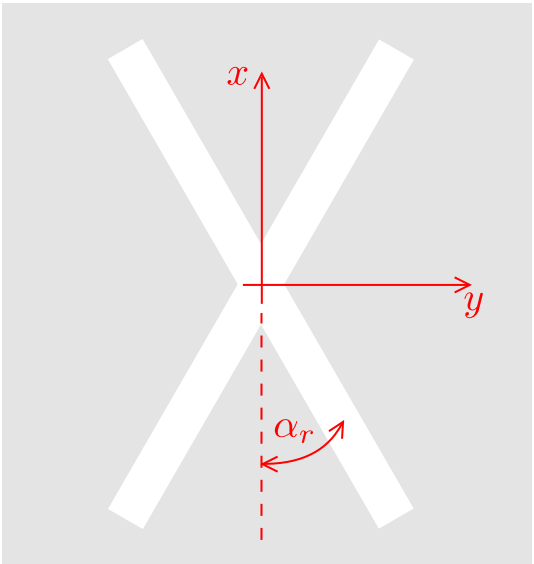

Figure 4.15: LWA with two slots

For the sake of having contributions of the slot modes in D and H-planes as similar as possible, α_r as defined in Figure 4.15 is taken to be 22.5°. The far field of the LWA with two slots for $h = w_s = 0.02\lambda_{0c}$ is plotted in Figure 4.16a, while the directivity of the antenna with three slots for the same h and w_s and $\alpha_r = 30°$ is presented again in Figure 4.16b. It can be noted that the antenna with two slots is slightly more directive and has larger cross pol. than the antenna with three slots. Furthermore, in the E-plane of the double slot antenna, due to the smaller angle α_r there is radiation pointing in the direction of $\theta \approx 60°$.

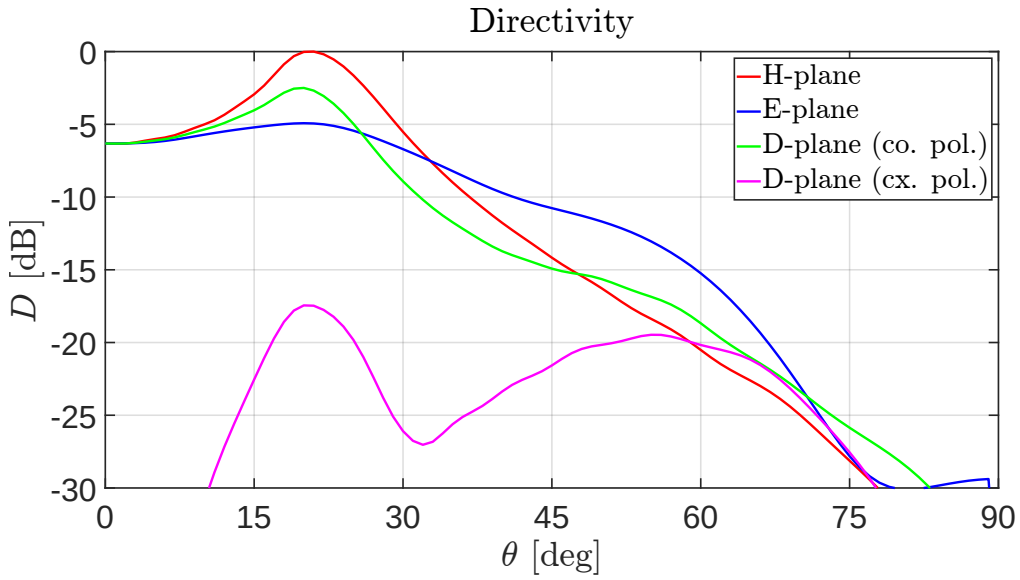

(a) 2 slots $\alpha_r = 22.5°$

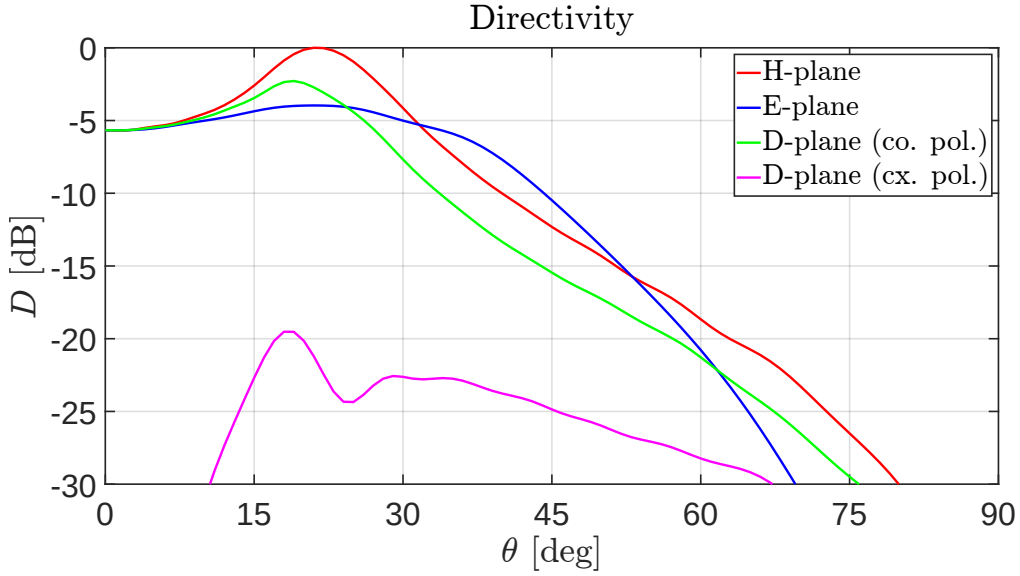

(b) 3 slots $\alpha_r = 30°$

Figure 4.16: Directivity of the LWA with multiple slots $\varepsilon_r = 11.9, h = w_s = 0.02\lambda_{0c}$

The aperture efficiencies of the LWA with two and three slots are presented in Figure 4.17. It can be noted that the leaky lens fed with antenna with three slots performs slightly better than the antenna with two slots. However, the truncation angle of the LWA with two slots is slightly smaller than that of a LWA with three slots.

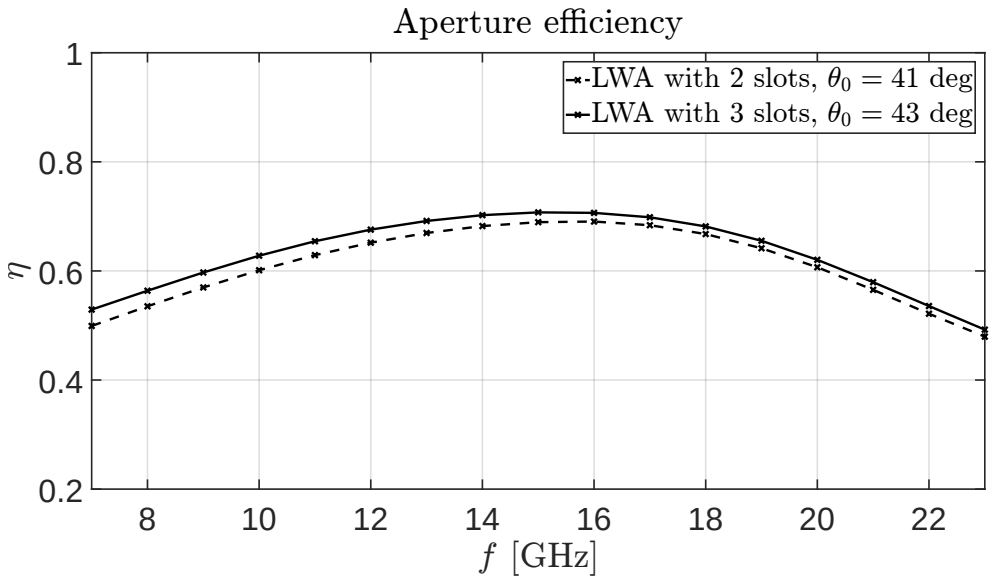

Figure 4.17: Aperture efficiency: LWA with two slots $\alpha_r = 22.5°$ vs. LWA with three slots $\alpha_r = 30°$: $\varepsilon_r = 11.9, D = 10\lambda_{0c}, h = w_s = 0.02\lambda_{0c}$

4.3.3 Air-cavity thickness

As was discussed in Section 4.1, in order to achieve lower cross pol. of the feed and better aperture efficiency of the leaky lens, the air-cavity thickness can be decreased. In this subsection, the results for the leaky wave antenna with three slots are presented for the air-cavity thickness of $h = 0.016\lambda_{0c}$.

The far field of the LWA with three slots and $h = w_s = 0.016\lambda_{0c}$ is plotted in Figure 4.18, while the aperture efficiency of the leaky lens fed by it is presented in Figure 4.19. As can be noted, the aperture efficiency is increased with thinner air-cavity, but the truncation angle of the lens is also increased which can be a downside for the manufacturing of certain types of matching layers.

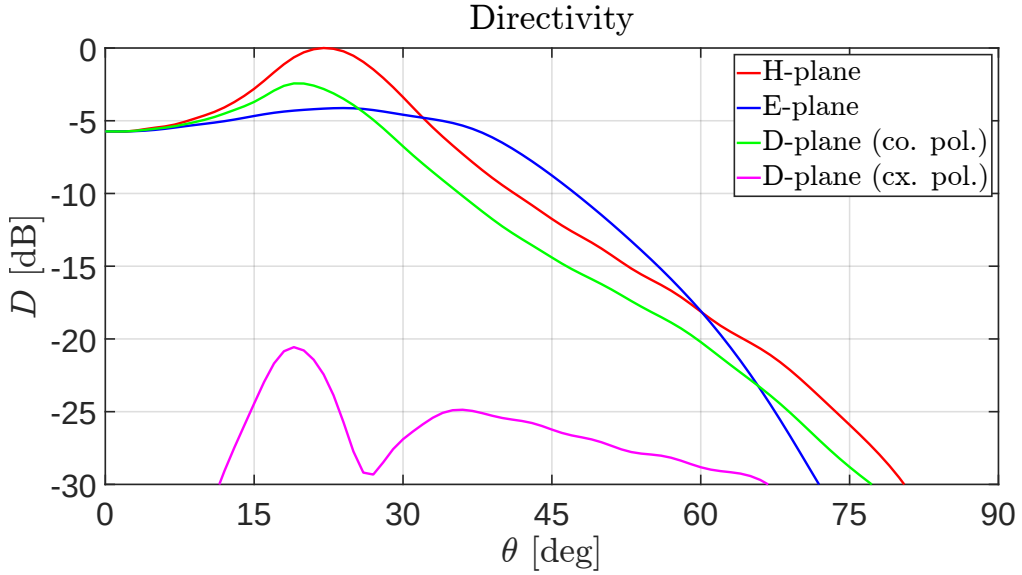

Figure 4.18: Directivity of the LWA with three slots: $\varepsilon_r = 11.9, h = w_s = 0.016\lambda_{0c}$

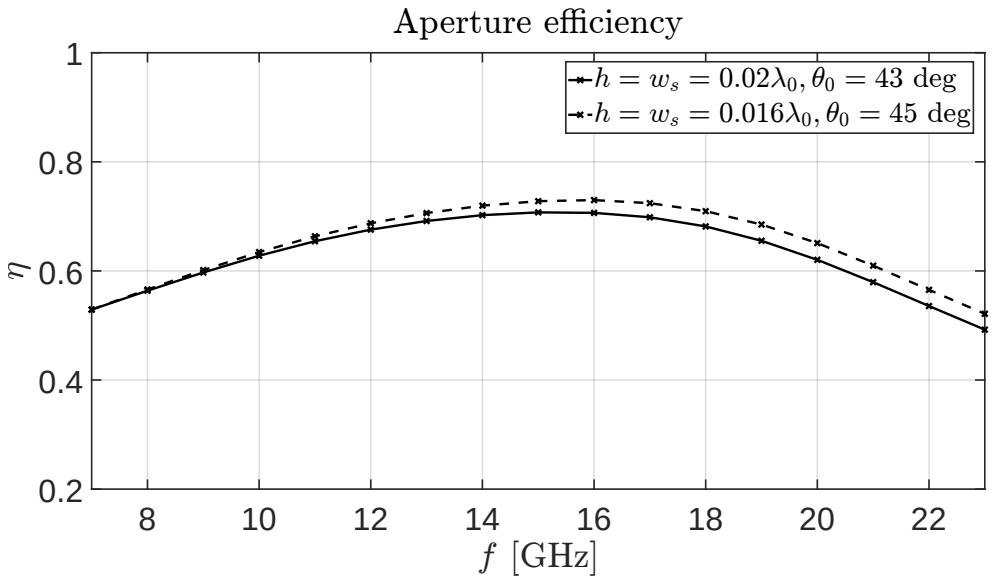

Figure 4.19: Aperture efficiency: LWA with three slots: $\varepsilon_r = 11.9, h = w_s = 0.016\lambda_{0c}$ vs. $h = w_s = 0.02\lambda_{0c}$

4.3.4 Slot tapering

Finally, in this subsection the tapering of the slots is explored. The analysed case is the leaky wave antenna with two slots $h = w_s = 0.016\lambda_{0c}, \alpha_r = 22.5°$ and $\gamma_{tap} = 20°$ (Figure 4.20).

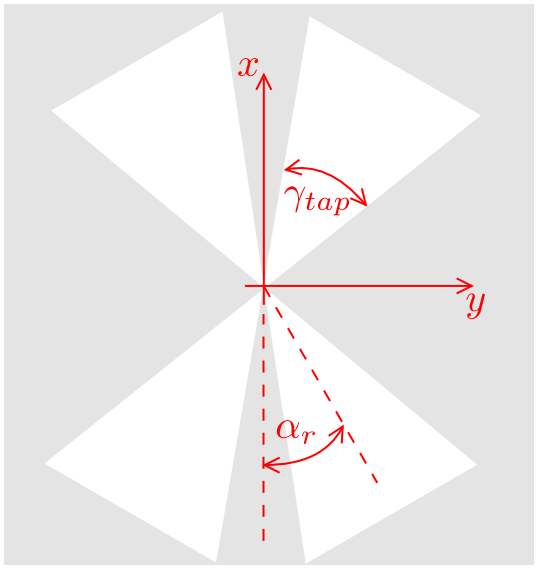

Figure 4.20: LWA with two tapered slots

From the far field presented in Figure 4.21, it can be noted that the cross pol. is further decreased compared to all the other cases analysed so far. Furthermore, the radiation at larger angles of θ is decreased, and the pattern is more symmetric. However, as discussed in Section 4.1, the leaky wave contribution decreases leading to a less directive pattern.

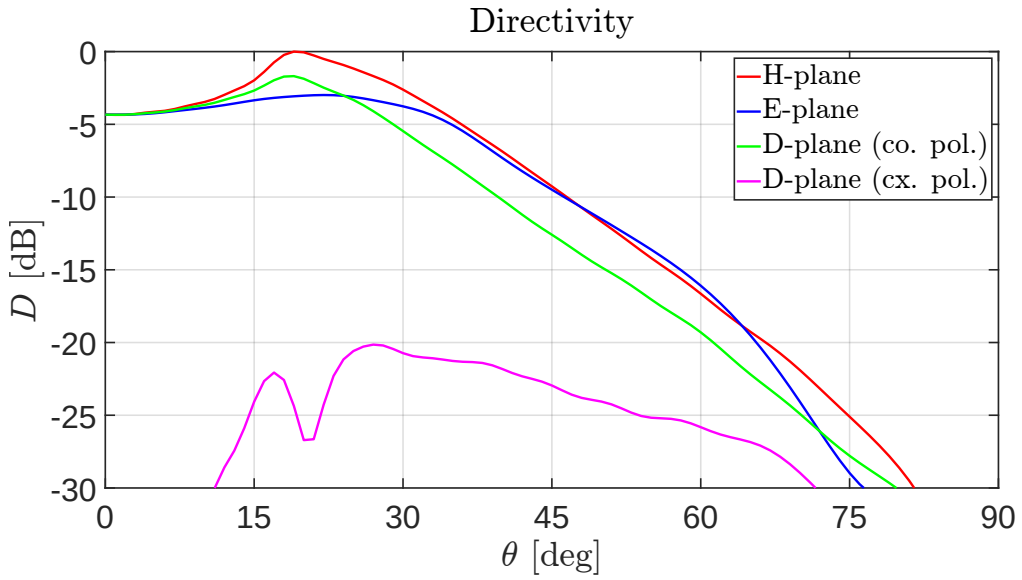

Figure 4.21: Directivity of the LWA with two tapered slots:
$\varepsilon_r = 11.9, h = w_s = 0.016\lambda_{0c}, \alpha_r = 22.5°, \gamma_{tap} = 20°$

The aperture efficiency of the lens antenna fed by the LWA with two tapered slots is plotted in Figure 4.22 and compared to the aperture efficiencies of the cases previously analysed. It can be noted that the LWA with two tapered slots outperforms the tapered single slot antenna from [3] in terms of the aperture efficiency. Furthermore, the truncation angle is decreased from 52° and 48°. However, this decrease is not large enough to help with the manufacturing of the matching layer significantly. In order to understand what aspect of the antenna could be further improved, different efficiencies are analysed.

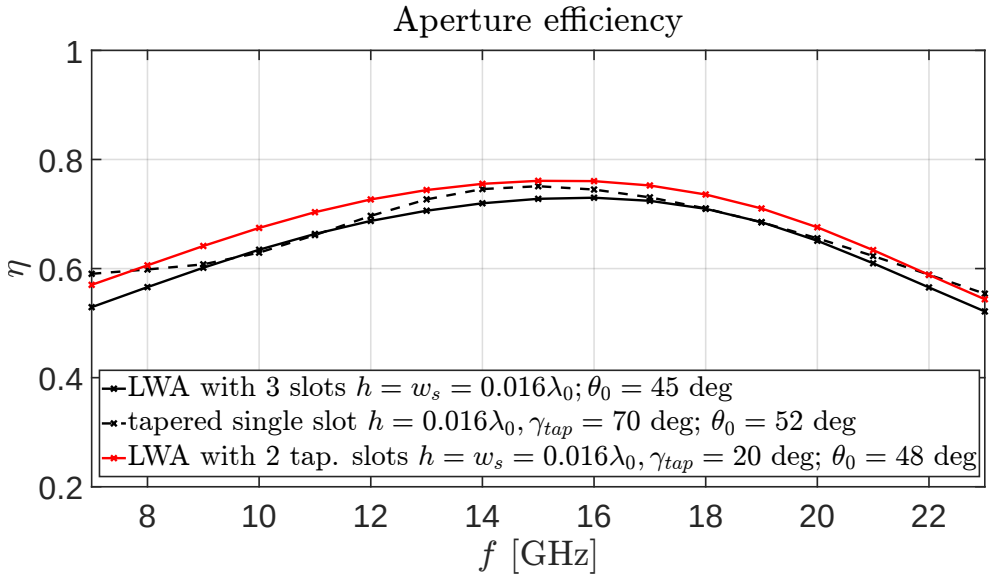

Figure 4.22: Aperture efficiency: LWA with two tapered slots
$\varepsilon_r = 11.9, h = w_s = 0.016\lambda_{0c}, \alpha_r = 22.5°, \gamma_{tap} = 20°$ vs. previous cases

In Figure 4.23, different efficiencies are plotted [15]. As can be noted, the most problematic aspect is the spillover. This is a direct consequence of decreasing the directivity by weakening the leaky waves through decreasing the thickness of the air-cavity and tapering the slots. However, if the taper and small air-cavity are not employed, spillover efficiency increases but the radiation pattern loses in symmetry and consequently the amplitude and aperture efficiency.

Therefore, the solution is not to simply increase h and use smaller taper, but the air-cavity of non-uniform thickness would likely need to be used.

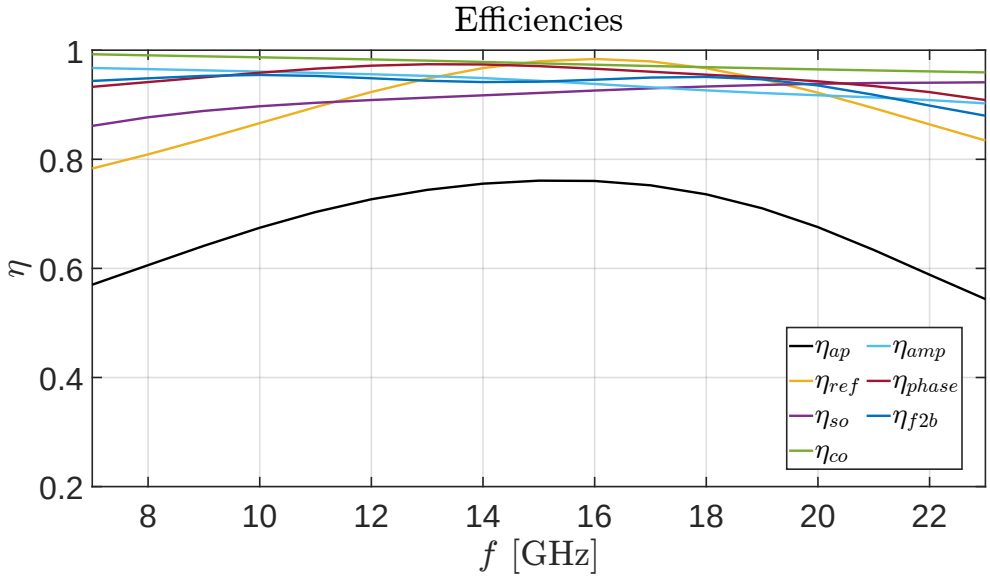

Figure 4.23: Efficiencies of the LWA with two tapered slots:
$\varepsilon_r = 11.9, h = w_s = 0.016\lambda_{0c}, \alpha_r = 22.5°, \gamma_{tap} = 20°$

To conclude, for the same thickness of the air-cavity, the leaky lens antenna fed by the LWA with multiple non-tapered slots achieves better aperture efficiency than having a single tapered slot as the feed due to the better performance in terms of the cross pol. (Figure 4.9). Additionally, the lens truncation angle is reduced allowing easier manufacturing of the matching layer. On the other hand, if higher aperture efficiency is needed while maintaining the small truncation angle of the lens, non-uniform air-cavity might be the solution.

Chapter 5

Conclusions and future work

5.1 Summary and conclusions

In this report, the analysis of the infinite slot leaky wave antenna was presented and a new geometry for the feed of a leaky lens was explored.

Firstly, the TM_0 mode and its propagation constant were presented (Chapter 2). Next, the slot mode was analysed. Observing the behaviour of the slot pole, it was not clear in which Riemann sheet with respect to k_0 the pole was to be found. For that reason, the integration paths in k_y-plane were defined and magnetic current was calculated as a summation of different contributions (space wave and leaky waves). Comparing this magnetic current with the total magnetic current obtained via the integration path that stays on top Riemann sheets for both branch-cuts, it was concluded that the slot pole is found in the top Riemann sheet for k_0 and the bottom Riemann sheet for k_2. Furthermore, it was noted that as the air-cavity and the width of the slot grow larger, the slot mode becomes less dominant and the contribution of the space wave increases. Next, the approximated contributions of the leaky waves were shown and the high level of cross pol. was noted and linked to the observation that the TM_0 and slot modes are intrinsically different in their natures and dependency on ϕ.

In order to gain deeper understanding of the leaky waves' behaviour, the spectral analysis of the near field was performed and presented in Chapter 3. Firstly, the closing of the integral in α was shown together with the approximation on the magnetic current that allows for an analytical solution of the integration in α. This was done in order to avoid the numerical method of closing this integral which would require a lot of computational time. Secondly, the singularities in k_ρ-plane were noted so as to understand how the integration should be performed. The integration paths in different planes were presented next together with the results of the electric field obtained with this approach. Finally, the electric field results were verified with the total electric field calculated when the integration path does not cross any branch-cuts demonstrating that the complex analysis presented in this chapter is valid. The comparison with the results obtained with full wave CST simulation does not result in the perfect match, but this outcome was expected due to the rough approximation made on the magnetic current and does not take away the gained insight into the behaviours of the modes.

Finally, in Chapter 4 a new geometry: leaky wave antenna with multiple slots was explored and compared to the state of the art leaky lens feed (tapered slot). As an example of the LWA with multiple slots, antenna with three slots was illustrated and its performance in terms of the cross pol. efficiency and aperture efficiency of the leaky lens that uses it as the feed was put forward. It is concluded that for the same air-cavity thickness, the LWA with three slots outperforms

the tapered slot in terms of cross pol. efficiency and, consequently, in aperture efficiency. Furthermore, the lens truncation angle is decreased which can be beneficial in manufacturing of the matching layer. Next, the parametric analysis of the new feed geometry was presented with analysing the angle α_r, the number of slots, air-cavity thickness and the tapering of the slots. It was seen that the aperture efficiency can be increased further by reducing the air-cavity thickness and tapering the slots, but with the consequent increase of the truncation angle as well.

5.2 Future work

As was concluded in the previous chapter, in order to achieve higher aperture efficiency without increasing the lens truncation angle, additional degree of freedom is likely needed. A possible solution through which this new degree of freedom might be gained is the non-uniform air-cavity. In this section, the introduction to the analysis of the tapered air-cavity is presented.

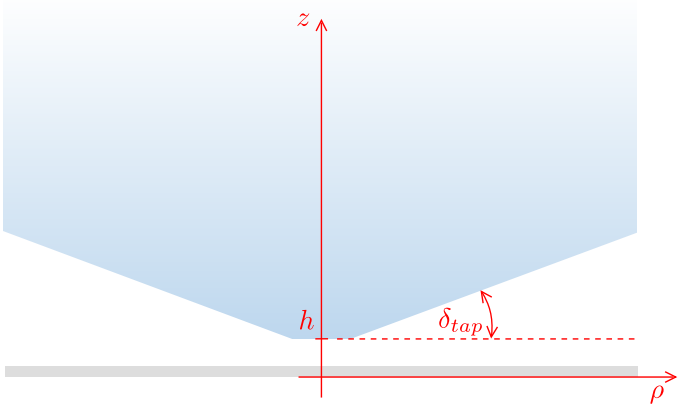

Figure 5.1: Uniformly tapered air-cavity

In Figure 5.1, the geometry of the antenna with the uniformly[1] tapered air-cavity is illustrated. As can be noted, the angle that defines the taper is δ_{tap}. The far field results obtained for different air-cavity tapering angles of the infinite slot LWA are plotted in Figure 5.2. It is evident that the pointing angle in the main plains decreases as the tapering angle increases. Furthermore, the field gets more directive. This was to be expected due to the fact that the air-cavity becomes thicker with the tapering. It can also be noted that the cross pol. grows with bigger tapering angle δ_{tap}.

Observing the far field in main planes of the infinite slot leaky wave antenna (Figure 4.1) and their asymmetry, it can be concluded that in order to achieve a more symmetrical pattern, the radiation in E-plane needs to be more directive. Ideally, the pattern in H-plane would be slightly less directive in order to have similar pattern as the one desired in E-plane. However, based on the results presented in Figure 5.2, with tapering the air-cavity, the directivity increases in all planes. For that reason, this geometry would not lead to a more symmetrical pattern.

[1]Uniformly meaning that the tapering angle is the same for every plane.

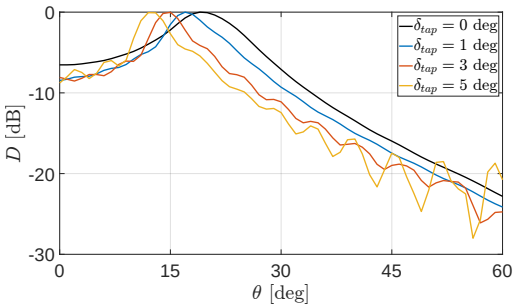

(a) H-plane

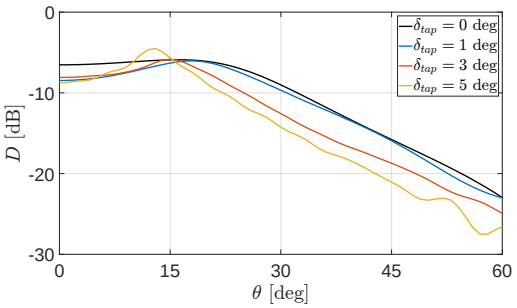

(b) E-plane

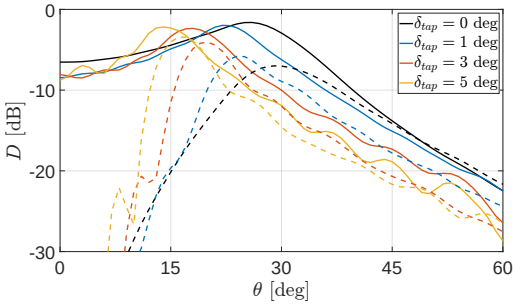

(c) D-plane (solid: co. pol, dashed: cx. pol)

Figure 5.2: Directivity of the infinite slot LWA with uniformly tapered air-cavity: $\varepsilon_r = 11.9, h = w_s = 0.02\lambda_0, \delta_{tap} = [0, 1, 3, 5]^\circ$

However, a potential solution to this problem might be to apply the tapered air-cavity in certain sectors and to have it uniform in others. More precisely, if it is assumed that the far field in H-plane is dominantly dependent on the air-cavity around the slot and the field in E-plane on the air-cavity in the plane perpendicular to the slot, the air-cavity thickness could be designed in the manner presented in Figure 5.3. With this, the goal is to have H-plane remain the same while making the pattern in E-plane more directive. Additionally, in order to decrease the cross pol. levels presented in Figure 5.2c, LWA with multiple slots can be used. Furthermore, if the H-plane needs to be less directive, small taper of the slots can be employed.

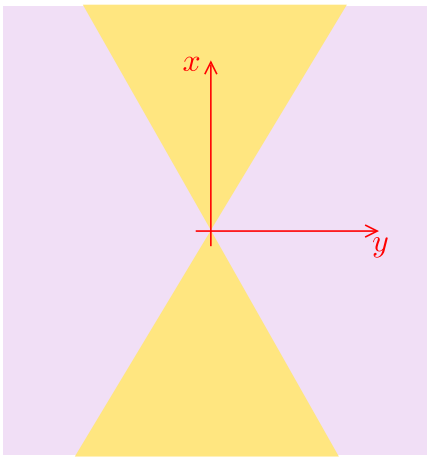

Figure 5.3: Air-cavity tapered in sectors (yellow: uniform air-cavity, purple: tapered air-cavity)

The presented ideas are yet to be further explored. The analysis of these designs and their implementation are expected to be the continuation of the work presented within this report.

Bibliography

[1] A. Neto. UWB, Non Dispersive Radiation From the Planarly Fed Leaky Lens Antenna—Part 1: Theory and Design. *IEEE Transactions on Antennas and Propagation*, 58(7):2238–2247, 2010.

[2] O. Yurduseven. *Wideband integrated lens antennas for Terahertz deep space investigation*. PhD thesis, Delft University of Technology, 2016.

[3] S.O. Dabironezare. *Fourier Optics Field Representations for the Design of Wide Field-of-View Imagers at Sub-millimetre Wavelengths*. PhD thesis, Delft University of Technology, 2020.

[4] J. Bueno, S. Bosma, T. Bußkamp-Alda, M. Alonso-delPino, and N. Llombart. Lossless Matching Layer for Silicon Lens Arrays at 500 GHz Using Laser Ablated Structures. *Transactions on Terahertz Science and Technology (under review)*, 2022.

[5] S. van Berkel. Characterization of Printed Transmission Lines at High Frequencies. Using quasi-analytical expressions. Master's thesis, Delft University of Technology, 2015.

[6] A. Neto and N. Llombart. Wideband Localization of the Dominant Leaky Wave Poles in Dielectric Covered Antennas. *IEEE Antennas and Wireless Propagation Letters*, 5:549–551, 2006.

[7] A. Neto, N. Llombart, and D. Cavallo. Lecture notes for Spectral Domain Methods in Electromagnetics. *Delft University of Technology*, 2021.

[8] A. Neto and S. Maci. Green's function for an infinite slot printed between two homogeneous dielectrics. i. magnetic currents. *IEEE Transactions on Antennas and Propagation*, 51(7):1572–1581, 2003.

[9] F. Mesa, C. di Nallo, and D.R. Jackson. The theory of surface-wave and space-wave leaky-mode excitation on microstrip lines. *IEEE Transactions on Microwave Theory and Techniques*, 47(2):207–215, 1999.

[10] A. Neto, N. Llombart, G. Gerini, Magnus D. Bonnedal, and P. de Maagt. EBG Enhanced Feeds for the Improvement of the Aperture Efficiency of Reflector Antennas. *IEEE Transactions on Antennas and Propagation*, 55(8):2185–2193, 2007.

[11] J.W. Brown and R.V. Churchill. *Complex Variables and Applications*. Mc Graw Hill Education, 2014.

[12] S. Bosma, A. Neto, and N. Llombart. On the Near-Field Spherical Wave Formation in Resonant Leaky-Wave Antennas: Application to Small Lens Design. *IEEE Transactions on Antennas and Propagation*, 70(2):801–812, 2022.

[13] H. Zhang, S. O. Dabironezare, G. Carluccio, A. Neto, and N. Llombart. A Fourier Optics Tool to Derive the Plane Wave Spectrum of Quasi-Optical Systems [EM Programmer's Notebook]. *IEEE Antennas and Propagation Magazine*, 63(1):103–116, 2021.

[14] H. Zhang, S. O. Dabironezare, G. Carluccio, A. Neto, and N. Llombart. A GO/FO Tool for Analyzing Quasi-Optical Systems in Reception. In *2019 44th International Conference on Infrared, Millimeter, and Terahertz Waves (IRMMW-THz)*, pages 1–2, 2019.

[15] A. Neto, N. Llombart, and D. Cavallo. Lecture notes for Quasi Optical Systems. *Delft University of Technology*, 2021.

[16] A. Neto, N. Llombart, and D. Cavallo. Lecture notes for Spectral Domain Methods in Electromagnetics. *Delft University of Technology*, 2019.

Appendix A

Closing the integral in α analytically

In this appendix, the steps of closing the integral in α are put forward [16]. The expression for the electric field after making the approximation on α of the magnetic current is:

$$\vec{E}(\vec{r}) \approx \frac{1}{4\pi^2}\int_0^{\infty} M_x(k_\rho,\phi)\Big(\int_0^{2\pi} \tilde{G}^{EM}(k_\rho,\alpha,z)\mathrm{e}^{-jk_\rho\rho\cos(\alpha-\phi)}d\alpha\Big)k_\rho dk_\rho. \tag{A.1}$$

Separating components of the electric field:

$$E_{x/y/z}(\vec{r}) \approx \frac{1}{4\pi^2}\int_0^{\infty} M_x(k_\rho,\phi)\Big(\int_0^{2\pi} G^{EM}_{x/y/zx}(k_\rho,\alpha,z)\mathrm{e}^{-jk_\rho\rho\cos(\alpha-\phi)}d\alpha\Big)k_\rho dk_\rho. \tag{A.2}$$

Taking $k_x = k_\rho\cos\alpha, k_y = k_\rho\sin\alpha$, components of the spectral Green's function are given as:

$$G^{EM}_{xx}(k_\rho,\alpha,z) = \frac{(v_{TM}-v_{TE})k_xk_y}{k_\rho^2} = \frac{1}{2}(v_{TM}-v_{TE})\sin 2\alpha, \tag{A.3}$$

$$G^{EM}_{yx}(k_\rho,\alpha,z) = \frac{v_{TE}k_x^2+v_{TM}k_y^2}{k_\rho^2} = \frac{1}{2}v_{TE}(1+\cos 2\alpha)+\frac{1}{2}v_{TM}(1-\cos 2\alpha), \tag{A.4}$$

$$G^{EM}_{zx}(k_\rho,\alpha,z) = -\zeta_2\frac{k_y i_{TM}}{k_2} = \frac{k_y v_{TM}}{k_{z2}}. \tag{A.5}$$

Using the following identity:

$$\int_0^{2\pi} \overset{\cos}{\underset{sin}{}}(n\alpha)\mathrm{e}^{-jk_\rho\rho\cos(\alpha-\phi)}d\alpha = j^{-n}2\pi\overset{\cos}{\underset{sin}{}}(n\phi)J_n(k_\rho\rho), \tag{A.6}$$

closed integral in α is equal to:

$$F_x(k_\rho,\rho,z) = [v_{TE}-v_{TM}]\pi\sin 2\phi J_2(k_\rho\rho), \tag{A.7}$$

$$F_y(k_\rho,\rho,z) = v_{TE}\pi[J_0(k_\rho\rho)-\cos 2\phi J_2(k_\rho\rho)]+v_{TM}\pi[J_0(k_\rho\rho)+\cos 2\phi J_2(k_\rho\rho)], \tag{A.8}$$

$$F_z(k_\rho,\rho,z) = \frac{k_\rho v_{TM}}{k_{z2}}j2\pi\sin\phi J_1(k_\rho\rho), \tag{A.9}$$

where $F_{x/y/z}(k_\rho,\rho,z) = \int_0^{2\pi} G^{EM}_{x/y/zx}(k_\rho,\alpha,z)\mathrm{e}^{-jk_\rho\rho\cos(\alpha-\phi)}d\alpha$ and $J_{0/1/2}(k_\rho\rho)$ are Bessel functions of zeroth, first and second order. The electric field expression is left with the integral in k_ρ:

$$E_{x/y/z}(\vec{r}) \approx \frac{1}{4\pi^2}\int_0^{\infty} M_x(k_\rho,\phi)F_{x/y/z}(k_\rho,\rho,z)k_\rho dk_\rho. \tag{A.10}$$

Using the identity that relates Bessel functions to Hankel functions:

$$\int_0^{\infty} C(k_\rho)J_n(k_\rho\rho)k_\rho dk_\rho = \frac{1}{2}\int_{-\infty}^{\infty} C(k_\rho)H_n^{(2)}(k_\rho\rho)k_\rho dk_\rho, \tag{A.11}$$

the final form of the electric field expression is:

$$\vec{E}(\vec{r}) \approx \frac{1}{8\pi}\int_{-\infty}^{\infty} \tilde{G}_{k_\rho}^{EM}(k_\rho,\rho,z)M_x(k_\rho,\phi)k_\rho dk_\rho, \tag{A.12}$$

where

$$G_{k_\rho,x}^{EM}(k_\rho,\rho,z) = \sin 2\phi[v_{TE}-v_{TM}]H_2^{(2)}(k_\rho\rho), \tag{A.13}$$

$$G_{k_\rho,y}^{EM}(k_\rho,\rho,z) = v_{TE}[H_0^{(2)}(k_\rho\rho)-\cos 2\phi H_2^{(2)}(k_\rho\rho)] + v_{TM}[H_0^{(2)}(k_\rho\rho)+\cos 2\phi H_2^{(2)}(k_\rho\rho)], \tag{A.14}$$

$$G_{k_\rho,z}^{EM}(k_\rho,\rho,z) = j2\sin\phi\frac{k_\rho v_{TM}}{k_{z2}}H_1^{(2)}(k_\rho\rho). \tag{A.15}$$

Using the standard transformation from cartesian to cylindrical vectors, the cylindrical components of $G_{k_\rho}^{EM}(k_\rho,\rho,z)$ are:

$$G_{k_\rho,\rho}^{EM}(k_\rho,\rho,z) = \sin\phi[v_{TE}(H_0^{(2)}(k_\rho\rho)+H_2^{(2)}(k_\rho\rho)) + v_{TM}(H_0^{(2)}(k_\rho\rho)-H_2^{(2)}(k_\rho\rho))], \tag{A.16}$$

$$G_{k_\rho,\phi}^{EM}(k_\rho,\rho,z) = \cos\phi[v_{TE}(H_0^{(2)}(k_\rho\rho)-H_2^{(2)}(k_\rho\rho)) + v_{TM}(H_0^{(2)}(k_\rho\rho)+H_2^{(2)}(k_\rho\rho))], \tag{A.17}$$

$$G_{k_\rho,z}^{EM}(k_\rho,\rho,z) = j2\sin\phi\frac{k_\rho v_{TM}}{k_{z2}}H_1^{(2)}(k_\rho\rho). \tag{A.18}$$

Appendix B

β-plane integration and choosing the Riemann sheets

The integration paths illustrated in Section 3.3 are in k_ρ-plane. However, the SDP is given in β-plane as:

$$k_\rho = k_2 \sin\beta. \tag{B.1}$$

The SDP is further defined with a change of variable $\beta \to \tau$, where $\tau \in [-\infty, \infty]$ and:

$$\beta_{SDP} = \theta + 2\arcsin\frac{\tau e^{j\frac{\pi}{4}}}{\sqrt{2}}. \tag{B.2}$$

As shown in Section 3.2, for an arbitrary angle ϕ, there are three branch-cuts the crossings of which need to be taken into account when integrating: k_2, $\frac{k_0}{\cos\phi}$ and $\frac{k_2}{\cos\phi}$.[1] In order to explain how these crossings are performed, the branch-cuts are analysed with respect to the functions they stem from: k_2 w.r.t. the spectral Green's function and $\frac{k_0}{\cos\phi}$ and $\frac{k_2}{\cos\phi}$ w.r.t. the magnetic current.

The branch-cuts for which $\tilde{G}^{EM}_{k_\rho}$ is calculated are given with the choice of k_{z0} and k_{z2}. Since k_0 is not a branch-point of the Green's function, k_{z0} can be simply computed as $k_{z0} = -j\sqrt{k_0^2 - k_\rho^2}$. However, the way k_{z2} is calculated depends on the location in β-plane. Amplitudes of the real and imaginary parts can be obtained from $k_\rho = k_2\cos\beta$, but the signs of the real and imaginary parts need to be defined for different regions in β-plane as given in [12].

The choice of $\frac{k_0}{\cos\phi}$ and $\frac{k_2}{\cos\phi}$ Riemann sheets is made the same way as described in Subsection 2.2.2.

[1] The branch-cut due to the TM_0 pole is not taken into consideration.

Appendix C

Residual contributions of the modes

Shadow boundary region is defined as the region in which there is no explicit contribution of the leaky wave modes (their contribution cannot be separated as a residual contribution). Above the shadow boundary angle θ_{SB} (Figure C.1), the pole of the leaky wave is captured. [7]

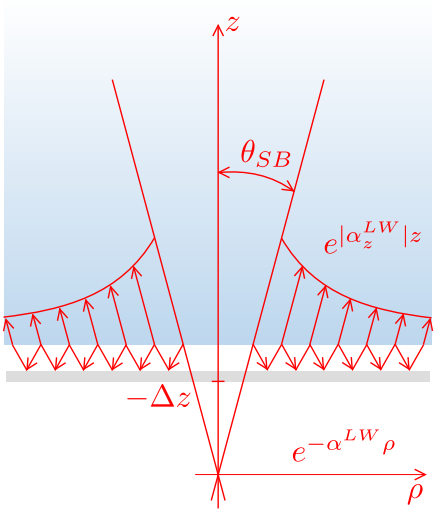

Figure C.1: Shadow boundary region

The shadow boundary angle of a leaky wave is calculated as:

$$\theta_{SB}^{LW} = \mathrm{Re}\{\beta^{LW}\} + \arccos\left(\mathrm{sech}(\mathrm{Im}\{\beta^{LW}\})\right), \tag{C.1}$$

where $\beta^{LW} = \arcsin\left(\frac{k_\rho^{LW}}{k_2}\right)$.

Applying the Cauchy's theorem (Eq.(3.11)), residual contribution of a leaky wave mode is calculated starting from Eq.(3.3) as:

$$\vec{E}_{LW}(\vec{r}) \approx -\frac{1}{8\pi} 2\pi j \mathrm{Res}[\tilde{G}_{k_\rho}^{EM}(k_\rho, \rho, z) M_x(k_\rho, \phi) k_\rho]\Big|_{k_\rho = k_{\rho,LW}}. \tag{C.2}$$

Substituting $\tilde{G}_{k_\rho}^{EM}(k_\rho, \rho, z)$ with Eq.(3.4), Eq.(3.5) and Eq.(3.6), the contribution of the TM_0

mode is:[1]

$$E_{TM_0,\rho}(\vec{r}) \approx -\frac{j}{4}\sin\phi\frac{N_{TM}[H_0^{(2)}-H_2^{(2)}]}{D'_{TM}}k_\rho M_x(k_\rho,\phi)\Big|_{k_\rho=k_\rho^{TM_0}}, \tag{C.3}$$

$$E_{TM_0,\phi}(\vec{r}) \approx -\frac{j}{4}\cos\phi\frac{N_{TM}[H_0^{(2)}+H_2^{(2)}]}{D'_{TM}}k_\rho M_x(k_\rho,\phi)\Big|_{k_\rho=k_\rho^{TM_0}}, \tag{C.4}$$

$$E_{TM_0,z}(\vec{r}) \approx -\frac{1}{2}\sin\phi\frac{k_\rho N_{TM}}{k_{z2}D'_{TM}}H_1^{(2)}k_\rho M_x(k_\rho,\phi)\Big|_{k_\rho=k_\rho^{TM_0}}, \tag{C.5}$$

where N_{TM} and D_{TM} are the numerator and the denominator of the voltage v_{TM}, respectively.

Similarly, the contribution of the slot mode can be calculated. However, since the pole of the slot mode is in k_x, the change of variables needs to be performed:

$$\int_C f(k_\rho)dk_\rho = 2\sum_{k=1}^{n}\mathrm{Res}_{k_\rho=k_{\rho,k}}f(k_\rho), \tag{C.6}$$

$$\int_C f\Big(\frac{k_x}{\cos\phi}\Big)\frac{1}{\cos\phi}dk_x = \frac{1}{\cos\phi}2\sum_{k=1}^{n}\mathrm{Res}_{k_x=k_{x,k}}f(k_x). \tag{C.7}$$

Residual contribution of the slot mode is calculated as:

$$E_{slot,\rho}(\vec{r}) \approx \frac{j\sin\phi[v_{TE}(H_0^{(2)}+H_2^{(2)})+v_{TM}(H_0^{(2)}-H_2^{(2)})]}{4\cos\phi}k_\rho\frac{\mathrm{sinc}\Big(\frac{k_x\Delta_{gap}}{2}\Big)J_0\Big(\frac{k_y w_s}{2}\Big)}{D_M(k_x)'}\Big|_{k_x=k_x^{slot}}, \tag{C.8}$$

$$E_{slot,\phi}(\vec{r}) \approx \frac{j[v_{TE}(H_0^{(2)}-H_2^{(2)})+v_{TM}(H_0^{(2)}+H_2^{(2)})]}{4}k_\rho\frac{\mathrm{sinc}\Big(\frac{k_x\Delta_{gap}}{2}\Big)J_0\Big(\frac{k_y w_s}{2}\Big)}{D_M(k_x)'}\Big|_{k_x=k_x^{slot}}, \tag{C.9}$$

$$E_{slot,z}(\vec{r}) \approx -\frac{\sin\phi}{2\cos\phi}\frac{k_\rho v_{TM}}{k_{z2}}H_1^{(2)}k_\rho\frac{\mathrm{sinc}\Big(\frac{k_x\Delta_{gap}}{2}\Big)J_0\Big(\frac{k_y w_s}{2}\Big)}{D_M(k_x)'}\Big|_{k_x=k_x^{slot}}. \tag{C.10}$$

After the large-argument approximation on Hankel functions is performed (as in Section 3.1), the residual contribution of the TM_0 mode is:

$$E_{TM_0,\rho}(\vec{r}) \approx -\frac{j}{4}\sin\phi\frac{N_{TM}2H_0^{(2)}}{D'_{TM}}k_\rho M_x(k_\rho,\phi)\Big|_{k_\rho=k_\rho^{TM_0}}, \tag{C.11}$$

$$E_{TM_0,\phi}(\vec{r}) \approx 0, \tag{C.12}$$

$$E_{TM_0,z}(\vec{r}) \approx -\frac{1}{2}\sin\phi\frac{k_\rho N_{TM}}{k_{z2}D'_{TM}}H_1^{(2)}k_\rho M_x(k_\rho,\phi)\Big|_{k_\rho=k_\rho^{TM_0}}, \tag{C.13}$$

and the contribution of the slot mode is equal to:

$$E_{slot,\rho}(\vec{r}) \approx \frac{j\sin\phi}{2\cos\phi}v_{TM}H_0^{(2)}k_\rho\frac{\mathrm{sinc}\Big(\frac{k_x\Delta_{gap}}{2}\Big)J_0\Big(\frac{k_y w_s}{2}\Big)}{D_M(k_x)'}\Big|_{k_x=k_x^{slot}}, \tag{C.14}$$

$$E_{slot,\phi}(\vec{r}) \approx \frac{j}{2}v_{TE}H_0^{(2)}k_\rho\frac{\mathrm{sinc}\Big(\frac{k_x\Delta_{gap}}{2}\Big)J_0\Big(\frac{k_y w_s}{2}\Big)}{D_M(k_x)'}\Big|_{k_x=k_x^{slot}}, \tag{C.15}$$

$$E_{slot,z}(\vec{r}) \approx -\frac{\sin\phi}{2\cos\phi}\frac{k_\rho v_{TM}}{k_{z2}}H_1^{(2)}k_\rho\frac{\mathrm{sinc}\Big(\frac{k_x\Delta_{gap}}{2}\Big)J_0\Big(\frac{k_y w_s}{2}\Big)}{D_M(k_x)'}\Big|_{k_x=k_x^{slot}}. \tag{C.16}$$

[1] $H_n^{(2)}(k_\rho\rho) \equiv H_n^{(2)}$